Interfacial Nanorheology: Probing Molecular Mobility
in Mesoscopic Polymeric Systems

Scott E. Sills

A dissertation
submitted in partial fulfillment of the
requirements for the degree of

Doctor of Philosophy

University of Washington

2004

Program Authorized to Offer Degree:
Department of Chemical Engineering

UMI Number: 3131228

INFORMATION TO USERS

The quality of this reproduction is dependent upon the quality of the copy submitted. Broken or indistinct print, colored or poor quality illustrations and photographs, print bleed-through, substandard margins, and improper alignment can adversely affect reproduction.

In the unlikely event that the author did not send a complete manuscript and there are missing pages, these will be noted. Also, if unauthorized copyright material had to be removed, a note will indicate the deletion.

UMI®

University of Washington
Graduate School

This is to certify that I have examined this copy of a doctoral dissertation by

Scott E. Sills

and have found that it is complete and satisfactory in all respects,
and that any and all revisions required by the final
examining committee have been made.

Chair of Supervisory Committee:
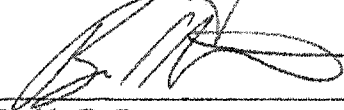
_____

René M. Overney

Reading Committee:

_____

Bruce A. Finlayson

_____

René M. Overney

_____

Buddy D. Ratner

Date: _27 MAY 2004_

In presenting this dissertation in partial fulfillment of the requirements for the doctoral degree at the University of Washington, I agree that the Library shall make its copies freely available for inspection. I further agree that extensive copying of the dissertation is allowable only for scholarly purposes, consistent with "fair use" as prescribed in the U.S. Copyright Law. Requests for copying or reproduction of this dissertation may be referred to Proquest Information and Learning, 300 North Zeeb Road, Ann Arbor, MI 48106-1346, to whom the author has granted "the right to reproduce and sell (a) copies of the manuscript in microform and/or (b) printed copies of the manuscript mode on microform."

Signature _Scott E Sills_

Date _27 MAY 2004_

University of Washington

Abstract

Interfacial Nanorheology: Probing Molecular Mobility in Mesoscopic Polymeric Systems

Scott E. Sills

Chair of the Supervisory Committee:
Associate Professor René M. Overney
Department of Chemical Engineering

Investigating the finite size limited structural relaxations in mesoscopic polymer systems is central to nanotechnological applications involving thin films, complex structures, and nanoscale phase-separated systems; for example, polymer electrolyte membranes, optoelectronic devices, and ultrahigh-density thermomechanical data storage (terabit recording). In such systems, bulk statistical averaging and continuum models are jeopardized. Interfacial constraints lead to bulk-deviating molecular dynamics and dictate material and transport properties. The objective of this dissertation is to provide insight to the exotic mesoscopic behaviors in thin films by developing novel rheological and tribological analytical methods based on scanning probe microscopy (SPM). Activation energies are deduced for the molecular motions associated with internal friction dissipation, and the temperature resolved length scale for cooperative motion during the glass transition is directly obtained for polystyrene. These results confirm the dynamical heterogeneity of the glass transition and reveal a crossover from intra- to inter- molecular relaxation in the transition regime. The impact of dimensional constraints on molecular mobility in ultrathin polymer films is explored through interfacial glass-transition profiles. With these profiles, a structural model of the rheological changes near interfacial boundaries is constructed as function of molecular weight and crosslinking density. The manifestation of interfacial constraints in nanotechnological applications is illustrated for thermomechanical recording, where rheological gradients near the substrate dictate the contact pressure and strain shielding at the substrate compromises film stability. A foundation for the critical aspects of interfacial stability is developed, and mechanically graded interfaces and *modulus-matching* techniques are explored as a means of improving the stability, durability, and stress transmission characteristics of the polymer-substrate interface in thermomechanical recording and the titanium-bone interface in human artificial hip implants.

Table of Contents

List of Figures

List of Tables

Acknowledgements

I would like to express my most sincere gratitude to René Overney for his inspiration, guidance, and keen intuition. I will reflect long on the exhilarating revelations we have shared over the years. Also, my deepest appreciation is extended to Jane Frommer at IBM Almaden for the wholesome guidance and support she has vivaciously bestowed.

Much of this work would not have been possible without the help and support of collaborators at IBM Almaden Research Center: Craig Hawker, Victor Lee, Bob Erickson, Victor Chin, Eugene Delenia, Brooke Van Horn, Wilson Chau, Bob Miller, and Chuck Wade; IBM Zurich Research Laboratories: Bernd Gotsmann, Urs Duerig, Dorothea Weismann, and Michel Despont; and University of Washington Engineered Biomaterials (UWEB): Felix Simonovsky and Buddy Ratner. It has been a pleasure working with each of you. A particular thanks to Bernd for many fruitful discussions and for his guidance and assistance in developing the heated tip force microscopy system.

My past and current fellow group members have been an integral part of this work. Thanks to Cynthia Buenviaje for sharing with me the tricks of the trade; to Martin Bammerlin for his expertise in instrumental development; and to Tomoko Gray and Joseph Wei who always keep me on my toes with data interpretations and creative challenges to conventional force microscopy techniques. I am grateful for all of your friendships.

I would like to express my appreciation to the Benson Hall research support staff for invaluable contributions to instrumental development efforts. In particular, special thanks to Dave Gery in the machine shop and to Arne Biermann in the electronics shop, who both have always been eager make *cool toys* for me to play with in the lab.

This work would never have been completed without the encouragement and devotion of my wife Mandy and my family: my mother Sue, my father Eric, and my brother Roger; Nan, Aunt Sally and Uncle Mike, and Aunt Barb. Finally, I must acknowledge my fellow boating partners who were always sure to keep me safe down in the drop zone; you know who you are.

Dedication

In memory of John Riker.

Introduction

Polymers have become an integral component of our modern lifestyles. Subsistence without Tupperware, Styrofoam cups, compact discs, disposable diapers, pneumatic tires, not to mention 1000's of other applications, is a bleak discernment for many. Over the past decades, polymers have been developed to replace traditional components of metal, glass, wood, paper and leather. The ongoing progression of this substitution process is catalyzed by continued developments in the fundamental understanding of polymer behaviors.

Miniaturization trends of electronic, optical, mechanical, and biomedical devices have brought the nanoscale to the forefront of the engineering design arena. In the 21st century, the nanometer will likely play a role similar to that of the micrometer in the 20th century. In systems reduced to nanoscopic dimensions, interfacial constraints lead to bulk-deviating molecular dynamics and dictate material and transport properties. Interfacial technologies are trapped between the atomistic and the three-dimensional bulk regimes – in the mesoscale. Here, the phenomenological classifications applied macrosystems breakdown. On the other hand, quantum or molecular theories are insufficient in describing the fractal-like behavior of mesoscopic systems.

Rheological material properties that were predominantly determined by macroscopic experiments in the past, e.g. viscosity and modulus, represent underlying microscopic transport properties of momentum and energy. These transport mechanisms are governed by couplings between atoms or molecules, intra- and intermolecular degrees of freedom, and external forces. Simply, macroscopic rheological properties are dictated by molecular mobility. Understanding and controlling molecular mobility becomes increasingly important in technologies that use nanoscopically confined polymeric materials. Herein lies the focus of this work.

The text is organized to first introduce the reader to the technological complexity of nanoscopic polymer applications in Chapter 1, highlighting polymer based thermomechanical data storage as one particular example of the diverse technical challenges faced by many nanotechnologies. In Chapter 2, a foundation of rheological principles is established and the glass transition is considered as a key indicator of molecular mobility. Triborheology is introduced as the particular branch of nanorheology which deals with molecular mobilities at the interface of two contacting materials in Chapter 3. A discussion of polymer triborheology is gradually developed, building on lubrication concepts and thermodynamic models of lubricated

friction. Chapter 4 builds on some of the tribological concepts and techniques considered in Chapter 3, and fundamental insight to the dynamics and kinetics in glass forming polymers is provided. Significant effort is directed towards investigating the finite size limited structural relaxations near the glass transition. In Chapter 5, the progression is made from the fundamental study of mesoscopic molecular motion to the consideration of dimensional constraints. A structural model for rheologically modified interfacial boundary layers is constructed by examining interfacial plasticization, dewetting kinetics, disentanglement barriers, and interfacial glass transition profiles in confined polymer films. At this point, the focus shifts to an engineering perspective. The implications of interfacial constraints on nano-contact mechanical operations is illustrated in Chapter 6 by studying strain shielding and confined plasticity in thin polymer films. Chapter 7 addresses concerns regarding interfacial stability and how to design various polymer interfaces for maximum adhesion and efficient stress distribution. Chapter 8 deals specifically with biological interfaces and applies many concepts developed earlier to the biomechanical and biochemical integration of artificial hip implants with the human skeletal system. Finally, the reader is referred to Chapter 9 for an in depth review of a diverse array of scanning force microscopy and nanoindentation based meso-mechanical analytical techniques.

1. Facing Up to Nanotechnology

1.0 Overview

In the 21st century, the nanometer will play a role similar to that of the micrometer in the 20th century. Miniaturization trends of electronic, optical, mechanical, and biomedical devices have brought the nanoscale to the forefront of the engineering design arena. Prescribed rheological properties and film stability are paramount to the development of polymer thin film and coating technologies; as found, for instance, in ultrahigh density polymer based data storage[1] and organic light emitting diodes.[2]

In systems reduced to nanoscopic dimensions, bulk statistical averaging and continuum models are jeopardized. Interfacial constraints lead to bulk-deviating molecular dynamics and dictate material and transport properties. The challenge for continued evolution of nanotechnologies is to work within the interfacial constraints, or yet, to utilize these constraints as engineering design opportunities.

This chapter is devoted to illustrating the technological complexity of nanoscopic polymer applications. For this intent, polymer based thermomechanical data storage is highlighted as one particular example of the diverse technical challenges faced by many nanotechnologies. The reader is urged to reflect on the demanding services required of the confined polymeric storage media while exploring the fundamental and applied attributes of mesoscopic polymeric systems in the forthcoming chapters.

1.1 Terabit Data Storage in Thin Polymer Films

It is predicted that within a few years, magnetic storage technology will reach the well-known superparamagnetic limit ($\sim$100Gb/in^2). The approach of this fundamental limit has motivated investigations of completely new data storage techniques, for example, localized mechanical probes or holographic methods.[1]

Any new technology being considered as a replacement for an existing technology must offer long-term viability since considerable commercial investment will be required for *very large-scale integration* (VLSI). A currently available tool that is simple, yet demonstrates long-term potential, is a nanometer-sharp probe.[1] Such probes are currently used in scanning force and scanning tunneling microscopes (SFM and STM) for sub-micron to sub-nanometer investigations.

4

The potential for using an SFM probe in data storage was first demonstrated by Mamin and Rugar in the early 1990's.[3] Their pioneering work utilized a single SFM probe in contact with a rotating polycarbonate substrate. The data bits were written by thermomechanically creating indentations in a polycarbonate surface by simultaneously heating and loading the probe. The read back mechanism used the same probe to detect the topographic features.

Recently, researchers at the IBM Zurich Research Laboratory have demonstrated ultra high storage densities of 0.5-1.0 Tb/in^2 with single probe thermomechanical storage, and have developed a highly parallel two dimensional array of probes (32x32), called *Millipede*, to address the issue of limited single probe data rates.[1] This high areal storage density makes thermomechanical data storage systems very attractive as a potential future technology in mobile applications, offering several gigabyte capacity and low power consumption at megabyte/second rates, for devices such as personal digital assistants, cellular phones, and multifunctional watches. Despite the preliminary success of the initial Millipede prototype, a number of fundamental issues remain to be investigated, for example, the design and optimization of the mechanical and transport properties of the polymeric storage media.

The concept of thermomechanical data-storage relies on the writing, reading, and erasing of nanometer sized data-bit *indentations* within a suitable polymer storage medium. A local probe, similar to an SFM cantilever tip, is employed for the necessary storage operations. Bit indentations are written by a combination of locally softening the polymer, above T_g, by heating the probe tip while simultaneously applying a force to the probe, pressing it into the polymer film, Figure 1-1. Each indentation represents one data bit. Recorded bits are read-back by measuring a change in heat flux (resistance across the heater tip) from the probe to the polymer. Erasing bits requires local heating with the probe to a temperature above T_g, where the displaced polymer may backflow into the original indentation.
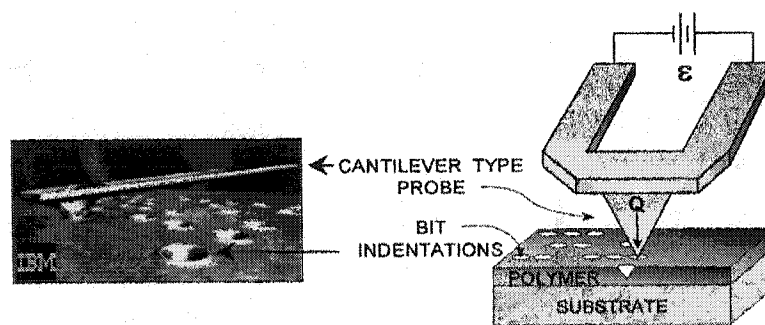
Figure 1-1: Thermomechanical data storage; a probe is heated and pressed into the polymer media forming a ~30nm indentation that represents 1 bit. Bits are recorded on a nanometer pitch in a ~50nm thick polymer film. Left image courtesy of IBM.

In a single probe thermomechanical storage device, storage densities up to 1 Tb/in^2 have been achieved.[1] Currently, the mechanical resonant frequency of the SFM probe limits the data rate of a single probe device to a few Mb/s,[3] which must be improved three orders of magnitude to compete with magnetic storage technology. To address the issue of limited single probe data rates, researchers at the IBM Zurich Research Laboratory have developed a highly parallel two dimensional array of probes,[1] Figure 1-2. The (32x32) cantilever array is operated in a parallel / multiplexed manner, where each cantilever / tip reads and writes data only in its own storage field. The storage capacity of the system scales with the areal density (indentation pitch), individual storage field size (cantilever pitch), and the number of cantilevers in the array. Despite the preliminary success of the initial Millipede prototype, a number of fundamental issues must be addressed before Millipede can be considered for commercial applications, namely the design and optimization of a suitable polymer storage media.
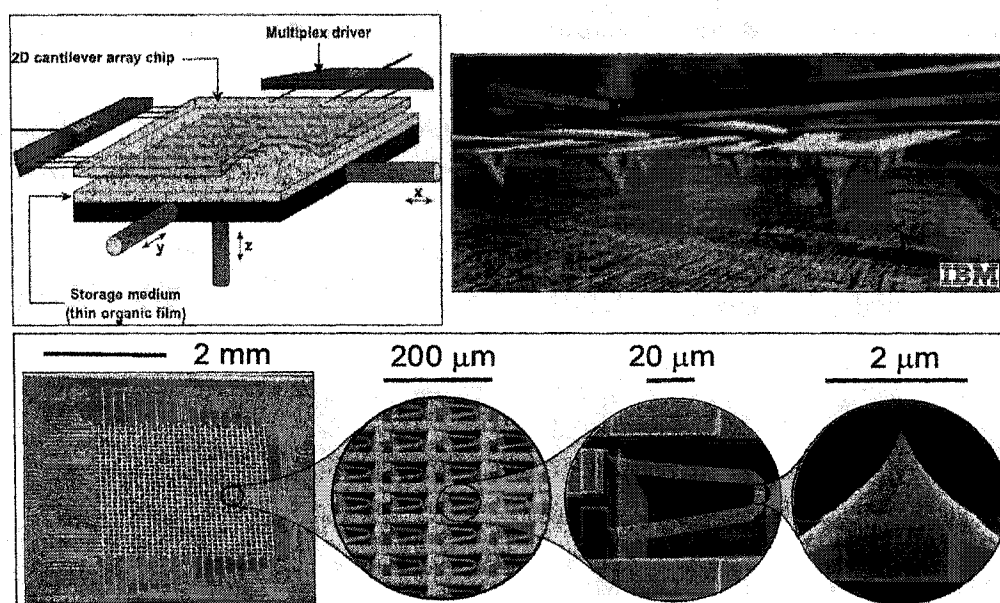
Figure 1-2: The 2D cantilever array for thermo-mechanical data storage. (A) Schematic of parallel / multiplexed operation of cantilever array. (B) visual representation of cantilever array and polymer storage media. (C) SEM images of prototype (32x32) cantilever array. Images courtesy of IBM.

The mechanical and material properties of the polymer storage media are critical to thermomechanical storage operations. The ideal polymer medium should be easily deformable for bit writing; however, the written bits must be stable against wear, thermal degradation, and

dewetting, offering a minimum reliability of ten years. In addition, the polymer must allow reversible bit indentations, i.e. controlled backflow, for erasing and re-writing.

By nature, polymers are well suited for thermomechanical recording because their properties are generally well controllable through temperature and process rates (frequency). The polymer's glass transition temperature, T_g, is one of the main parameters determining the threshold writing temperature. An ideal polymer exhibits a well defined glass transition at a sufficiently high temperature (>100°C) to prevent deformation of the bit indentations during thermal read-back of the data. However, an excessively high T_g would require a higher operating temperature, increasing the power consumption of the device.

The writing and erasing processes rely on local deformation of the polymer film, and to exploit the enhanced molecular-chain segment mobility above the glass transition point, these processes are conducted at a local temperature above T_g. Elastic recovery of displaced material is prevented by rapidly quenching the indentation site to below T_g, with the probe tip in place. As a result, the deformation is *frozen in* because the motion of molecular-chain segments is effectively inhibited below T_g. In order to preserve the recorded data, any further deformation of the polymer film must be limited during read-back and scanning; therefore, these operations are conducted below T_g, where molecular-chain segmental mobility is effectively inhibited.

In addition to achieving the appropriate T_g, the polymer film should exhibit a large drop, by orders of magnitude, in the shear modulus, G, at T_g. When the probe tip is indented into the polymer during writing and erasing (above T_g), the polymer is strained, and elastic shear stresses are incorporated into the film in the vicinity of the indentation. Unlike the deformation of a simple liquid, the indentation represents a metastable state of the deformed volume. The driving force for recovery of the initial unstressed state is directly related to the magnitude of the incorporated elastic stresses. In the interest of bit stability, elastic recovery should be avoided; hence a low shear modulus, leading to reduced internal stresses during the indentation process (above T_g), is desirable. To further promote longevity of recorded bit indentations, the strain applied to the polymer film during the reading/scanning operation, below T_g, must be minimized, and a higher shear modulus is desired. The higher modulus, assuming a constant adhesion force, will result in reduced friction forces, thus a reduced potential for wear.

The thermomechanical storage technique also requires specific attention to the local thermal transport properties of the polymer media and underlying substrate. Ideally, the heat transfer to the polymer should be limited only to the indentation site so adjacent data bits are not subject to thermal degradation, and the excess heat should be removed through the supporting substrate, a

heat sink. This requires that the polymer medium has a very low thermal conductivity relative to the substrate. The heat transfer from the probe tip to the polymer is highly nonlinear, making it very difficult to reproducibly control tip penetration into the polymer, and hence, to maintain small uniform bit indentations.[1] In order to overcome this difficulty, the depth of the tip penetration must be limited. The use of ultra-thin polymer films (<100nm) on a hard impenetrable substrate is a necessary and sufficient means to limit tip penetration. With this configuration, the hard substrate prevents the tip from penetrating farther than the film thickness.

A current and substantial impediment to designing the polymer storage medium in its confined substrate configuration is the lack of fundamental knowledge about thermal transitions on the sub-100nm scale. The scaling behavior of thermoplastic and thermosetting polymers is simply not well-established, neither in fundamental understanding nor in performance. Commercially available polymers have served for the purpose of demonstrating device feasibility. Ultimately, however, achieving the goals for a successful storage device will require engineered polymeric media *of tailored molecular structure*. The reason for tailoring the molecular structure is to achieve the narrow range of physiochemical properties that ensure high durability, long shelf life, and low power consumption.

The basis of our continued work focuses on developing the necessary molecular structure tailoring and characterizing, on the nanometer scale, the rheological and performance responses of the tailored polymer films. Three types of polymer interfaces are relevant to this application: *polymer-substrate* between the foundation film and the underlying silicon substrate, *polymer-polymer* between the foundation film and the storage medium film, and *polymer-point* between the thermomechanical probe the storage medium surface. The relevant issues and research results pertaining to the above interfaces will be discussed in the appropriate forthcoming chapters.

8

1.2 Notes to Chapter 1

[1] P. Vettiger, G. Cross, M. Despont, U. Drechsler, U. Duerig, W. Heberle, M. I. Lantz, H. E. Rothuizen, R. Stutz and G. K. Binnig, *IEEE Transactions on Nanotechnology* **1,** 39 (2002).

[2] T. Gray, C. Buenviaje, R. M. Overney, S. A. Jenekhe, L. Zheng and A. K. Y. Jen, *App. Phys. Lett.* **83,** 2563 (2003).

[3] H. J. Mamin and D. Rugar, *Appl. Phys. Lett.* **61,** 1003 (1992).

2. Nanorheology

2.0 Overview

In a classical sense, rheology is defined as the study of the flow and deformation of matter and is generally deduced from material properties of fluid and semi-solid materials. Rheology spans many disciplines and is used to describe the properties of a wide variety of materials such as oils, foods, inks, polymers, clays, concrete, asphalt, amongst others. The commonality between these diverse systems is that each material exhibits some sort of flow characteristics and, therefore, cannot be treated as perfect solids. Any material that displays both *liquid-like* and *solid-like* characteristics is referred to as viscoelastic.

Rheological material properties that were predominantly determined by macroscopic experiments in the past, i.e. viscosity and modulus, represent underlying microscopic transport properties of momentum and energy. These transport mechanisms are governed by couplings between atoms or molecules, intra- and intermolecular degrees of freedom, and external forces. Simply, macroscopic rheological properties are dictated by molecular mobility. In this sense, *nanorheology* focuses on the nanoscopic contributions of molecular mobility to the phenomenological rheological properties of matter.

Understanding and controlling molecular mobility becomes increasingly important in technologies that use nanoscopically confined materials. In these systems, bulk statistical averaging and continuum models are jeopardized. Interfacial, i.e. dimensional, constraints lead to bulk-deviating molecular dynamics and dictate material and transport properties.

In this chapter, a general foundation for rheology is provided in section 2.1 with a discussion of viscoelasticity. In section 2.2, the glass transition is introduced as an indicator of molecular mobility, and various theoretical interpretations of the glass transition are reviewed. Finally, the role of dimensional constraints in nanoscopic systems is discussed in section 2.3.

2.1 Viscoelasticity: Between Liquids and Solids

Viscoelastic materials, notably polymers, exhibit a time and temperature dependence in their stress-strain-strain rate relationships. Their behavior may be liquid-like and or solid-like. In a perfect viscous fluid, the stress-strain-strain rate relationship is characterized by Newton's law,

with the stress, τ, directly proportional to the strain rate, $\dot{\gamma}$, but independent of the magnitude of the strain, γ, i.e.

$$\tau = \eta\dot{\gamma} \tag{2.1-2}$$

where η is the absolute viscosity of the fluid. This viscous phenomenon is generally modeled as a *dashpot*. For an ideally elastic material, the stress-strain relation is described by Hooke's law, where the stress is directly proportional to the strain, but independent of the strain rate, i.e.

$$\tau = G\gamma \tag{2.1-1}$$

The proportionality constant, G, represents the appropriate modulus, either the shear or Young's modulus, depending on the orientation of the applied stress. Elastic deformation is generally modeled as a *simple spring*, and viscoelastic materials displaying both solid-like and liquid like behaviors may be modeled as various *spring* and *dashpot* combinations. The two simplest models are the Maxwell and Kelvin-Voight models with a spring and dashpot in series and parallel, respectively, Figure 2.1-1. The Maxwell model is the simplest model which exhibits a material's viscous behavior, i.e. steady creep, and the Kelvin-Voigt model is the simplest one to characterize delayed elasticity on both loading and unloading.
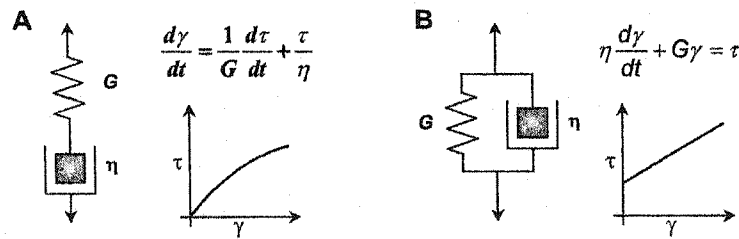
Figure 2.1-1: Viscoelastic models: (A) Maxwell model, and (B) Kelvin-Voigt model.

The stress-strain relations for a linear viscoelastic material are most commonly expressed through the *creep compliance function*, $\Phi(t)$, which describes the strain response to a step change in stress, or the *relaxation function*, $\Psi(t)$, which describes the stress response to a step change in

strain. For an incompressible material, the stress-strain relations in terms of the deviatoric stress (σ^{δ}) and strain (ε^{δ}) components, respectively, are:[1]

$$\sigma^{\delta} = \left(\sigma - \sigma^{*}\right) \qquad \varepsilon^{\delta} = (\varepsilon - \varepsilon^{*}) \tag{2.1-3}$$

where * denotes the hydrostatic or spherical component of the stress or strain tensor, i.e. $\sigma^{*} = \frac{1}{3}(\sigma_1 + \sigma_2 + \sigma_3)$ and $\varepsilon^{*} = \frac{1}{3}(\varepsilon_1 + \varepsilon_2 + \varepsilon_3)$ with subscripts $1, 2, 3$ denoting the principle stresses and strains. For an incompressible material, $e^{*} = 0$, so that:

$$\sigma^{\delta} = 2G\varepsilon^{\delta} = 2G\varepsilon \tag{2.1-4}$$

The corresponding relation for an incompressible viscoelastic material becomes:[1]

$$\sigma^{\delta}(t) = \int_0^t \Psi(t - t') \frac{\partial \varepsilon^{\delta}(t')}{\partial t'} dt' \tag{2.1-5}$$

$$\varepsilon^{\delta}(t) = \int_0^t \Phi(t - t') \frac{\partial \sigma^{\delta}(t')}{\partial t'} dt' \tag{2.1-6}$$

The appropriate forms of the creep compliance and relaxation functions are determined from appropriate spring and dashpot models or obtained experimentally. For a Maxwell material, i.e. steady creep:

$$\Phi(t) = \left[\frac{1}{G} + \frac{1}{\eta} t\right] \qquad \Psi(t) = G e^{-\frac{t}{\tau}} \tag{2.1-7}$$

and for a Kelvin-Voigt model:

$$\Phi(t) = G \qquad \Psi(t) = \frac{1}{G}\left(1 - e^{-\frac{t}{\tau}}\right) \tag{2.1-8}$$

where τ represents the relaxation time characterized by $\tau = \eta/G$.

Rheometric measurements normally consists of a *strain (deformation)* or a *stress* analysis at a specified frequency or range of frequencies. Generally, the strain response to an applied stress (relaxation experiment), or the stress response to an applied strain (creep experiment) are out of phase by the amount δ. This out of phase phenomenon is usually described by a complex modulus function $G^* = G' + iG''$. G' is referred to as the *storage modulus* and is related to the energy *stored* in the elastic component. G'' is referred to as the *loss modulus* and is related to the energy dissipated, or *lost*, through the viscous behavior. A vector diagram of the complex modulus is depicted in Figure 2.1-2
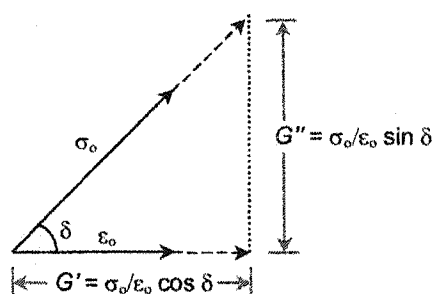
Figure 2.1-2: Vector diagram of the complex modulus

A large value of G' in comparison of G'' indicates pronounced elastic properties. For such a product the phase angle is also small (a phase angle of $0°$ means a perfectly elastic material and a phase angle of $90°$ means a perfectly viscous material). On the other hand, a small value of G' in comparison of G'' indicates pronounced viscous properties.

2.2 Glass Transitions: Unlocking Molecular Mobility

To describe material behavior in terms of transport properties it is essential to know, in addition to the structural properties, the kinetic properties such as the molecular mobility. Particularly in amorphous condensed systems, such as polymers, the determination of the molecular mobility is of foremost importance. A parameter that has been found paramount in predicting the degree of molecular mobility is *the glass transition temperature, T_g.*

The *glass transition* is defined as the reversible change in an amorphous material (e.g., polystyrene) or in amorphous regions of a partially crystalline material (e.g., polyethylene), between a viscous or rubbery condition and a hard, relatively brittle one.[2] The temperature at

which the transition occurs, or possibly the *starting-point* of the temperature regime over which the transition occurs (see Chapter 3), is defined as the glass transition temperature. The term *glass transition* is used in the materials community pervasively, implying that it describes a well-understood material phenomena or material property. However, similar to other poorly defined terms, such as *friction*, a large ambiguity exists. The problem in describing the glass transition or in reporting the transition temperature unambiguously arises from: *diverging* instrumental methods; critical parameters such as, measurement rates or areas; and processes responsible for changing molecular mobilities (see chapter 4); all of which can lead to diverging theoretical models and interpretations.

The definition of the glass transition presented above depends on the perception of *solid* and *liquid*. Materials may be classified as "solids" and "liquids" by either considering their rheological response, or by analyzing the thermodynamic phase of the system. A rheological material description is concerned about stress-strain and stress-strain-rate relationships. As discussed above, a *solid-like* behavior exhibits a rheological behavior characterized by a purely stress-strain relationship. Conversely, a *liquid-like* behavior is a purely strain-rate dependent process and cannot be described with a stress-strain relationship. Any real material will exhibit various degrees of both behaviors, depending on (a) its microscopic (molecular) and macroscopic intrinsic mobility, and (b) the extrinsic stress and stress rate to which it is exposed.

From the thermodynamic perspective of free energy changes between equilibrium states, one may identify the solid-liquid phase transition by a discontinuity in the first partial derivatives of the Gibbs free energy, G, with respect to the relevant state variable (e.g., temperature, T, and pressure, P), as illustrated for the volume-temperature plot in Figure 2.2-1.
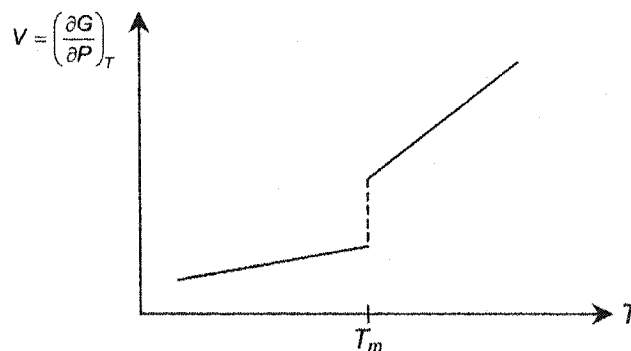
Figure 2.2-1: Volume discontinuity. First-order transition between liquid and solid. (T_m = melting temperature).

Discontinuities, as expressed in the first partial derivatives of the Gibbs free energy are found in the temperature relationships of the volume, V; entropy, S; and enthalpy, H.

$$\left(\frac{\partial G}{\partial P}\right)_T = V \qquad \left(\frac{\partial G}{\partial T}\right)_P = -S \qquad \left(\frac{\partial(G/T)}{\partial(1/T)}\right)_P = H \qquad (2.2\text{-}1)$$

Mesophases between solid and liquid phases that are found in polymeric systems include the states of a *glass* and a *melt*. The glass state is known to exist also for many non-polymeric materials. From a structural viewpoint a solid can be either crystalline, amorphous (unstructured) or partially amorphous-crystalline. A *glass* is an amorphous solid and can exhibit both solid- or liquid-like behaviors. The *melt* behaves rheologically liquid-like; yet, exhibits short-range order similar to the amorphous solid not present in perfect liquids. The melt state compared the corresponding glass-state shows the same structure, but exhibits *large amplitude* molecular motions, such as translational, rotational, and conformational motions. The large amplitude motions operate on the picosecond (10^{-12}s) time-scale. Around the glass transition temperature, the time-scale of this large amplitude motion is slowed to milliseconds or even seconds. [3]

Empirically it has been found that for many glasses with mobile units the size of one to six atoms, called *beads*, the heat capacity increases "abruptly" by about $11\ ^J/_{mol\ K}$ at the glass transition temperature.[3] Discontinuity in the heat capacity is known to exist and can be caused by second-order transitions. Second order transitions are considered as *order-disorder transitions*, and express a continuous behavior of the free energy and its partial derivatives, and a discontinuous behavior for the second partial derivative with respect to the relevant state variable. Hence there are no discontinuities in S, V or H at the glass transition temperature, but the discontinuities lie in the heat capacity, C_p, the isothermal compressibility, k, and the coefficient of thermal expansion, α:

$$C_p: \qquad -\left(\frac{\partial^2 G}{\partial T^2}\right)_P = \left(\frac{\partial S}{\partial T}\right) = \frac{C_p}{T} \qquad \frac{\partial}{\partial T}\left[\left(\frac{\partial(G/T)}{\partial(1/T)}\right)_P\right]_P = \left(\frac{\partial H}{\partial T}\right)_P = C_p \qquad (2.2\text{-}2)$$

$$\kappa: \qquad \left(\frac{\partial^2 G}{\partial P^2}\right)_T = \left(\frac{\partial V}{\partial P}\right)_T = -\kappa V \qquad (2.2\text{-}3)$$

$$\alpha: \qquad \left[\frac{\partial}{\partial T}\left(\frac{\partial G}{\partial P}\right)_T\right]_P = \left(\frac{\partial V}{\partial T}\right)_P = \alpha V \qquad (2.2\text{-}4)$$

First and second order transitions are illustrated in Figure 2.2-2. If compared to property changes in glasses around the glass transition temperature, one finds some similarity between the glass transition and the second order transition. There are however significant differences. C_p, κ and α values are always smaller and nearly constant below T_g compared to the values above T_g. This is in contrast to the second-order transition. A more disturbing finding is that T_g measurements are highly heating/cooling rate dependent, which does not occur for a "true" second-order transition.[4]
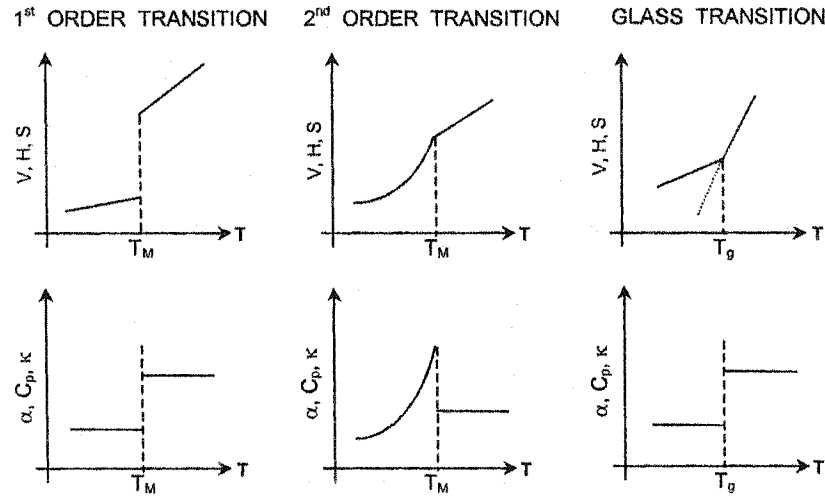
Figure 2.2-2: The nature of material property changes at T_g compared to those of 1st and 2nd order transitions.

Based on the similarity of the glass transition with a second order thermodynamic transition, the Ehrenfest approach may applied.[4] Equilibrium criteria requires $G_{glass} = G_{melt}$, and the analogous form of the Clausius–Clapeyron equation is:

$$\frac{dP}{dT_g} = \frac{\Delta H}{T\Delta V} \qquad (2.2\text{-}5)$$

For a second order phase transition, this gives:

$$\frac{dT_g}{dP} = \frac{\Delta\kappa}{\Delta\alpha} = \frac{T\Delta\alpha}{\Delta C_p} \qquad \text{or} \qquad T_g = \left.\frac{\Delta\kappa\Delta C_p}{\Delta\alpha^2}\right|_{T=T_g} \qquad (2.2\text{-}6)$$

However for most polymers, the following has been observed:[5]

$$\frac{dT_g}{dP} < \frac{\Delta\kappa}{\Delta\alpha} \qquad \text{and} \qquad \frac{dT_g}{dP} \approx \frac{T\Delta\alpha}{\Delta C_p} \qquad (2.2\text{-}7)$$

suggesting that the glass transition is not a true second order thermodynamic transition.

Recognizing the thermal and loading rate dependencies of the glass transition process, the glassy state can be described as a non-equilibrium state. This approach requires, in addition to the state variables, an internal order parameter. In other words, from the concept of an order-disorder transition, where the glass is the ordered state, the internal order parameter describes the departure from equilibrium conditions. Fox and Flory suggest that the appropriate order parameter is the *free volume*.[4] The free volume, V_f, is defined as the *void* space within the polymer phase that is not occupied by the molecules themselves, and may be quantified by the difference between the total volume, V, and the molecular volume, V_m. The molar volume is the sum of the hypothetical volume in a void free melt at absolute zero and the volume expanded due to thermal vibrations. The relation for the free volume is then:

$$V_f = V + V_m \left[\Delta\alpha\left(T - T_g\right) - 1\right] \qquad (2.2\text{-}8)$$

Just below T_g, the molecular mobility is so drastically reduced that a non-equilibrium state would become effectively frozen, suggesting a constant free volume below T_g. From Figure 2.2-2, it is seen that $\Delta\alpha=0$, and with V and V_m exhibiting the same temperature dependence, V_f becomes constant, see Figure 2.2-3.

Between the solid glass state and the melt state, i.e., for temperatures between T_g and the melting temperature, T_m, the material can be treated as a supercooled fluid.
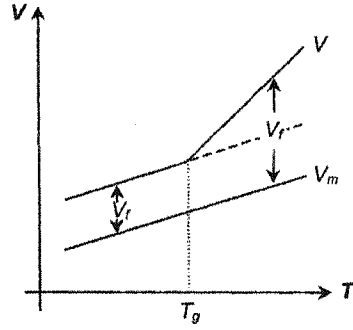
Figure 2.2-3: Free volume diagram as a function of temperature.

Using Eyring's thermodynamic model for supercooled liquids, the viscosity may be expressed in the form of:

$$\eta = \eta_0 \exp\left(\frac{\Delta G_a}{k_b T}\right); \quad \eta_0 = \frac{k_b T}{C_E v_a} \tag{2.2-9}$$

with ΔG_a as the height of free energy barrier to be crossed by Eyring's jump, the Boltzmann constant k_b, the activation volume of the stress, σ, deformation v_a (assume $v_a \sigma \ll kT$), and a constant C_E. With decreasing temperature, i.e. $T \rightarrow T_g$, the Arrhenius behavior breaks down, and the viscosity is represented by a power law, or by the empirical Williams-Lendel-Ferry (WLF) relationship:[4]

$$\log\left(\frac{\eta}{\eta_g}\right) = \frac{-c_1(T - T_g)}{c_2 + T - T_g} \tag{2.2-10}$$

where $T \sim \geq T_g$; and the constants c_1 and c_2 are defined as:

$$c_1 = B/(2.303\, f_g) \tag{2.2-11}$$

$$c_2 = f_g / \alpha_f \tag{2.2-12}$$

where B is a constant taken as unity according to Doolittle,[4] f_g is the fractional free volume, V_f/V, in the glass transition region, and α_f is the coefficient of thermal expansion of the free volume. The apparent activation energy, E_a, associated with this kinetic model becomes:

$$E_a = -2.303\,(c_1/c_2)\,RT^2 \tag{2.2-13}$$

with $T \gtrsim T_g$ and R as the gas constant.

Comparing the above theories one finds that the *free volume model* presumes that the entire motion of atoms results only from the distribution of free volume without crossing the energy barrier. Contrarily in the *kinetic model*, one assumes that the atomic motions are the consequence of a co-operative rearrangement of an assembly of structural units under the effect of thermal fluctuations, which allow the jump over the energy barrier separating the initial configuration from the final configuration. It has been very difficult to experimentally establish a preference for either of the two theories.

There are a diverse array of instrumental techniques employed for determining glass transition temperatures. The most classical methods for obtaining T_g are calorimetric measurements (differential scanning calorimetry, DSC) that record the specific heat capacity as a function of the temperature, $C_p(T)$. Other methods involve dilatometric measurements for the determination of the specific volume, mechanical property measurements (thermomechanical analysis, TMA, and dynamic mechanical analysis, DMA), and dielectric measurements. We have found that the relatively new shear modulated scanning force microscopy technique, SM-SFM, is especially well suited for near surface T_g measurements in confined interfacial systems. The details of this technique are discussed in Chapter 9.

2.3 The Role of Dimensional Constraints

Since mathematicians have introduced us to many dimensions, it has been our desire to strive for more degrees of freedom while seemingly unsatisfied with the four dimensions we live in.[6] Our pursuit of entertaining ourselves with fictions that escape our common senses is documented as early as 1884 in the satire "Flatland - A Romance of Many Dimensions" by Edwin A. Abbott.[7] While Abbott's work tries to introduce the reader to the concept of the multi-dimensional space, it chooses fewer dimensions than three as starting point. By doing so, Abbott came up with imaginary laws of nature that apply in one and two dimensions. Although these

laws, which for instance explain how rain is experienced in two dimensions, are unrealistic, they impressively illustrate the mystery of lower dimensionalities.

Indeed, the laws of nature, or more appropriately, the perception of them in the form of material and transport properties, are challenged if a three dimensional bulk material is reduced to a two dimensional plane. This becomes apparent in many interfacial applications, such as thin film technologies. Structural, material, and transport properties are increasingly dominated by interfacial, interactive, and dimensional constraints. Statistical properties are altered in small ensemble systems, and interfacial properties become dominant on the so-called *mesoscale*.

Material properties, either physical or chemical in nature, are distinctive attributes of a steady-state condensed system. It is imposed that such *intrinsic* properties are time independent, i.e., they describe thermodynamically equilibrated material characteristics. An experimentally determined value is referred to as an *apparent property value* if it depends on system parameters, for instance, the rate at which the experiment is performed. An example of a rate dependent property is viscosity. By definition, the intrinsic value of a rate dependent property is the extrapolated value in regards of an infinite time period over which the property is obtained. There are properties that are combinations of truly independent properties, e.g., the material density as the mass per unit volume. The properties of foremost interest are *intensive* properties, i.e., properties that are independent of the size of a system. Transport properties such as wave propagation, diffusion, and conduction are known to depend strongly on material properties, but also on geometrical constraints and dimensional confinement. It is very challenging, especially in mesoscopic systems like ultrathin polymer films, to determine the origin for exotic, bulk-deviating transport properties.

Critical Length Scales: Dimensional and topological constraints

Critical length scales, kinematics, and dissipation are primarily problems of distributions, probabilities, and cutoff limits. Moving from two dimensional systems or nanoscale small ensembles to three dimensional systems, we find ourselves in a fractional dimensionality. Material transport and reaction properties are known to be strongly affected by the so-called fractal dimension. For instance, for decades it is common knowledge that bulk kinetics and the kinetics at surfaces are significantly different processes. While bulk kinetics are described by time-independent rate constants, kinetics at surfaces reveal time dependent rate coefficients, also termed apparent coefficients[8]. Chemical and non-chemical, e.g., exciton-exciton recombination, reactions that take place at interfaces of different phases, are called *heterogeneous* processes.

Already in the late 1950s, the diffusion and the kinetics, for instance of the adsorption of alcohols at water-air interfaces, has been discussed in terms of barrier-limited adsorption[9] and diffusion-limited[10] processes with time-dependent rate coefficients. The difference between a three-dimensional vs. a two-dimensional process is the number of available degrees of freedom. Restricted degrees of freedom limit the diffusive fluxes and hence, any apparent kinetics in the absence of convective processes like mixing. For surface reactions, this entropic cooling effect can be pictured as a constraint in the natural self-diffusion process. In the forth coming chapters, bulk-deviating properties of interfacial polymeric systems and the technological ramifications will be discussed in context of the relevant length scales.

Critical time scales: Apparent properties

Material properties that were predominantly determined by macroscopic experiments in the past represent underlying microscopic transport properties of momentum and energy. Microscopic transport mechanisms are governed by couplings between atoms or molecules, intra- and intermolecular degrees of freedom, and external forces. The degrees of freedom are influenced by chemical groups and the *stiffness* of molecular interactions. Associated with the couplings is a spectrum of intrinsic characteristic times, τ_i, and extrinsic characteristic times, τ_e, also called the experimental "drive" time. Intrinsic characteristic times relate to structural relaxation and energy distribution and dissipation times within the material; while extrinsic characteristic times relate to observation times that are connected with the rate of the applied external forces. The relationship between these two time-scales, τ_i / τ_e, is called the Deborah number, D_e,[11] and is critical for many processes. In the forthcoming chapters, we will explore how the dimensional constraints imposed on interfacial systems affect these characteristic times and the resulting material properties.

2.4 Notes to Chapter 2

1.   K. L. Johnson, *Contact Mechanics* (Cambridge University Press, Cambridge, 1985).

2.   A. S. f. T. Materials, (American Society for Testing Materials, ASTM E 1142).

3.   J. R. Fried, *Polymer Science and Technology* (Scott, Foresman, and Co., Glenview, IL, 1995).

4.   U. Eisele, *Introduction to Polymer Physics* (Springer-Verlag, Berlin, 1990).

5.   R. G. C. Arridge, *Mechanics of Polymers* (Clarendon Press, Oxford, 1975).

6.   R. M. Overney and S. E. Sills, in *Interfacial Properties on the Submicrometer Scale*, 781, ed. J. Frommer and R. M. Overney (Oxford University Press, Washington, DC, 2001), p. 2.

7.   E. A. Abbott, *Flatland - A Romance of Many Dimensions* (Dover Publ., New York, 1992).

8.   R. Kopelman, *Science* **241**, 1620 (1988).

9.   R. S. Hansen and T. C. Wallace, *J. Phys. Chem.* **63**, 1085 (1959).

10.   R. Defay and J. R. Hommelen, *J. Colloid. Sci.* **14**, 411 (1959).

11.   M. Reiner, *Phys. Today* January, 62 (1964).

3. Triborheology

3.0 Overview

Tribology implies the study of rubbing, and is concerned with the phenomena occurring at the interface between two or more bodies in relative motion. The nature and manifestations of the interactions that take place at the interface determine the friction and wear behaviors of the materials involved. During these interactions, forces are transmitted, energy is dissipated, and the surface topography may be deformed. All of these processes are intricately related to the molecular mobility of the materials in contact, and to the ability of the molecules to flow (lubrication) and deform (wear) under the induced contact stresses. In this light, nanoscale tribology constitutes the particular branch of nanorheology (see section 2.0), i.e. triborheology, which deals with molecular mobilities at the interface of two contacting materials.

Polymers serve also as important tribological materials because of their self-lubricating qualities and excellent wear resistance. The tribological behavior of polymers is significantly different depending on the molecular structure, crystallinity, molecular weight, and crosslinking density,[1] all of which are tied to molecular mobility. Moreover, nanotribological studies of polymers offer particular insight to the molecular relaxation behavior responsible for frictional dissipation and to the intrinsic nanorheological properties, such as activation energies for molecular motion, molecular relaxation times, and the length scale over which cooperative motion occurs (see Chapter 4).

In this chapter, a discussion of polymer triborheology is gradually developed, building on lubrication concepts and thermodynamic models of lubricated friction. The utility of lateral force microscopy (LFM) as a nanorheological tool is demonstrated for polymer friction studies in section 3.5.

3.1 Classical Lubrication Concepts

Since technology is driving lubricant films to molecular thicknesses, kinetic friction and its dependence on the sliding parameters, especially the sliding velocity, have become of great interest. The complexity of the frictional resistance in lubricated sliding is illustrated in Figure 3.1-1 with a *Stribeck Curve*. Various regimes of lubrication are identified within the Stribeck curve to express to what degree the hydrodynamic pressure is involved in the lubrication

process. In the ultra-low speed regime, called the *boundary lubrication regime,* no hydrodynamic pressure is sustained in the lubricant. Consequently, the load is carried by contact asperities that are coated with adsorbed lubricant molecules. If the speed is raised, a hydrodynamic pressure builds up that leads to a *mixed lubrication* in which the load is carried by both, asperities and hydrodynamic pressure. At even higher speeds, elastic contributions of the solid surfaces have to be considered paired with hydrodynamic pressure effects (elastohydrodynamic lubrication), until only *hydrodynamic lubrication* is relevant.

As illustrated, the Stribeck curve encompasses various aspects of lubrication. The curve cannot be discussed without considering the lubricant film thickness, and the different models of asperity contact sliding. In one of the first comprehensive physical models of "dry" friction, Bowden and Tabor introduced a plastic asperity model, in which the material's yield stress and adhesive properties play an important role.[2] Considering this model, which depends on surface energies and mechanical yield properties, paired with all the properties that accompany an adsorbed lubricant, one can hardly grasp the difficulty level involved in describing the frictional kinetics in lubrication.
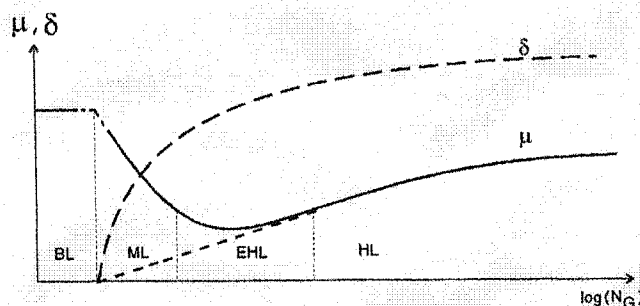
Figure 3.1-1. Stribeck Curve (schematic) relates the fluid lubricant thickness, δ, and the friction coefficient μ to the Gumbel Number $N_G = \eta\, \omega P^{-1}$; i.e., the product of the liquid bulk viscosity, η, the sliding speed (or more precisely the shaft frequency), ω, and the inverse of the normal pressure, P. BL: Boundary Lubrication, ML: Mixed Lubrication, EHL: Elastohydrodynamic Lubrication, HL: Hydrodynamic Lubrication.

Past and current engineering challenges in lubrication have been met with great and complex empiricism. The design of lubrication junctions generally involved only bulk property considerations paired with poorly understood adsorption mechanisms. The complexity of today's lubricants, most of them a product of years of empirical design, i.e. motor oil, has increased

exponentially, making it very difficult to meet future challenges. The problem of empiricism is that conventional laws and perceptions are unchallenged. *Effective* quantities are invented (e.g., effective viscosity), and exponential fitting parameters are introduced (e.g., Kohlrausch relaxation parameter). Progress based on empiricism is generally incremental, and rarely revolutionary.

One of the reasons for empiricism is a lack of access to a system with fewer dimensions and better controlled parameters. In lubricated sliding, that challenge has been addressed over the last two decades with the inception of the surface forces apparatus (SFA) by Tabor et al.[3] and scanning force microscopy (SFM) by Binnig et al.[4] These two instrumental methods allow lubrication studies where roughness effects can be neglected, surface energies controlled, and wear from wearless friction distinguished. Lubricant properties can be studied at nearly mathematically described boundaries, atomistic friction events can be recorded, and fundamental models that have been considered to be mere Gedanken Experiments, such as the *Tomlinson model of friction*, can be verified. In the wake of these nanoscopic tools, exciting new theoretical lubrication and friction models have appeared.

3.2 From Bulk to Molecular Lubrication

In the classical theories of tribology by da Vinci, Amonton and Coulomb, not much attention was given to the dependence of kinetic friction on the sliding velocity. This clearly changed during the first industrial revolution of the 19th century, where lubricants became increasingly important, for instance, in ball bearings. It was Petrov,[5] Tower,[6] and Reynolds (1886) who established that the liquid viscous shear properties determine the frictional kinetics. Reynolds combined the pressure-gradient driven *Poisseuille flow* with the bearing surface induced *Couette flow* assuming a no-slip condition at the interface between lubricant and solid. This led to the widely used linear relationship between friction and velocity. Reynolds hydrodynamic theory of lubrication can be applied to steady state sliding at constant relative velocity, and transient decay sliding (sliding is stopped from an initial velocity v and a corresponding shear stress, τ_o, which leads to the classical Debye exponential relaxation behavior, i.e.:

$$\tau = \tau_o \exp\left(\frac{-\delta}{A\eta}t\right); \quad \tau_o \propto \frac{v\eta}{\delta}. \tag{3.2-1}$$

where δ is the lubricant thickness, A the area of the slider, and η the absolute viscosity of the lubricant. We will see below that this classical exponential relaxation behavior, which is obtained in a thermodynamically well-mixed three dimensional medium, is distorted when the lubricant film thickness is reduced to molecular dimensions.

Reynolds hydrodynamic description of lubrication was found to work well for thick lubricant films but to break down for thinner films. One manifestation is that for films on the order of ten molecular diameters, the stress in the film does not allow the tension to return to zero. It was also found that motion in the steady state sliding regime was disrupted, exhibiting a stick-slip-like slider motion.[7] Consequently, this non-Newtonian behavior was treated with a modified viscosity parameter (effective viscosity), which was comprised of the pressure, temperature and rate of shear.

The term *Boundary Lubrication* is used to describe a lubricant that is reduced in thickness to molecular dimensions. Hardy et al.[8] recognized that molecular properties, such as molecular weight and molecular arrangement (entropy), are governing the frictional force. This concept of confined lubrication, often visualized by two highly ordered opposing films with shear taking place somewhere between the two layers, contains many of the rate dependent manifestations of frictional sliding; e.g., stick-slip, ultra low friction, transitions from high to low friction, phase transitions, dissipation due to dislocations (e.g., gauche and cis-transformations), and memory effects.

Boundary-lubrication was found to be in many respects unique in that it deviates significantly from bulk-lubrication.[9] In macroscopic experiments, which involved rough surfaces, friction-velocity plots resembled logarithmic functions at moderate speeds. No static stiction force peaks were observed in boundary-lubricants close to zero speed. On the contrary, retractive slips could be observed upon halting, constituting a static friction coefficient that is exceeded by the dynamic friction coefficient.[9] These unique manifestations of boundary-lubrication were discussed in terms of a lubricated asperity-junction mechanism, which associated "an increase in the coefficient of friction with a decrease in the adsorptive coverage of the sliding surfaces by the lubricant."[9] It was argued that in the course of the sliding process of a macroscopic slider, more adsorbed lubricant is expected to exist within the interfacial area than outside. Upon halting, this would lead to a relaxation process of the elastic restraints on the slider, causing the slider to a retractively slip.

3.3 Thermal Activation Model of Lubricated Friction

Structural entropy was introduced above as one of the key players affecting frictional resistance in lubricants. Furthermore, the structural entropy is affected by the load of the slider, which contributes to an activation barrier in the form of a critical pressure.

Eyring discussed a pure liquid at rest in terms of a thermal activation model. The individual liquid molecules experience a *cage-like* barrier that hinders free molecular motion, because of the close packing in liquids. To escape from the cage, an activation barrier needs to be surmounted. In Eyring's model, two processes are considered in order to overcome the potential barrier: (i) shear stresses and (ii) thermal fluctuations. The potential barrier in the thermal activation model is depicted in Figure 3.3-1 indicating the modifications by the applied pressure force P, and shear stress τ.
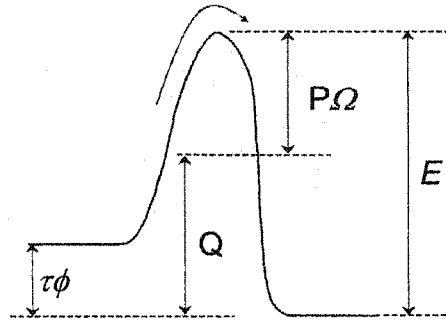
Figure 3.3-1. Potential barrier in a lubricant based on Eyring's thermodynamic "cage-model". The normal pressure, P, and the shear stress τ are modifying the barrier height, Q. Modified from Briscoe et al.[10]

Briscoe et al.[10] applied this idea to interpret the frictional behavior observed on molecularly smooth monolayer systems. Starting from the overall barrier height, $E = Q + P\Omega - \tau\phi$, that is repeatedly overcome during a discontinuous sliding motion, using a Boltzmann distribution to determine the average time for single molecular barrier-hopping, and assuming a regular series of barriers and a high stress limit ($\tau\phi / k_B T > 1$), the following shear strength versus velocity v relationship was derived:[10]

$$\tau = \frac{k_B T}{\phi} \ln\left(\frac{v}{v_o}\right) + \frac{1}{\phi}(Q + P\Omega). \tag{3.3-1}$$

The barrier height, E, is composed of the process activation energy Q, the compression energy $P\Omega$, where P is the pressure acting on the volume of the junction Ω, and the shear energy $\tau\phi$, where τ is the shear strength acting on the stress activation volume ϕ. T represents the absolute temperature. The stress activation volume ϕ can be conceived as a process coherence volume, and interpreted as the size of the moving segment in the unit shear process, whether it is a part of a molecule or a dislocation line. The most critical parameter in equation (3.3-1), v_o, is a characteristic velocity related to the frequency of the process and to a jump distance (discussed below).

From equation 3.3-1 the following iso-relationships can be directly deduced:[10]

$$\tau = \tau_o + \alpha P; \quad \tau_o = \frac{1}{\phi}\left(k_B T \ln\left(\frac{v}{v_o}\right) + Q\right); \quad \alpha = \frac{\Omega}{\phi}, \qquad \text{at constant } v, T \qquad (3.3\text{-}2a)$$

$$\tau = \tau_1 - \beta T; \quad \tau_1 = \frac{1}{\phi}(Q + P\Omega); \quad \beta = -\frac{k_B}{\phi}\ln\left(\frac{v}{v_o}\right), \qquad \text{at constant } P, v \qquad (3.3\text{-}2b)$$

$$\tau = \tau_2 + \theta \ln v; \quad \tau_2 = \frac{1}{\phi}(Q + P\Omega - kT \ln v_o); \quad \theta = \frac{k_B t}{\phi}, \qquad \text{at constant } P, T. \qquad (3.3\text{-}2c)$$

Thus, Eyring's model predicts a linear relationship of friction (the product of the shear strength and the active process area) in pressure and temperature, and a logarithmic relationship in velocity.

Eyring's model has been verified in lubrication experiments of solid (soap-like) lubricants by Briscoe and for liquid lubricants by He et al.[11] over three logarithmic decades of velocity. While Briscoe et al.[10] employed a SFA that confines and pressurizes the film over several square microns, He et al. used a SFM system in which the contact is on the order of the lubricant molecular dimension.

He et al. determined the degree of interfacial structuring and its effect on lubrication of n-hexadecane and octamethylcyclotetrasiloxane (OMCTS). For spherically shaped OMCTS molecules only an interfacial *monolayer* was found; in contrast, a 2 nm thick entropically cooled layer was detected for n-hexadecane in the boundary regime on an ultra-smooth silicon wafer. SFM measurements of the two lubricants (with similar chemical affinity to silicon) identified the molecular shape of n-hexadecane responsible for augmented interfacial structuring.

Consequently, interfacial liquid structuring was found to reduce lubricated friction. Again, as reasoned above, these results can be discussed in terms of a collective phenomenon, i.e. in terms of increased molecular coordination in n-hexadecane versus OMCTS.

3.4 Thermodynamic Models Based on Small, Non-Conforming Contacts

The SFM approach simulates a single asperity, or point, contact with a very high compliance, provided by a microfabricated, etched ultra-sharp tip and a typically soft cantilever spring. From a realistic, tribological perspective, the SFM approach is targeted towards the study of the intrinsic lubricant properties of a thin film in close vicinity to the solid substrate. The small contact area, on the order of the lubricant's molecular dimension, allows discussing SFM results in terms of a thermodynamic equilibrium. The area is insufficient in reorganizing the lubricant molecules coherently to cause an apparent material phase-transition or to generate a metastable situation as observed in SFA experiments (see below). Hence, SFM is not appropriate to reflect on tribological issues involving large area confinement effects.

In the molecular discussion of friction above, we introduced for solid and liquid lubrication a thermal activation model, the *Eyring model*, which employed a regular series of potential barriers. Note that the concept applies for both solid lubricants of an inherent, highly ordered structure[10] and also for a liquid system where a series of potentials is built up and overcome in the course of the shear process.[11]

Gnecco et al.[12] showed in a ultrahigh vacuum study on sodium chloride that the concept of the Eyring model also applies for dry SFM friction studies. Thus, a molecular theory of lubricated friction involving a molecular contact could be derived from a very simplistic model of an apparent sinusoidal-corrugated surface potential over which a cantilever tip is pulled. In a first attempt, one could assume that the corresponding wave length of the shear process corresponds to the apparent lattice spacing of the corrugated surface. However, such a simple attempt assumes there is no noise present, such as thermal noise, and thus, the driven tip leaves the total potential well when the barrier vanishes at the instability point. In the presence of noise, the transition to sliding can be expected to occur before the barrier peak is reached. Such barrier-hopping fluctuations have been theoretically discussed by Sang et al.[13] and Dudko et al.[14]

The relationship between thermal fluctuations and velocity must be handled thoughtfully. Sang et al. (2001) noted that, in previous considerations of thermal fluctuations by Heslot et al. (1994), the fluctuations were proportionally related to the velocity. This led to a friction force

that is logarithmically dependent on the velocity. In Heslot's *linear creep model*, the barrier height is proportional to the frictional force. Sang argued that if one considered an absorbing boundary condition (i.e. an elastic deformation of the overall potential which is accomplished by shifting the x-axis), the barrier height becomes proportional to a $3/2$-power law in the friction force. Sang's extended linear creep model resembles a *ramped creep model*, and leads analytically to the following logarithmic distorted dynamic friction-*versus*-velocity relationship of:

$$F_F = F_c - \Delta F_F \left| \ln v^* \right|^{2/3} \tag{3.4-1}$$

where v^* represents a dimensionless velocity, $\Delta F_F \propto T^{2/3}$, and F_c is an experimentally determined constant (by plotting F_F versus $T^{2/3}$ for a fixed ratio $T/v = 1$ K/(nm/sec)) that contains the critical position of the cantilever support. The same relationship of friction with velocity was also derived for the maximum spring force by Dudko et al.[14] ΔF_F and v^* in equation 4.6.4-1 were derived as follows by Sang:

$$v^* = 2\left(\frac{v\beta\omega_o^2 U_o}{k_B T\lambda} \right)\frac{\Omega_k^2}{\left(1-\Omega_k^4\right)^{1/2}}; \quad \Omega_k = \frac{\omega_o}{2\pi\omega_k}; \quad \omega_o = \sqrt{\frac{M\lambda^2}{U_o}}; \quad \omega_k = \sqrt{\frac{M}{k}} \tag{3.4-2a}$$

$$\Delta F_F = \frac{\pi U_o}{\lambda}\left(\frac{3}{2}\frac{k_B T}{U_o} \right)^{\frac{2}{3}}\left(\frac{\left(1-\Omega_k^4\right)^{\frac{1}{6}}}{1+\Omega_k^2} \right) \tag{3.4-2b}$$

In equations 3.4-2a,b, v is the velocity of the cantilever stage, β is the microscopic friction coefficient or dissipation (damping) factor, ω_o is the frequency of the small oscillations of the tip in the minima of the periodic potential, λ is the lattice constant, U_o is the surface barrier potential height, M and k represent the mass and the spring constant of the cantilever, respectively, and $2\pi\Omega_k$ represents the ratio of ω_o with the intrinsic cantilever resonance frequency ω_k. Although there is currently no experimental data available that would provide friction force measurements over a sufficiently large temperature and velocity regime to verify the *ramp creep model*, Sang's first rudimentary data extrapolation tests are promising.

The stronger supporting argument for the ramp creep model, relative to the experimental interpolation, is the comparison of the model to the numerical solution of the Langevin equation.

The Langevin equation combines the equation of motion (including the sinusoidal potential and perfect cantilever oscillator in the total potential energy, E, with thermal noise in the form of the random force, $\xi(t)$, i.e.:

$$M\ddot{x} + M\beta\dot{x} + \frac{\partial E(x,t)}{\partial x} = \xi(t)$$

(3.4-3)

$$\text{where} \quad E(x,t) = \frac{k}{2}(R(t) - x)^2 - U_o \cos\left(\frac{2\pi x}{\lambda}\right).$$

Equation 3.4-3 was solved numerically by both groups, Sang et al.[13] and Dudko et al.,[14] assuming a Gaussian fluctuation-dissipation relation, $<\xi(t)\xi(t')> = 2M\beta k_b T\delta(t-t')$ to express the random force. Sang confirmed the *ramped creep model* and Dudko showed that a force reconstruction approach from the density of states is equivalent with the Langevin equation. From the dynamic spectral analysis, it could be concluded that the locked states (states within the potential wells) contribute mostly to the potential component of the friction force that dominates at low velocities, and that the sliding states contribute to viscous friction dominating at high velocities.[14]

3.5 Creeping Friction Dynamics and Molecular Dissipation in Glassy Polymers

In the latest ambient scanning force microscopy (SFM) experiments and computer models, such as molecular dynamic (MD) and Monte Carlo (MC) simulations, molecular scale friction was discussed in terms of mechanical relaxations and internal conformational changes.[15-18] These studies involved highly structured model systems, which were prepared by either self-assembly or Langmuir-Blodgett techniques.[19] Such mono- or multilayered systems provide convenient access for investigations of molecular-scale dissipation mechanisms; e.g. load induced molecular tilts,[15] and reversible and irreversible conformation changes.[15-17] Simple frictional models, such as the Tomlinson-Prandtl model,[20] could be tested, and the corrugated molecular surface potential compared to the magnitude of discontinuous molecular stick-slip sliding.[16,18] The jump-distances were found to be stochastic above a critical sliding velocity, which led to a discussion of molecular friction in terms of fluctuations around discrete attractors.[18] This corresponds to recent theoretical treatments, i.e. *creep models*, that consider *barrier-hopping fluctuations* of periodic surface potentials with slips occurring at lower energy

values than prescribed by the potential barriers.[13,14,21] Here, we investigate the possibility that *hindered,* or *frozen,* relaxation states of an amorphous polymer, atactic polystyrene, could be activated in the course of a frictional sliding process, and thus, give rise to a barrier-hopping fluctuation not unlike the one observed for highly ordered surfaces.

Atactic polystyrene (PS) (Polymer Source, Inc., M_W=96.5k, M_W/M_N=1.04) was selected as a model polymer for its high monodispersity and phase homogeneity. The PS film was spin cast from a toluene solution onto a silicon wafer <1,1,1> and thermally annealed at 150°C for 2 hours under vacuum. The PS film thickness was ~220 nm, and the near surface glass transition temperature T_g was 373 K, measured with shear-modulated SFM.[22] SFM friction measurements were conducted with a Topometrics Explorer SFM using a bar shaped silicon cantilever (Nanosensors[TM], k_N = 0.139 N/m, k_T ~ 80 N/m), and under nitrogen with the relative humidity below ~7%. The instrument and cantilever were calibrated on a silicon wafer <1,1,1> according to the procedure by Buenviaje et al.[23] Measurements were performed over 2.0 μm scan range with a 20 nm line-spacing to avoid memory effects from previous scans.

Isothermal friction-velocity curves are presented in Figure 3.5-1 for temperatures between 300-365 K. Quasi-logarithmic friction-velocity relationships are found, which is in accordance with recently developed theoretical models,[10,13,14,21] and resemble SFM experiments on ionic crystals in ultrahigh vacuum[12] and in lubricated sliding.[11]
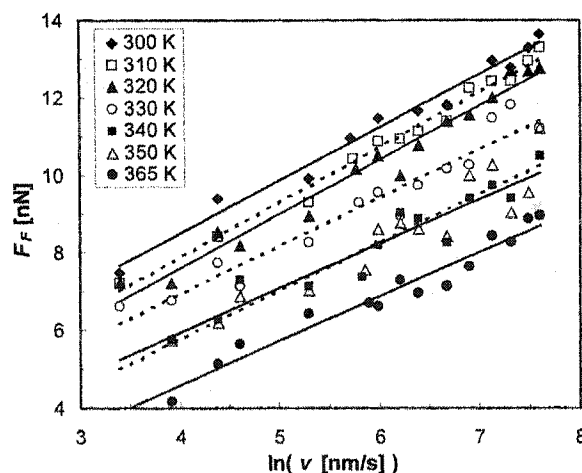
Figure 3.5-1: Friction force – scan velocity relationship on glassy polystyrene at various temperatures indicated in the legend and under a normal force of 15±2 nN. The scan velocity was varied between 30 and 2000 nm/s at each temperature, over a range of 300 to 365 K.

Based on the *linear creep model* by Heslot, the friction between two contacting surfaces with constant potential bias depends logarithmically on the sliding velocity, i.e. $F_F \propto const + \ln(v)$, where v represents the slider support velocity.[21] An extension to this model, the *ramped creep model*, independently proposed by Dudko et al. and Sang et al.,[13,14] considers that the SFM tip support is also moving, resulting in a potential bias that is continuously ramped up. Thus, the barrier height becomes proportional to a 3/2-power law in the friction force.[13,14] This modification to the linear creep model leads to a logarithmically power-law distorted friction-velocity relationship of $F_F = F_c - \Delta F_F |\ln v^*|^{2/3}$. From Sang, $v^* \propto v/T$ represents a dimensionless velocity, and $\Delta F_F \propto T^{2/3}$. F_c is an experimentally determined constant that contains the critical position of the cantilever support. F_c is determined from the intercept of F versus $T^{2/3}$ and from F_F versus T for ramped and linear creep, respectively, both at a fixed ratio $T/v = 1$ K/(nm/s).[13] The combination of these relationships suggests the collapse of $F_F(v)|_T$ curves obtained at different temperatures.

This scaling model was shown to be in accordance with the solution of the Langevin equation

$$M\ddot{x} + M\beta\dot{x} + \frac{\partial E(x,t)}{\partial x} = \xi(t),$$ (3.5-1)

where x is the position of the tip on the surface, M is the mass of the SFM tip, and β is a linear dampening factor (*microscopic friction coefficient*). Equation 3.5-1 assumes a sinusoidal surface potential and perfect cantilever oscillator in the total potential energy E, with thermal noise in the form of the random force, $\xi(t)$, where $<\xi(t)\xi(t')> = 2M\beta k_b T\delta(t-t')$.[13,14] We successfully tested the scaling models with our amorphous glassy PS friction measurements in Figure 3.5-1. The results are presented in Figures 3.5-2 and 3.5-3. The ramped creep model, Figure 3.5-2, provides a marginally better fit compared to the linear creep model, Figure 3.5-3. The fit quality of the ramped creep model relative to the linear creep model is expected to increase for a system that is less overdamped, i.e. a stiffer spring with respect to β,[24] and with measurements over larger velocity and temperature ranges.
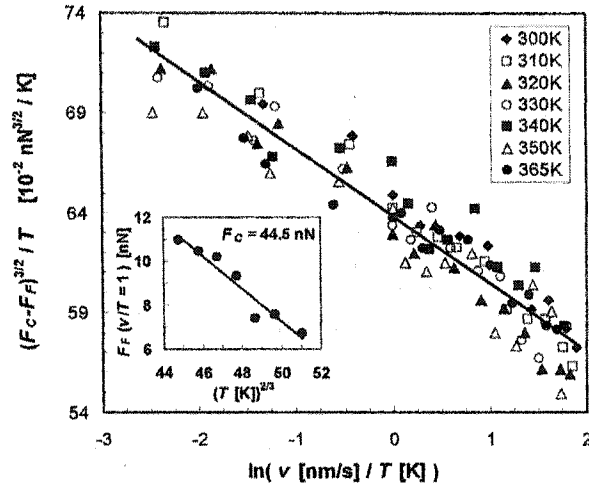
Figure 3.5-2: Collapse of the friction data from Figure 3.5-1 using a ramped creep scaling model.[13] The linear regression parameters are reported in the upper inset (R^2=0.9124). Lower inset: the constant F_c is determined from the intercept of F_F versus $T^{2/3}$ for a fixed ratio $T / v = 1$ K/(nm/s):[13] $F_c = 44.5$ nN.
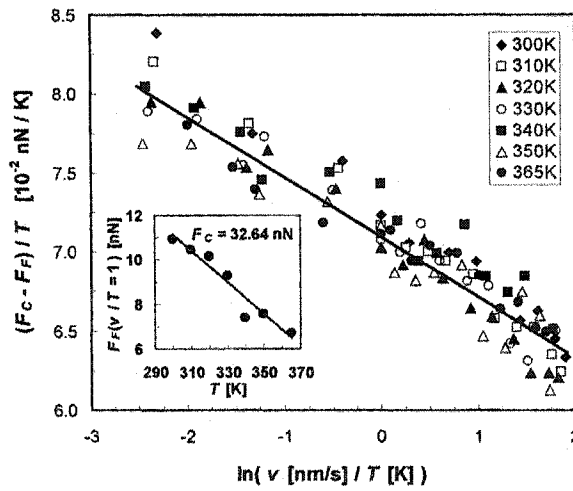
Figure 3.5-3: Collapse of the friction data from Figure 3.5-1 using a linear creep scaling model.[21] The linear regression parameters are reported in the upper inset (R^2=0.909). Lower inset: the constant F_c is determined from the intercept of F_F versus T for a fixed ratio $T / v = 1$ K/(nm/s):[13] $F_c = 32.6$ nN.

At this point, it would be desirable to identify the potential barrier responsible for frictional losses of a nanoscopic SFM tip sliding over the amorphous PS surface. Recognizing the *quasi-parallelism* of the $F(v)|_T$ curves in Figure 3.5-1, we employed the method of reduced variables to superpose the data into a master curve.[25] This *linear* approach serves to decouple the thermal and rate contributions to the friction force, similar to the well known Williams-Landel-Ferry (WLF) equation applied to viscoelastic behaviors of polymers above the glass transition.[25] The superposed data, from a single horizontal shift defining the a_T shift factor, are shown in Figure 3.5-4. The thermal dependence of the a_T shift factor in the inset of Figure 3.5-4 identifies the frictional process as an activation process. From the Arrhenius behavior of a_T, the representative barrier height U_0 is 7.0 kcal/mol. This value corresponds to the activation energy of the phenyl rotation around the C-C bond to the backbone chain in atactic PS, 7.0 kcal/mol.[26] Thus, the primary dissipation mechanism for *dry* sliding of a nanoscopic tip on glassy PS is through rotation of the phenyl groups.
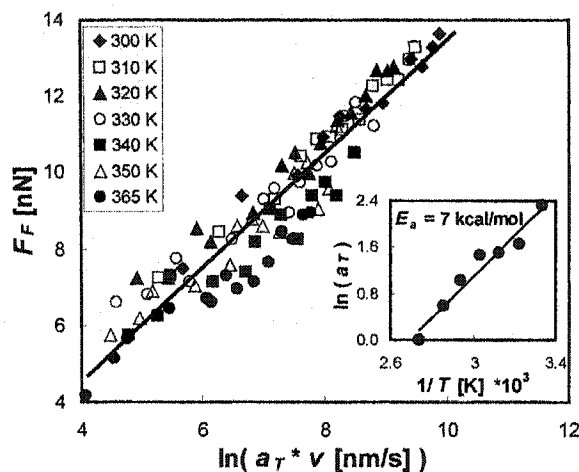
Figure 3.5-4: Superposed friction master curve from data of Figure 3.5-1. (inset) Thermal a_T shift factor. An activation engergy of 7.0 kcal/mol is deduced from Arrhenius behavior of a_T, corresponding to the activation of phenyl rotation in atactic PS.

Considering that the creep models (a) fit the friction data reasonably well, and (b) are in accordance with a fluctuation model based on a Gaussian fluctuation distribution, we may conclude that there is little or no correlation between the individual phenyl rotations that are

relaxed during the sliding motion. It is because of this weak correlation that similar frictional dissipative behaviors are observed on both highly structured (crystalline) surfaces and the unstructured (amorphous) PS surface.

The rotation of phenyl groups in atactic PS has been attributed to the γ relaxation.[27] Considering that other relaxations are possible (e.g. δ, β, and α with respective activation energies of 2-3, 35, and 90 kcal/mol),[28] one would expect that depending on the load and contact area, i.e. the degree of size and pressure confinement, friction could also originate from other relaxations. For example, Hammerschmidt et al. have identified the β relaxation as the primary dissipation mechanism in SFM friction measurements on poly(methyl methacrylate).[29] As long as the individual relaxation processes are uncorrelated, it is reasonable to assume that the current creep models will apply to describe friction on a broad range of polymer molecules. Any deviations from the model could be attributed to memory effects within the system.

3.6 Chapter Summary

These results and the associated discussion of molecular friction mechanisms on a glassy polymer system illustrate the effectiveness of rudimentary non-equilibrium models that incorporate simple potentials with thermal fluctuations. The combination of polymer relaxation data, available from transition studies, with either of the two creep models should provide a vast array of possible outcomes for friction values involving single asperity contacts. Deviations from the models are expected, particularly for correlated fluctuations, i.e. memory effects in relaxation processes. Addressing the issue of the so called non-Markovian behavior of sliding systems demands a more rigorous theoretical treatment, such as the generalized Fokker-Planck equation with a system specific statistical kernel.[30-33] It is interesting to note, for Gaussian systems, Dudko et al. showed that a force reconstruction approach from the density of states, accumulated from the corresponding Fokker-Planck equation, is equivalent with the solution of the Langevin equation, Equation 3.5-1.[14] The applicability of this work reaches beyond the scope of traditional tribology. It promises groundbreaking nanorheological analysis of molecular systems, in which there is a competition between the rate of thermally assisted escape from the trapped state and the pulling rate, as found, for instance, in the study of bond rupturing and unfolding of complex biological molecules.[34]

36

3.7 Notes to Chapter 3

[1]   N. P. Suh, *Tribophysics* (Prentice-Hall, Inc., Englewood Cliffs, NJ, 1986).

[2]   F. P. Bowden and D. Tabor, *The friction and lubrication of solids* (Clarendon Press, Oxford, 1951).

[3]   D. Tabor and R. H. S. Winterton, *Proc. R. Soc. Lond.* A312, 435 (1969).

[4]   G. Binnig, C. F. Quate and C. Gerber, *Phys. Rev. Lett.* 56, 930 (1986).

[5]   N. P. Petrov, *Friction in Machines and the Effect of the Lubricant* (St. Petersburg, 1883).

[6]   B. Tower, *Proc. Inst. Mech. Engrs* Nov., 632 (1883).

[7]   J. Israelachvili, M. P., M. Gee, A. Homola, M. Robbins and P. Thompson, *J. Phys.: Condens. Matter* 2, 89 (1990).

[8]   W. B. Hardy and I. Doubleday, *Proc. Roy. Soc.* A 100, 550 (1922).

[9]   A. Dorinson and K. C. Ludema, *Mechanics and Chemistry in Lubrication* (Elsevier, Amsterdam, 1985).

[10] B. J. Briscoe and D. C. B. Evans, *Proc. R. Lond. A* 380, 389 (1982).

[11] M. He, A. Szuchmacher Blum, G. Overney and R. M. Overney, *Phys. Rev. Lett.* 88, 154302/1 (2002).

[12] E. Gnecco, R. Bennewitz, T. Gyalog, C. Loppacher, M. Bammerlin, E. Meyer and H.-J. Güntherodt, *Phys. Rev. Lett.* 84, 1172 (2000).

[13] Y. Sang, M. Dube and M. Grant, *Phys. Rev. Lett.* 87, 174301/1 (2001).

[14] O. K. Dudko, A. E. Filippov, J. Klafter and M. Urbakh, *Chemical Physics Letters* 352, 499 (2002).

[15] J. I. Siepmann and I. R. McDonald, *Phys. Rev. Lett.* 70, 453 (1993).

[16] T. Bonner and A. Baratoff, *Surf. Sci.* 377-379, 1082 (1997).

[17] P. T. Mikulski and J. A. Harrison, *J. Am. Chem. Soc.* 123, 6873 (2001).

[18] R. M. Overney, H. Takano, M. Fujihira, W. Paulus and H. Ringsdorf, *Phys. Rev. Lett.* 72, 3546 (1994).

[19] A. Ulman, *An Introduction to Ultrathin Organic Films* (Academic Press, New York, 1991).

[20] G. A. Tomlinson, *Philos. Mag. Ser.* 7, 905 (1929).

[21] F. Heslot, T. Baumberger, B. Perrin, B. Caroli and C. Caroli, *Phys. Rev. E* 49, 4973 (1994).

[22] R. M. Overney, C. Buenviaje, R. Luginbuhl and F. Dinelli, *Journal of Thermal Analysis and Calorimetry* 59, 205 (2000).

[23] C. K. Buenviaje, S. R. Ge, M. H. Rafailovich and R. M. Overney, *Mat. Res. Soc. Symp. Proc.* 552, 187 (1998).

24   M. G. Rozman, M. Urbakh and J. Klafter, *Physica A* **249**, 184 (1998).

25   J. D. Ferry, *Viscoelastic Properties of Polymers*, 3rd ed. (John Wiley, New York, 1980).

26   S. Reich and A. Eisenberg, *J. Poly. Sci. A-2* **10**, 1397 (1972).

27   O. Yano and Y. Wada, *J. Poly. Sci. A-2* **9**, 669 (1971).

28   R. F. Boyer and S. G. Turley, in *Molecular basis of transitions and relaxations*, edited by D.J.Meier (Gordon and Breach Science Publishers, New York, 1978), pp. 333.

29   J. A. Hammerschmidt, W. L. Gladfelter and G. Haugstad, *Macromolecules* **32**, 3360 (1999).

30   R. Metzler and J. Klafter, *Phys. Reports* **339**, 1 (2000).

31   R. Metzler and J. Klafter, *Physica A* **302**, 290 (2001).

32   I. M. Sokolov, *Phys. Rev. E* **63**, 011104/1 (2000).

33   W. D. Luedtke and U. Landman, *Phys. Rev. Lett.* **82**, 3835 (1999).

34   D. Keller, D. Swigon and C. Bustamante, *Biophys. J.* **84**, 733 (2003).

4. Mesoscopic Mobility: Molecular Evolution of the Glass Transition

4.0 Overview

Significant effort is currently directed towards a fundamental understanding of the dynamics and kinetics in glass forming polymer liquids.[1-3] The study of the glass transition is technologically and fundamentally strongly motivated. Particularly, investigating the finite size limited structural relaxations near the glass transition is central to nanotechnological applications. Since Adam and Gibbs,[4] the structural relaxation near the glass transition temperature, T_g, is envisioned in terms of the cooperative motion of polymer segments or domains. Over the last four decades, extensive research has targeted the length scale for cooperative motion as the essence of understanding the glass transition.[3,5] Despite the predicted increase in the cooperative length scale on cooling towards T_g, the structure of a glass former changes only slightly.[6,7] This disqualifies many *structure-sensitive* instrumental techniques, such as scattering, for investigating cooperative motion. One technique that has recently shown great potential for glass transition analyses of finite size limited polymers is shear modulation force microscopy (SM-FM) (see section 9.4). Although this thermomechanical method accurately provides the phenomenological quantity T_g, it lacks the molecular dynamics information generally furnished by spectroscopic techniques. Here we introduce lateral force microscopy, originally designed for nanotribological studies,[8] as a technique that provides the crucial link between the spectroscopic and nanoscopic phenomenological analyses. We demonstrate that activation energies related to molecular mobilities in the vicinity of T_g can be deduced and that the temperature dependent length scale for cooperative motion near T_g can be directly inferred with the combination of dielectric data.

4.1 Mesoscopic Polymer Dynamics and Cooperative Motion Near the Glass Transition

The complex dynamics observed in the glass transition region have been attributed to mesoscopic thermodynamic fluctuations.[9] Various theories have conceded the concept of cooperative segmental motion by considering: environmental fluctuations, local density fluctuations (*flickering* of fluidized domains), extended Adam-Gibbs thermodynamic fluctuations, cooperatively rearranging domains (Adam-Gibbs), and various two-fluid models.[3] The length scale for cooperative motion of the α-relaxation is predicted to be on the nanometer scale, involving ~100 monomer segments.[3] Most spectroscopic techniques lack the spatial

resolution necessary for probing the length scale of the relaxation domains.[3] Currently, only 4D NMR studies have provided direct experimental access to the size of the dynamically heterogeneous clusters.[10] However, depending on the cluster size, any number of relaxation events may occur within each cluster. To our knowledge, there has been no prior direct experimental evidence for the temperature dependent length scale of cooperative motion associated with each particular relaxation event.

A mesoscopic description of polymer dynamics involves, in general, only two parameters: an appropriate molecular length scale and the internal, or monomeric, friction coefficient.[11] So far, internal frictional properties have not been accessible with conventional tribological techniques, such as lateral force microscopy (LFM). However, LFM has evolved into a widely used chemically distinctive nano-tool[8] and a truly atomic/molecular scale tribological apparatus.[12,13] It has been shown that the LFM cantilever, with its integrated nanometer-sharp tip, is capable of probing a single surface potential well and addressing the barrier hopping dynamics that govern sliding friction between contacting solids[14] and *interfacially cooled* liquids.[15] In this section, we demonstrate how LFM, in combination with dielectric spectroscopy, offers access to both the characteristic length scales and the internal friction properties of polymer systems, and provides insight into the molecular origins and evolution of the glass transition.

The dynamic polymer friction results in section 3.5 have revived the question of to what degree is LFM sensitive to intrinsic material properties, such as the monomeric friction coefficient, as opposed to extrinsic tribological attributes. This question dates as far back as 1966,[16] where Ludema and Tabor attempted to deduce intrinsic properties of rubbery materials from friction-velocity, $F_F(v)$, relationships. A qualitative schematic of the $F_F(v)$ behavior found by Ludema and Tabor is presented in Figure 4.0-1A. They recognized the characteristic peak in the $F_F(v)$ curve as having some intrinsic material origin, although their attempt to deduce intrinsic properties failed.

With LFM, it is possible to deduce intrinsic relaxation properties from the characteristic $F_F(v)$ peaks presented in superposed form in Figure 4.0-1b. The $F_F(v)$ peak is explained by the interplay of two dominating time scales: the extrinsic observation time scale, τ_e, dictated by the sliding velocity, v, and the intrinsic material response time, τ_m. In the region of the $F_F(v)$ peak, the two competing processes occur on comparable time scales. The friction force increases or decreases with increasing sliding velocity depending on whether the extrinsic time scale trails or leads the material response time, respectively. The $F_F(v)$ peak is analogous to the loss peak in

dielectric spectroscopy, where the maximum absorption occurs when the electric field frequency, τ_e^{-1}, matches the time scale of segmental motion, τ_m. However, the friction peak is distinguished by a velocity as opposed to a frequency; thereby coupling a characteristic length scale with the characteristic time scale.
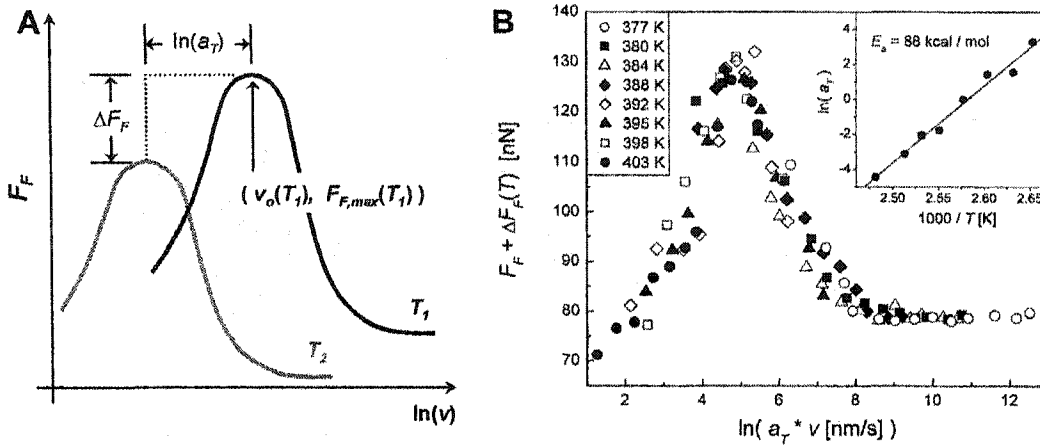
Figure 4.0-1: Friction force-velocity, $F_F(v)$, isotherms for polymers. (A) Generic $F_F(v)$ isotherms with $T_1 > T_2$. The maximum friction intensity, $F_{F,max}$ at v_o is a reference point for plots obtained at different temperatures. (B) $F_F(v)$ isotherms for PS above the glass transition temperature ($T_g = 373K$), superposed using the method of reduced variables. The thermal a_T shift factor was determined for a reference temperature of 388K. A vertical ΔF_F-shift was only necessary within the heterogeneous regime, (see Figure 4.0-3) The Arhenius behavior of a_T reveals an activation energy, E_a, of 88 kcal/mol., corresponding to the α-relaxation process of unlocked backbone mobility.

The significant difference between the original macroscopic study by Ludma and Tabor and the nanoscopic study presented here is the confining length scale of the experiment. Sliding experiments on compliant materials with a contact area exceeding the molecular length scale are destined to produce metastable material configurations, which give rise to externally induced tribological characteristics. To avoid metastable artifacts, thus achieving sensitivity to intrinsic material properties, we chose a probing tip with a contact radius on the order of the polymer radius of gyration (~ 8 nm).

The LFM measurements were conducted on a 156 ± 8 nm thick film of atactic polystyrene (PS) (Polymer Source, Inc., $M_W = 96.5k$, $M_W/M_N = 1.04$). The film was spin cast from a cyclohexanone (Mallinckrodt Baker, Inc.) solution onto a silicon wafer, and thermally annealed at 160°C for 4 hours under vacuum. Friction measurements were conducted with a scanning force microscope (Explorer, Veeco Instruments) using a bar shaped silicon cantilever

(Nanosensors[TM], $k_N = 0.164$ N/m, $k_T \sim 80$ N/m), and under nitrogen with a relative humidity below ~7 %. The applied load ranged from ~102 to 36 nN, and the corresponding normal forces, including adhesion, were 31 to 373 nN. The friction force, F_F, was determined from the hysterisis in the lateral deflection signal between forward and reverse scans.[17,18] Scanning was performed over 2.0 μm range with a 20 nm line-spacing to avoid memory effects from previous scans. Isothermal friction-velocity curves were recorded over a velocity range of 0.01 to 20 μm/s, for temperatures between 377 and 403 K. SM-FM measurements revealed a glass transition temperature of 373 K.

In section 3.5, it was shown that LFM is especially well suited for ascertaining the time (rate) and temperature coupling of viscoelastic behaviors of glassy atactic polystyrene (below T_g). The dissipative mechanism for the sliding process was identified as an *intra*-molecular relaxation. Specifically, the hindered rotation of phenyl rings about the C-C bond with the backbone were activated during the course of frictional sliding, pictured in Figure 4.0-2.

As polystyrene is heated above its T_g, the activation barrier increases by one order of magnitude, from 7 to 88 kcal/mol. This is determined from the Arrhenius behavior of the a_T shift factor in the inset of Figure 4.0-1b, and coincides with the 90 kcal/mol activation energy for the α-relaxation process.[19] In molecular terms, the α-relaxation is the unlocking of backbone mobility and dissipation through oscillations and or rotations of phenyl groups around the axis of the backbone chain, pictured in Figure 4.0-2. In this light, the characteristic friction peak in Figure 4.0-1b may be referred to as the α-relaxation peak, or the α-peak.
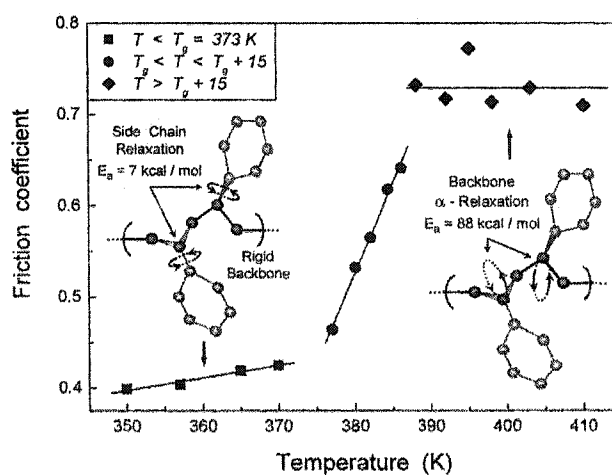
Figure 4.0-2: The polystyrene friction coefficient (friction force normalized by applied load) illustrates a transition in the dissipation mechanism from side chain relaxation in the glass phase to backbone relaxation in the melt phase. The transition ocurs over a 15 K region, starting at T_g, and indicates the heterogeneous nature of the glass transition.

The continuity of a_T in the inset of Figure 4.0-1b indicates that the α-relaxation commences at T_g and persists throughout the studied temperature range. However, within this range, the frictional response in Figure 4.0-2 reveals two distinct regimes: a transition regime between the glass and melt with a strongly temperature dependent friction coefficient, indicative of the heterogeneous nature of the glass transition; and a fully developed rubbery melt regime starting at $T > T_g + 15$ °C, which exhibits a temperature independent friction coefficient.

Inspection of the α-peak intensity, $F_{F,max}(T)$ from Figure 4.0-1b, reveals in Figure 4.0-3, the maturation of the α-relaxation for temperatures increasing from T_g to $T_g + 15$K. The strong 4.8 nN/K temperature dependence of $F_{F,max}$ in the transition regime is, in essence, caused by the heterogeneity of two structural phases, i.e. the glassy and melt phases. This is corroborated in Figure 4.0-2 by the quasi-continuous transition from lower energy dissipation through side chain relaxations in the glass ($T < T_g$) to higher energy dissipation through α-relaxations in the fully developed melt ($T > T_g + 15$K). Conceptually, small domains of the melt phase begin to appear at T_g, yielding a relatively weak α-peak intensity. As the temperature increases, remnant glassy domains are consumed by the melt and the and the α-peak intensity increases. Once the fully developed melt is achieved at $T > T_g + 15$K, the homogeneous melt is characterized by the temperature independent α-peak intensity. The existence of structural heterogeneity around T_g is consistent with conclusions drawn from multidimensional nuclear magnetic resonance (NMR), dielectric spectroscopy, photobleaching, dynamic light scattering, and quasi-elastic neutron scattering studies.([3] and references therein)
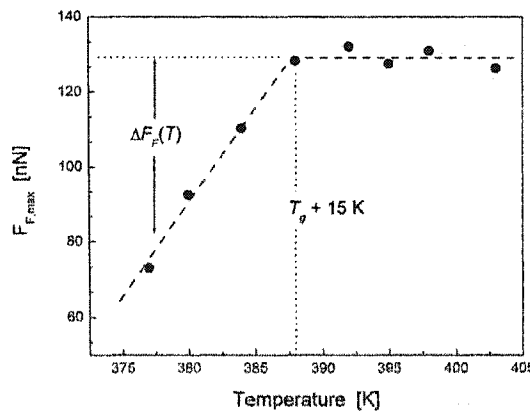
Figure 4.0-3: The growing intensity of the friction peak, $F_{F,max}(T)$, through the glass transition region, $T = T_g$ (373 K) → $T_g + 15$ (388 K), indicates the heterogeneous nature of the transition process. The dilution of the peak intensity in the transition region suggests the presence of the lower energy dissipation side chain relaxation associated with the glassy state. $ΔF_F(T) = F_{F,max}(T>T_g+15) - F_{F,max}(T)$.

To address the length scale for cooperative motion during the α-relaxation, we combined the friction force data presented here with α-relaxation time measurements from dielectric spectroscopy[20] for PS of comparable molecular weight (M_W = 90.0k, M_W/M_N=1.06), Figure 4.0-4. We define the length scale for cooperative α-relaxations as $\xi_\alpha(T) = v_o(T) \cdot \tau_\alpha(T)$, where $v_o(T)$ is the velocity corresponding to the α-peak of the $F_F(v)$ curves in Figure 4.0-1b, and $\tau_\alpha(T)$ is the α-relaxation time. The resulting cooperation length is presented in the inset of Figure 4.0-4, and is discussed with greater detail in Figure 4.0-5.
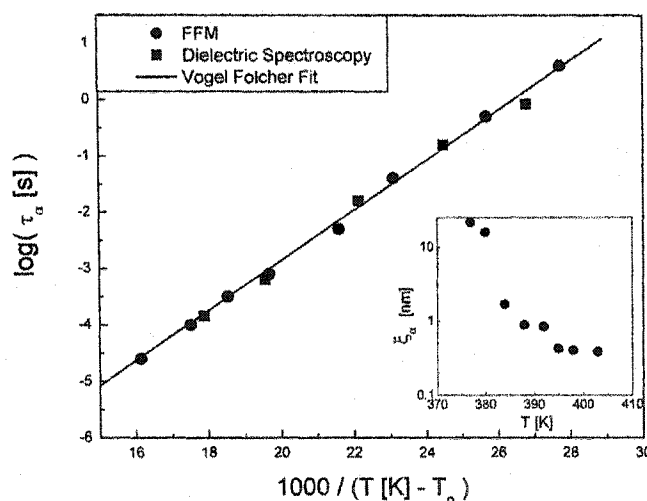
Figure 4.0-4: Polystyrene α-relaxation times, τ_α, determined from the LFM friction peak compared to the dielectric spectroscopy measurements of [20]. The solid line is the fit of the Vogel-Fulcher equation, $\tau(T) = \tau_o \exp(B/(T-T_o))$, to the relaxation times (τ_o = 2.4*10^{-12}, B = 1005, T_o = 341.3 K), which expresses the non-Arrhenius behavior of the α-relaxation time. (inset) Temperature dependence of length scale of cooperative motion during the α-relaxation of the polystyrene backbone, ξ_α.

It is important to note that the determination of the cooperation length in Figure 4.0-4 did not involve any of the many theoretical models. The cooperation length increases from 3 Å to 18 Å for temperatures decreasing from the fully developed melt to ~384 K, respectively. The functional relationship of $\xi_\alpha(T)$ within this temperature range, provides, to our knowledge, the first model independent experimental confirmation of Donth's fluctuation theory.[21] Donth's theory predicts a $\xi_\alpha(T)$ relationship of the form: $\xi_\alpha(T) \sim (T-T_o)^{-\nu}$, ($\nu$ = 2/3 for a three-dimensional system). The fit of our data with this fluctuation theory is shown in Figure 4.0-5.
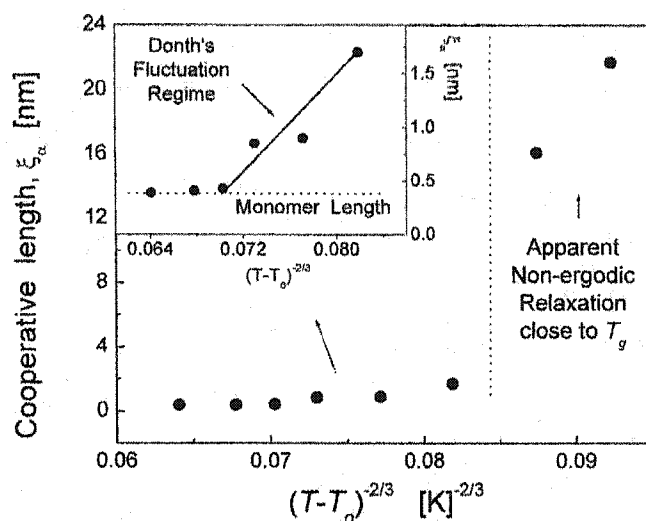
Figure 4.0-5: The length scale for cooperative motion during α-relaxation events in atactic polystyrene near T_g. The data are expressed in the form of Donth's fluctuation theory, and reveal an apparent non-ergodic relaxation behavior very close to T_g. (inset) Zoom into the higher temperature data reveals the monomer length as the low limit.

Figure 4.0-5 also illustrates that the cooperation length deviates significantly from the fluctuation theory very close to T_g, i.e. between T_g and ~384 K. Based on light-scattering studies by Fischer and co-workers, long-range density fluctuations are expected in the vicinity of T_g. These *far-field* effects involve slow relaxations, $\tau_{slow}=10^7 \tau_\alpha$, with a cooperation length up to two orders of magnitude larger than the characteristic length of the α-relaxation discussed above.[2,22] Although our experiment, based on its small contact size and experimentally applicable velocities, should be insensitive to such long-range density fluctuations, the slow process has been attributed to apparent non-ergodic time averaged correlations that occur on the time scale of the α-relaxation.[2] Thus, we believe that the significant increase of the correlation length below 384 K results from an apparent non-ergodic behavior on the time scale of the α-relaxation.

4.2 Chapter Summary

With LFM, we have provided fundamental insight into the intrinsic friction behaviors of polymers, and answered the long standing question regarding the sensitivity of LFM to intrinsic polymer properties. The LFM results confirmed the heterogeneity of the glass transition, and provided direct experimental access to the temperature dependent length scale for cooperative

motion during the α-relaxation process. In the fully developed melt state, the cooperative lengths are consistent with theoretical predictions and offer experimental confirmation of Donth's fluctuation theory. Very close to T_g, the relaxation, the cooperative lentgh deviates from Donth's theory, which supports the prediction of a slow process close to T_g and an apparent non-ergodic behavior.

Increasing the LFM probe-contact size to that of the non-ergodic length scale (by a factor of 3) should increase sensitivity to the slow process, and provide valuable insight into the exotic non-ergodic behaviors. Furthermore, cooperative motion in dimensionally constrained systems (see Chapter 5) may be addressed by considering a reduction in the fractal dimension from 3 towards 2 and modifying the exponent in Donth's fluctuation theory, i.e. replacing $v = 2/3$ with $v = 2/D_f$, where D_f is the fractal dimension.

46

4.3 Notes to Chapter 4

[1]   J. Rault, *Journal of Physics: Condensed Matter* **15**, 1193 (2003).

[2]   A. Patkowski, H. Glaser, T. Kanaya and E. W. Fischer, *Physical Review E (Statistical, Nonlinear, and Soft Matter Physics)* **64**, 031503 (2001).

[3]   H. Sillescu, *J. Non-Crystalline Solids* **243**, 81 (1999).

[4]   G. Adam and J. H. Gibbs, *J. Chem. Phys.* **43**, 139 (1965).

[5]   C. Bennemann, C. Donati, J. Baschnagel and S. Glotzer, *Nature* **399**, 246 (1999).

[6]   J. A. Forrest and J. Mattsson, *Physical Review E (Statistical Physics, Plasmas, Fluids, and Related Interdisciplinary Topics)* **61**, 53 (2000).

[7]   F. Varnik, J. Baschnagel and K. Binder, *European Physical Journal E* **8**, 175 (2002).

[8]   R. M. Overney, E. Meyer, J. Frommer, D. Brodbeck, R. Luethi, L. Howald, H. J. Guentherodt, M. Fujihira, H. Takano and Y. Gotoh, *Nature (London)* **359**, 133 (1992).

[9]   F. Bueche, *J. Chem. Phys.* **30**, 448 (1959).

[10]   U. Tracht, M. Wilhelm, A. Heuer, H. Feng, K. Schmidt-Rohr and H. W. Spiess, *Phys. Rev. Lett.* **81**, 2727 (1998).

[11]   V. N. Pokrovskii, *The Mesoscopic Theory of Polymer Dynamics* (Kluwer Academic Publishers, Dordrecht, 2000).

[12]   R. M. Overney, H. Takano, M. Fujihira, W. Paulus and H. Ringsdorf, *Phys. Rev. Lett.* **72**, 3546 (1994).

[13]   E. Gnecco, R. Bennewitz, T. Gyalog, C. Loppacher, M. Bammerlin, E. Meyer and H.-J. Güntherodt, *Phys. Rev. Lett.* **84**, 1172 (2000).

[14]   E. Riedo, E. Gnecco, R. Bennewitz, E. Meyer and H. Brune, *Physical Review Letters* **91**, 084502 (2003).

[15]   M. He, A. Szuchmacher Blum, G. Overney and R. M. Overney, *Phys. Rev. Lett.* **88**, 154302/1 (2002).

[16]   K. C. Ludema and D. Tabor, *Wear* **9**, 329 (1966).

[17]   R. Overney and E. Meyer, *MRS Bulletin* **XVIII**, 26 (1993).

[18]   C. K. Buenviaje, S. R. Ge, M. H. Rafailovich and R. M. Overney, *Mat. Res. Soc. Symp. Proc.* **552**, 187 (1998).

[19]   R. F. Boyer and S. G. Turley, in *Molecular basis of transitions and relaxations*, edited by D. J. Meier (Gordon and Breach Science Publishers, Inc., New York, 1978), pp. 335.

[20]   C. M. Roland and R. Casalini, *J. Chem. Phys.* **119**, 1838 (2003).

[21]   E. Donth, *J. Non-Cryst. Solids* **53**, 325 (1982).

[22]   T. Kanaya, A. Patkowski, E. W. Fischer, J. Seils, H. Glaser and K. Kaji, *Macromolecules* **28**, 7831 (1995).

5. Interfacial Confinement: Rheological Boundary Layers

5.0 Overview

The laws of nature, or more appropriately, their perception in the form of physiochemical material properties, become challenged when a three-dimensional bulk material is confined to only two dimensions. This is apparent in many interfacial applications, such as thin film technologies. Interfacial technologies are trapped between the atomistic and the three-dimensional bulk regimes – in the mesoscale. Here, the phenomenological classifications applied macrosystems breakdown. On the other hand, quantum or molecular theories are insufficient in describing the fractal-like behavior of mesoscopic systems. Interfacial constraints generate frustrated, or poorly mixed, systems, in which equilibration processes are severely impeded. These systems are best described with non-equilibrium statistical mechanical models for constrained small ensemble systems.

In polymer thin films, when film thicknesses approach the nanometer scale, structural, material, and transport properties become increasingly dominated by interfacial and dimensional constraints. Various groups have reported bulk-deviating structural and dynamic properties for polymers at interfaces.[1-7] For example, reduced molecular mobility in ultrathin polystyrene films was reported based on forward recoil spectroscopy measurements.[1] Furthermore, in secondary ion mass spectrometry (SIMS) and scanning force microscopy (SFM) studies of polystyrene and polyethylene-co-propylene systems, it was found that the degree of molecular ordering significantly affects dynamic processes at interfaces.[2]

An aspect that is ignored with classical mean-field theoretical considerations of thin films is the possibility of conformational changes due the film preparation process.[7] In the past, one considered substrate effects to be confined to the pinning regime, typically on the order of a few nanometers. However, recent SFM experiments have revealed that the spin casting process alters the structural properties of polyethylene-co-propylene at silicon interfaces, leading to an anisotropic molecular diffusion process.[8] Thermal annealing has been found inadequate to relax process-induced structural anisotropy in confined polymer systems because of insufficient *mixing* at the interface.[8] Consequently, depending on the proximity to the substrate, i.e. film thickness, the molecular mobility and relaxation properties of the polymer may be altered during the preparation process.

48

Rheological boundary layers are often formed at interfaces, within which, anisotropic constraints lead to bulk-deviating behaviors. This chapter is devoted to exploring rheological boundary layers at polymer interfaces. A variety of rheological manifestations are illustrated, and a visualization of the molecular configuration within interfacial boundaries is gradually developed.

5.1 Interfacial Plasticization

The conceptually intuitive process of heterogeneous diffusion serves as worthy starting point for a discussion about rheologically modified interfacial boundary layers. This is illustrated for a multiphase binary thin film system, in which, low molecular weight components (LMCs) leach from an underlying film into the surface film, forming an interdiffusion zone at the interface. LFM studies were conducted on poly(methyl methacrylate) (PMMA) films supported on either crosslinked epoxy or Si substrates.

For PMMA films on epoxy substrates, the friction coefficient, μ, in Figure 4 decreases with increasing film thickness, and for thicker films, approaches the friction value of PMMA on Si. The friction coefficient may be considered constant on all films, if one assumes that (a) the shear modulus is constant, and (b) the adhesion force is only a function of the contact area, i.e. a constant physical and chemical bonding strength between the LFM tip and sample. Holding to these assumptions and considering that the LFM probe (Si) is much stiffer than PMMA, it follows that changes in μ reflect changes in the PMMA modulus.
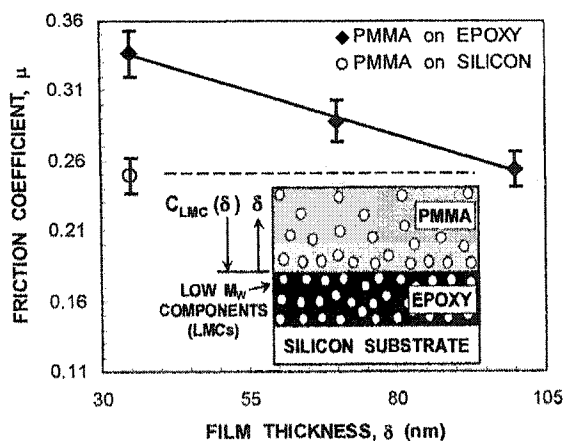
Figure 5.1-1: LFM friction coefficient measurements of PMMA supported on Si and crosslinked epoxy substrates disclose the interfacial plasticization process. (inset) model for low molecular weight component leaching into PMMA.

The friction coefficient for the 35nm films is significantly higher with epoxy substrates than for Si. However, the friction coefficient on thicker epoxy supported films reaches the low value found on the 35nm Si supported film, appearing substrate independent. This friction gradient suggests the leaching of LMCs from the epoxy into the PMMA that is illustrated in Figure 5.1-1, essentially *softens*, or *plasticizes*, the film and reduces the PMMA modulus.

The extent of the softening, and modulus depression, is proportional to the concentration of LMCs, C_{LMC}, at the surface, which in turn, is a function of film thickness. For a thickness of 100nm, the friction coefficient matches that of the 35nm Si supported PMMA, indicating no detectable plasticization, or LMCs, at the surface. This process of heterogeneous interdiffusion across interfaces highlights the importance of substrate chemistry for thin film applications. In this case, a 100nm thick boundary layer is rheologically modified due to the plasticization effects of interdiffused low molecular weight components.

5.2 Dewetting Kinetics

The prior discussion of interfacial plasticization served as one example where chemical transport processes are responsible for the formation of a rheologically modified interfacial boundary. The rheological impact associated with physical and dimensional constraints is perhaps, less intuitive. The role of the substrate in generating rheologically modified boundary layers becomes apparent in dewetting studies with binary PS on polyethylene-co-propylene (PEP) films, which are supported on Si substrates (high interaction surface) [2]. The dewetting kinetics in Figure 5.2-1 were determined from a time-series of SFM topography images, and reveal a critical PEP film thickness, δ_{CRIT}, below which, the dewetting velocity, V_d, decreases with decreasing film thickness, and above which, V_d remains constant. Independent LFM measurements on Si supported PEP films also indicate a critical film thickness, δ_{CRIT}, below which, the friction decreases with decreasing film thickness, and above which remains constant. In both studies, the critical PEP film thickness in Figure 5 corresponds to approximately 100nm.

The dewetting kinetics and friction forces both suggest the presence of a rheologically modified PEP boundary layer adjacent to the Si. For $\delta_{PEP} < \delta_{CRIT}$, the decreasing friction represents an increase in the PEP modulus. This translates to an increasing *glasslike* behavior, or loss of mobility, as the Si interface is approached through the PEP phase. It is this loss of PEP mobility that is responsible for decreasing the dewetting velocity. The dewetting kinetics and friction forces both suggest the presence of a rheologically modified PEP boundary layer

adjacent to the Si. For $\delta_{PEP} < \delta_{CRIT}$, the decreasing friction represents an increase in the PEP modulus. This translates to an increasing *glasslike* behavior, or loss of mobility, as the Si interface is approached through the PEP phase. It is this loss of PEP mobility that is responsible for decreasing the dewetting velocity.
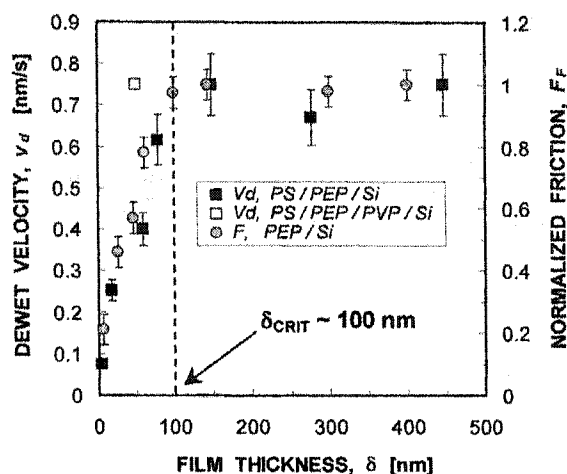
Figure 5.2-1: Dewetting velocity, V_d, and friction, F_F, measurements on PS/PEP systems reveal a 100nm interfacial boundary layer. Data from reference [2].

To identify the source of this rheological gradient, the PEP-Si interactions were effectively masked by first spin casting a low interaction foundation layer of poly(vinyl pyridine) (PVP) on the Si. The dewetting velocity of the PS/PEP/PVP film is reported as the open box in Figure 5 and remained constant, even at PEP film thicknesses below δ_{CRIT}. This anomalous finding unveils the high interfacial interactions between PEP and Si as responsible for the apparent PEP vitrification inside the interfacial boundary.

5.3 Disentanglement Barriers

The current picture of the rheological boundary attributes formation of the boundary layer to interfacial constraints on the molecular mobility. In the past, interfacial effects were considered to be confined to the pinning regime, typically on the order of a few nanometers. However, LFM disentanglement studies on PEP films [8] and NMR tracer diffusion measurements in PS [6] have revealed that the interfacial boundary may extend up to 10 radii of gyration, R_G, beyond the

interface. Simple surface pinning alone has been ruled out since, at this distance, the probability of a polymer molecule making direct surface contact is nearly zero.

LFM friction measurements on Si supported PEP films (R_G = 24nm) offer insight to the source of these *far-field* molecular constraints. A transition in the friction coefficient ($\partial F_F / \partial F_N$) at a critical load, P, is seen in Figure 5.3-1. The higher friction coefficient below P portrays a dissipative behavior consistent with viscous plowing through an entangled PEP melt.
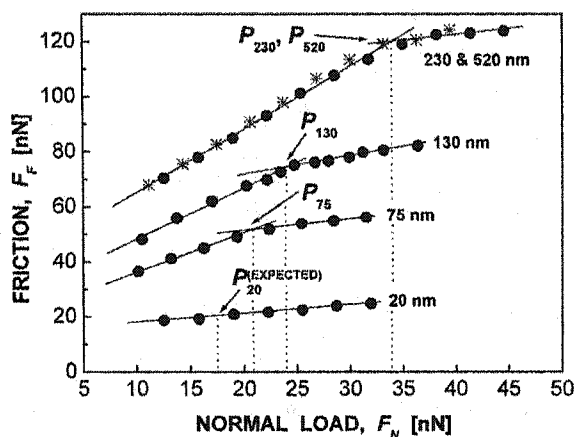
Figure 5.3-1: LFM measurements on PEP films reveal a critical load, P, marking a transition from viscous shearing to chain sliding. Data are from reference [8].

At loads exceeding P, the reduced friction coefficient represents a chain slipping phenomenon similar to a shear banding behavior. Thus, the critical load may be conceptualized as an effective activation barrier for disentanglement [8]. The boundary layer thickness and information about to the conformational structure within the boundary are elucidated from the film thickness dependence of P:

(i) The absence of the disentanglement transition (P) in the 20nm films and the ubiquitous low friction, chain slipping suggest that the PEP molecules are highly disentangled within a *sublayer* immediately adjacent to the substrate.

(ii) In the 75-230nm films, the disentanglement transition (P) increases linearly with film thickness until the bulk-material P is reached. The sub-bulk P values indicate an *intermediate regime* of partial disentanglement, the extent of which diminishes with increasing film thickness until the bulk entanglement density is recovered. This far-field disentanglement (~ 10 R_G from the substrate) is attributed to the strain imposed during spin casting, and the preservation of the

disentangled structure in the melt reflects an anisotropic diffusion process where partially disentangled chain ends diffuse into the porous structure [6] of sublayer [8].

(iii) Finally, for films thicker than 230nm, the polymer behaves like the bulk elastomer and loses any memory of the underlying Si.

The picture of rheological boundary layers now reflects a two phase system comprised of a *sublayer* and an *intermediate regime*. The mobility constraints are ascribed to the strain imposed during spin casting, paired with interfacial interactions in the sublayer and anisotropic diffusion in the intermediate regime.

5.4 Interfacial Glass Transition Profiles

One parameter of particular interest when discussing molecular mobility of polymers is the glass transition temperature, T_g. For thin homopolymer films, it has been recognized that several factors are intricately responsible for the departure of T_g from the bulk value [9-28], e.g. the proximity of a free surface, substrate interactions, and process-induced anisotropy. Here, we address the effects of spin casting on the interfacial T_g profiles of amorphous polymer films. In addition, the use of chemical crosslinking as a controlled mobility constraint in thin films is investigated, and the rheological impact is discussed.

Monodisperse, atactic polystyrene (PS) and polystyrene-vinylbenzocyclobutene (PS-BCB) homo- and co-polymer films were spin cast from cyclohexanone solutions onto silicon wafers <001> and thermally annealed at 134°C under vacuum. The film thicknesses ranged from ~3 - 275 nm. The molecular weights, M_w, were 12.0 kDa for PS; and 17.5 and 21.0 kDa for PS-BCB, with 1.7 and 4.8 mole % BCB, respectively. The BCB served as a latent crosslinking agent, and one possible reaction mechanism is illustrated in Figure 5.4-1. The crosslinking action of BCB is known commercially in adhesion promotion;[29] its incorporation into linear hydrocarbon polymers has been more recent.[30,31] The crosslinks are provided by an o-xylylene unit that is generated *in-situ* from ring opening of the vinylbenzocyclobutene component on application of heat. The reactive diene (o-xylylene) then couples with species on adjacent polymer chains, resulting in a crosslinked matrix. The degree of crosslinking is controlled by the percentage of BCB incorporated during polymerization, and the crosslinking reaction is accomplished by heating the pre-cast films at 250 °C for 1 hour under dry nitrogen.
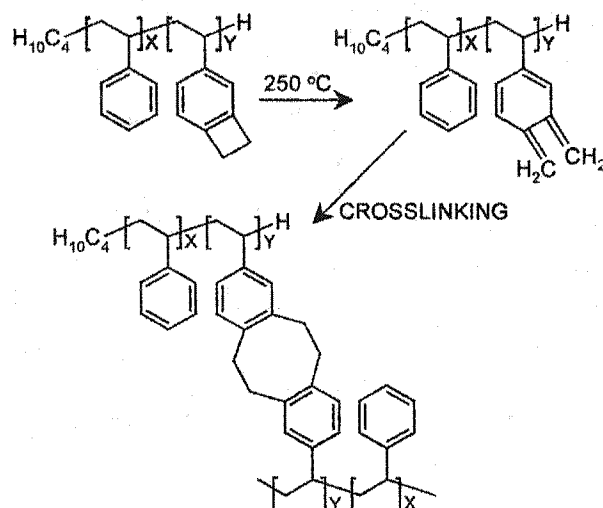
Figure 5.4-1: Polystyrene – vinylbenzocyclobutene crosslinking mechanism.

The quality of the spin cast PS films is illustrated in Figure 5.4-2A, a SFM image which exhibits a smooth topography with a RMS roughness of 0.6 nm. Figure 5.4-2B is representative of the quality of all tested films, with the exception of the thinnest crosslinked films. The onset of partial dewetting was found after crosslinking films thinner than the bulk radius of gyration, R_G, of 4 nm, illustrated in Figure 2(b) for a 4 nm crosslinked 21 kDa PS-BCB film. Thus, we can conclude that the stress imposed on films with a thickness on the order of R_G, or less, is sufficient to thermally activate dewetting instabilities during the crosslinking process at 250 °C.
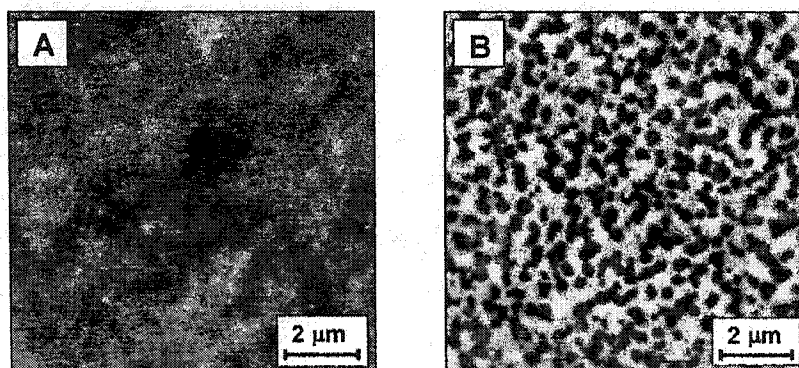
Figure 5.4-2: (a) Representative SFM topography image of a smooth, thin PS film with an RMS roughness of 0.6 nm (dynamic range of grayscale 3.4 nm), measured at 27 °C. (b) Crosslinked PS-BCB film of 4 nm thickness reveals dewetting instability. SFM topography image measured at 27 °C (dynamic range of grayscale = 9 nm).

Near surface glass transition temperatures were acquired using shear-modulated scanning force microscopy (SM-SFM). The measurements were conducted in a dry nitrogen environment with a relative humidity of less than 10 %. For the PS-BCB samples, T_g values were obtained before and after crosslinking. A representative example of the SM-SFM results is reported in Figure 5.4-3 for an uncrosslinked, 140 nm, 17.5 kDa PS-BCB film. The glass transition temperature is indicated by the discontinuity in the slope of the amplitude response, i.e. the onset of creep.
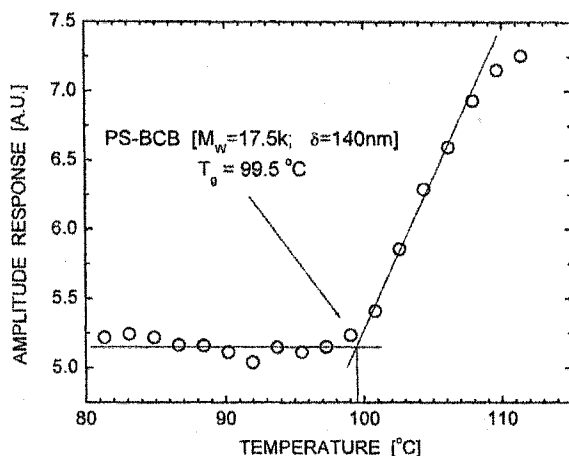
Figure 5.4-3: Near surface T_g measurement in thin PS films using shear-modulated SFM. The amplitude response to the modulation force indicates a T_g value of 99.5 °C on an uncrosslinked, 140 nm thick PS-BCB film (M_w = 17.5 kDa)

In Figure 5.4-4, glass transition values are presented for the homopolymer PS films over a film thickness, δ, range of 5 to 240 nm. For δ > 200 nm, the transition values correspond to the bulk T_g value of 95 °C.[9] However, bulk-deviating values were found for δ < 200 nm. From a qualitative perspective, there are two findings: (a) adjacent to the substrate interface, T_g values are depressed relative to the bulk value within a *sublayer* with a thickness on the order of the unperturbed R_G, which exceeds the persistence length predicted by Brogley[32] by one order of magnitude; and (b) between the sublayer and the bulk phase lies an *intermediate regime* within which T_g values exceed the bulk T_g.

This unexpected, non-monotonic $T_g(\delta)$ relationship can be interpreted considering two competing processes that affect the relaxation dynamics: (a) shear induced structuring and (b) interdiffusion.[6,8,33]
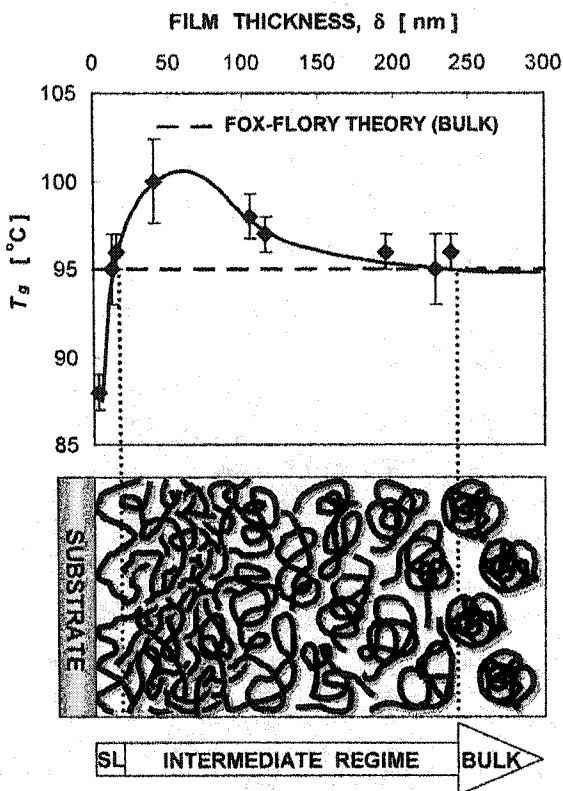
FILM THICKNESS, δ [nm]

Figure 5.4-4: (top) Film thickness dependence of the glass transition temperature on polystyrene films (M_w = 12 kDa) compared to the bulk T_g value predicted from Fox-Flory theory. (bottom) Rheological anisotropy model describing the observed T_g relationship [SL = sublayer].

Shear induced structuring creates an interfacial region where the spin casting shear stresses induce polymer stretching and or disentanglement. This process will hereafter be referred to as polymer deformation. The second process involves the interdiffusion between the entropically cooled interfacial region and the unperturbed bulk phase.

Considering shear induced structuring, computational fluid dynamics (CFD) simulations of Newtonian flow over a rotating disk indicate that the shear stress increases with distance from the interface until a maximum is reached at a distance approximately corresponding to the momentum boundary layer thickness.[34] Further from the interface, the shear stress asymptotically decays to zero at a distance approximately ten times the momentum boundary layer thickness. This shear stress profile is qualitatively similar to the $T_g(\delta)$ profile in Figure 5.4-4, and suggests that the extent of polymer deformation may be related to the shear stresses

experienced during spin casting. Interdiffusion of the deformed chains occurs during annealing, and diffusion generated entanglements are formed. Conformational relaxation during annealing is hindered by the entanglements, which results in residual internal stresses, schematically illustrated as the intermediate regime in Figure 5.4-4. The entanglement density and internal stress profiles follow the shear stress profile during spin casting, with the residual internal stresses presenting an additional barrier to the relaxation associated with the glass transition. Hence, it is surmised that the sequential combination of deformation followed by interdiffusion contributes to the observed $T_g(\delta)$ profile.

Because the spin casting of polymer solutions exhibits a non-Newtonian behavior, direct correlation of the shear stress length scales from the CFD simulations to those of Figure 5.4-4 is not possible. However, experimental studies of polymer solutions under shear flow[35-37] have indicated that shear induced structure formation is a common phenomenon in polystyrene solutions.[36] Given sufficient shear stress and shearing rate, laminar flow induced anisotropic structuring has been observed in polystyrene solutions both with and without entanglements. Furthermore, depending on the solution concentration, the shear induced structuring becomes an irreversible process.[37] With this strong precedence for shear structuring in polystyrene solutions, it is reasonable to propose that the effects of the spin casting process extend from the silicon substrate, over both the sublayer and intermediate regime, to the boundary with the unperturbed bulk phase.

An alternate mechanism responsible for the observed anisotropy proposes the shear structuring effects associated with spin casting extend only through the sublayer, and that interdiffusion alone is responsible for the conformational restructuring within the intermediate regime. The sublayer can be pictured as highly disentangled with a free volume in excess of that of the bulk. This is consistent with neutron reflectivity measurements on PS films that have indicated, for $\delta < R_G$, the film density is less than that of the bulk polymer, and that the density continues to decreases as the film thickness decreases.[33] The mobility of the PS chains is limited by the propagation of *holes*, or packets of free volume, which facilitate conformational rearrangements of the chains.[38] For molecular weights less than the entanglement molecular weight, a moving boundary diffusion process is encountered during annealing, where molecules from the bulk phase diffuse toward the interface into the less dense sublayer, leaving behind holes in which molecules from the adjacent outer *shell* diffuse. The diffusion front propagates from the sublayer a finite distance out into the bulk phase, creating the intermediate regime.

To investigate the effect of the radius of gyration on the $T_g(\delta)$ profile, $T_g(\delta)$ studies have been performed for PS and uncrosslinked PS-BCB samples as a function of molecular weight (12.0, 17.5, and 21 kDa). As seen in Figure 5.4-5, the $T_g(\delta)$ profile for each molecular weight follows the same qualitative behavior as discussed above in Figure 5.4-4. The most significant difference between each molecular weight is the film thickness corresponding to the maxima in the $T_g(\delta)$ profiles. Figure 5.4-5 indicates that, with an increase in molecular weight, the maximum in the $T_g(\delta)$ profile is shifted further from the substrate. The film thickness values at the T_g maxima (δ_{MAX}), interpolated from the three curves in Figure 5.4-5, are plotted together in the inset of Figure 5.4-5. The apparent linear dependence on molecular weight in Figure 5.4-5(inset) yields an approximate δ_{MAX} shift of 10 nm/kDa over the range of molecular weights considered. For all three molecular weights, the bulk T_g values are recovered beyond ~ 250 nm.
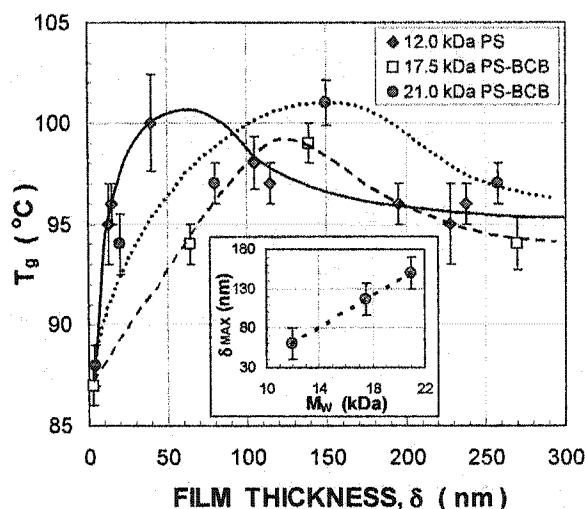
Figure 5.4-5: The effect of molecular weight on $T_g(\delta)$ profiles for polystyrene. (Inset: Film thickness corresponding to maximum T_g, δ_{MAX}, as a function of molecular weight).

In order to probe the effect of modifying the polymer's relaxation behavior on the $T_g(\delta)$ profiles, covalent crosslinks were introduced to the polymer structure (see Figure 5.4-1). Figure 5.4-6 provides $T_g(\delta)$ plots of PS-BCB films (M_w = 21 kDa) before and after crosslinking. The $T_g(\delta)$ profiles exhibit a similar qualitative behavior before and after the reaction, suggesting that the rheological anisotropy, illustrated in Figure 5.4-4, remains even after heating the polymer films ~150 °C above the bulk T_g value, to the crosslinking temperature of 250 °C. However, the

crosslinking yields an overall T_g increase of 7±3 °C. In contrast to the molecular weight dependence of δ_{MAX} shown in Figure 5.4-5, no significant shift is found in the peak values of the $T_g(\delta)$ profiles on crosslinking, which are located at $\delta_{MAX} \approx 150$ nm. The lack of shift in δ_{MAX} on crosslinking is surprising, given the increase in molecular weight that accompanies crosslinking. However, since crosslinking occurs after spin coating, the spin casting dynamics that create the shift in δ_{MAX} are not present. The $T_g(\delta)$ profile is impacted differently for each of the two conditions of higher molecular weight because of the sequential film preparation process.
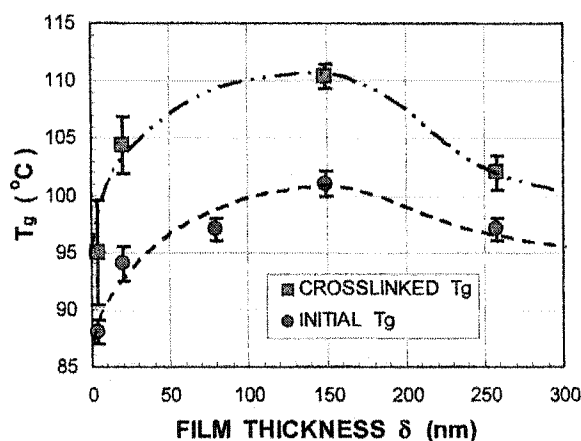
Figure 5.4-6: The effect of crosslinking on the T_g of PS-BCB thin films (21kDa PS - 4.8 mol% BCB, crosslinked at 250 °C under N_2 for 1 hr).

In summary, SM-SFM glass transition measurements of ultrathin spin cast PS films revealed a molecularly restructured and thermally stable boundary layer that extends over 200 nm from the substrate interface, i.e. two orders of magnitude beyond the persistence length. The glass transition temperature, measured as a function of the distance from the substrate, was found to deviate non-monotonically, by as much as ± 10 °C, from the bulk value. The $T_g(\delta)$ profiles exhibited (a) increased molecular mobility in a sublayer adjacent to the substrate $(\delta \sim R_G)$, and (b) reduced molecular mobility in a wide intermediate zone $(R_G < \delta <\sim 200$ nm) between the sublayer and the bulk phase. We attribute the localized increase and decrease in the T_g value to the coupled effects of shear-induced restructuring during spin casting and anisotropic relaxation and transport constraints during annealing.

It was qualitatively and quantitatively illustrated how the $T_g(\delta)$ profiles can be controlled either by adjusting the molecular weight or by crosslinking. On one hand, spin casting films of increased molecular weight had the effect of shifting the $T_g(\delta)$ profiles further from the substrate. The influence of molecular weight on the internal structure of the boundary layer appears more pronounced on the sublayer thickness than on the far-field boundary of the intermediate regime. This suggests that the overall boundary thickness depends more strongly on the spin casting shear stresses than on molecular dimensions. Crosslinking pre-cast films, on the other hand, was found to affect the absolute T_g value without shifting the boundary constraints. Since crosslinking occurs after spin casting, the shear stresses that create the shifted $T_g(\delta)$ profiles are not present, i.e. pre- and post-crosslinked films share the same spin casting history. Hence, the $T_g(\delta)$ profiles are impacted differently for each condition of increased molecular weight because of the sequence of treatments during thin film preparation: molecular weight changes are introduced during solution preparation, prior to spin casting; while crosslinking occurs in a post-spin casting annealing step.

5.5 Chapter Summary

The two phase model for rheological boundary layers has evolved to include interfacial interactions that lead to the formation of a less dense *sublayer* adjacent to the interface. The thickness of the sublayer is characterized, in part, by the molecular dimensions and the interaction potential at the interface. The coupled effects of shear-induced structuring during spin casting and anisotropic relaxation and transport constraints during annealing are responsible for the creation of an *intermediate regime* between the sublayer and bulk phase. The overall rheological boundary may extend up to two orders of magnitude beyond the polymer's persistence length, and the molecular restructuring within the boundary is thermally stable well above T_g. Finally, the impact of mobility constraints (e.g. crosslinking) on the structure within boundary layers depends on the sequence of the film preparation process, i.e. constrains incorporated before and after casting exhibit different rheological outcomes.

With this knowledge, very specific material engineering involving spin cast polymer films can be achieved through an understanding of polymer dynamics at the polymer-substrate interface. Modified relaxational properties and enhanced conformational stability may be achieved through control of the molecular weight, crosslinking density, and film thickness. In this regard, the measurement and control of interfacial glass transition profiles becomes

60

increasingly important, as nanotechnological thin film applications, such as terabit thermomechanical data storage,[39] rely on very specific relaxation, transition, and transport properties within the sub-one-hundred nanometer regime.

5.6 Notes to Chapter 5

[1] B. Frank, A. P. Gast, T. P. Russel, H. R. Brown and C. Hawker, *Macromolecules* **29**, 6531 (1996).

[2] R. M. Overney, L. Guo, H. Totsuka, M. Rafailovich, J. Sokolov and S. A. Schwarz, in *Dynamics in Small Confining Systems IV*, Vol. 464, edited by J. M. Drake, J. Klafter, and R. Kopelman (Material Research Society, Pittsburgh, PA, 1997), pp. 133.

[3] M. Rabeony, D. G. Pfeiffer, S. K. Behal, M. Disko, W. D. Dozier, P. Thiyagarajan and M. Y. Lin, *J. Chem. Soc., Faraday Trans.* **91**, 2855 (1995).

[4] P. F. Green, T. M. Christensen, T. P. Russel and J. J. Jérôme, *J. Chem. Phys.* **92**, 1478 (1990).

[5] T. P. Russel, A. Menelle, S. H. Anastasiadis, S. K. Satija and C. F. Majkrzak, *Macromolecules* **24**, 6263 (1991).

[6] X. Zheng, M. H. Rafailovich, J. Sokolov, Y. Strzhemechny, S. A. Schwarz, B. B. Sauer and M. Rubinstein, *Phys. Rev. Lett.* **79**, 241 (1997).

[7] R. M. Overney, D. P. Leta, L. J. Fetters, Y. Liu, M. H. Rafailovich and J. Sokolov, *J. Vac. Sci. Technol.* **B 14**, 1276 (1996).

[8] C. Buenviaje, S. Ge, M. Rafailovich, J. Sokolov, J. M. Drake and R. M. Overney, *Langmuir* **15**, 6446 (1999).

[9] C. Buenviaje, F. Dinelli and R. M. Overney, in *ACS Symposium Series "Interfacital Properties on the Submicron Scale"*, Vol. **781**, edited by J. Frommer and R. M. Overney (Oxford U. P., New Orleans, 2000), pp. 76.

[10] H. P. Chen, D. Katsis, J. C. Mastrangelo, S. H. Chem, S. D. Jacobs and P. J. Hood, *Adv. Mater.* **12**, 1283 (2000).

[11] P. Claudy, J. M. Letoffe, Y. Camberlain and J. P. Pascault, *Polym. Bull.* **9**, 208 (1983).

[12] K. Dalnoki-Veress, J. A. Forrest, P. G. d. Gennes and J. R. Dutcher, *J. Phys. IV* **10**, 221 (2000).

[13] P.-G. de Gennes, *C.R. Acad. Sci.* **IV**, 1 (2000).

[14] G. B. DeMaggio, W. E. Frieze, D. W. Gidley, M. Zhu, H. A. Hristov and A. F. Yee, *Phys. Rev. Lett.* **78**, 1524 (1997).

[15] E. A. DiMarzio and A. J. M. Yang, *J. Res. Natl. Inst. Stand. Technol.* **102**, 135 (1997).

[16] F. Dinelli, C. Buenviaje and R. M. Overney, *J. Chem. Phys.* **113**, 2043 (2000).

[17] A. Eisenberg, in *ACS Symposium Series "Physical Properties of Polymers"*, 2nd ed., edited by J. E. Mark (ACS, Washington DC, 1993).

[18] J. A. Forrest, K. Dalnoki-Veress, J. R. Stevens and J. R. Dutcher, *Phys. Rev. E* **56**, 5705 (1997).

[19] J. A. Forrest and J. Mattsson, *Phys. Rev. E* **61**, R53 (2000).

62

[20] S. Ge, Y. Pu, W. Zhang, M. Rafailovich, J. Sokolov, C. Buenviaje, R. Buckmaster and R. M. Overney, *Phys. Rev. Lett.* **85**, 2340 (2000).

[21] T. Kajiyama, K. Tanaka and A. Takahara, *Macromolecules* **28**, 3482 (1995).

[22] J. L. Keddie, R. A. L. Jones and R. A. Cory, *Europhys. Lett.* **27**, 59 (1994).

[23] Y. Liu, T. P. Russell, M. G. Samant, J. Stohr, H. R. Brown, A. Cossy-Favre and J. Diaz, *Macromolecules* **30**, 7768 (1997).

[24] G. F. Meyers, B. M. DeKoven and J. T. Seitz, *Langmuir* **8**, 2330 (1992).

[25] R. M. Overney, C. Buenviaje, R. Luginbuehl and F. Dinelli, *J. Therm. Anal. Cal.* **59**, 205 (2000).

[26] D. Schaefer, H. W. Spiess, U. W. Suter and W. W. Fleming, *Macromolecules* **23**, 3431 (1990).

[27] K. C. Tseng, N. J. Turro and C. J. Durning, *Phys. Rev. E* **61**, 1800 (2000).

[28] J. H. Kim, J. Jang and W. C. Zin, *Langmuir* **17**, 2703 (2001).

[29] D. Scheck, (Dow Chemical Company, Hsinchu, Taiwan, 2001).

[30] W. Chau, V. Lee, J. Frommer, S. Sills and R.Overney, in *CPIMA Forum 2001* (Center for Polymer Interfaces and Macromolecule Assemblies, Stanford, CA, 2001).

[31] L. Y. T. Li, H. C. Kim and C. J. Hawker, (Center for Polymer Interfaces and Macromolecule Assemblies, Stanford, CA, 2001).

[32] M. Brogly, S. Bistac and J. Schultz, *Macromol. Theory Simul.* **7**, 65 (1998).

[33] W. J. Orts, J. H. Van Zanten, W. L. Wu and S. K. Satija, *Phys. Rev. Lett.* **71**, 867 (1993).

[34] X. Wu and K. D. Squires, *J. Fluid Mech.* **418**, 231 (2000).

[35] S. Saito and T. Hashimoto, *J. Chem. Phys.* **114**, 10531 (2001).

[36] M. K. Endoh, S. Saito and T. Hashimoto, *Macromolecules* **35**, 7692 (2002).

[37] I. Morfin, P. Linder and F. Boue, *Macromolecules* **32**, 7208 (1999).

[38] C. L. Wang and S. J. Wang, *Phys. Rev. B* **51**, 8810 (1995).

[39] P. Vettiger, G. Cross, M. Despont, U. Drechsler, U. Duerig, W. Heberle, M. I. Lantz, H. E. Rothuizen, R. Stutz and G. K. Binnig, *IEEE Trans. Nanotechnol.* **1**, 39 (2002).

6. Strain Shielding and Confined Plasticity in Thin Polymer Films

6.0 Overview

In the previous chapter, the contribution of interfacial constraints to the formation of rheological boundary layers was explored for thin polymer films. A variety of rheological manifestations were illustrated, and a visualization of the molecular configuration within interfacial boundaries was developed. At this point, it is pertinent to discuss the implications of interfacial constraints and rheological boundaries in technological applications. Particularly relevent is the process of ultrahigh density thermomechanical data storage in thin polymer films[1,2] (see Chapter 1).

Ultrahigh density thermomechanical data storage (TDS) relies on writing, reading, and erasing nanometer sized data bits in thin polymer films.[1,2] In essence, the TDS writing operation is a high speed (MHz), elastic-viscoplastic polymer indentation process. The polymer storage media must be designed to achieve the narrow range of physiochemical properties necessary for: high data density, fast data rates, high durability, long shelf life, and low power consumption. The ideal polymer should be easily deformable for bit writing; however, the written bits must be stable against dewetting, thermal degradation, and wear.

Each indented bit represents a metastable state of the deformed volume, and will either initiate spontaneous dewetting (film instability) or strive for recovery of the initial unstressed state (bit instability).[3] The delicate balance between these instability nodes constitutes one optimization scenario in the design of polymeric storage media. Furthermore, media (and data) wear must be minimized during scanning operations. In particular, topographical protrusions, in the form of piled-up *rims* around the indented bits, are regions susceptible to wear. The presence of rims also adversely affects the writing density. Rims interact non-linearly with adjacent bits, lowering the signal-to-noise ratio of bit detection and requiring a relaxation of the indentation pitch (data density). From the perspectives of media wear and data density, a suitable polymer storage media exhibits a weak propensity for rim formation during indentation.

In this chapter, we review the contact mechanics associated with the indentation process, then we explore how the contact mechanics associated with TDS in polymer films may be compounded by the proximity of the underlying substrate. Specifically, in section 6.4, we investigate interfacial strain shielding and its implications on rim formation during high strain rate indentations in thin polystyrene films. We revisit the scaling basis of the well known "10%

rule" for ascertaining substrate constraints under impact conditions. Finally, we illustrate the role of rheological anisotropy in the indentation process, and elucidated the polymer's mechanical response with interfacial glass transition profiles.

6.1 Indentation Contact Mechanics

During normal indentation of an elastic-plastic material, when the yield point of the more ductile material is first exceeded, the onset of plastic deformation commences. Initially, the plastic region is small and completely contained by the surrounding elastic material. Hence, the plastic strains are of the same order of magnitude as the surrounding elastic strains. The plastically displaced material is fully accommodated by elastic expansion of the surrounding solid. This is referred to as the "constrained deformation" regime because the flowing or plastically deforming volume is fully constrained by the surrounding elastic medium. As the applied strain is increased, i.e. increased load or sharper indenter, a greater pressure beneath the tip is required to produce the necessary expansion. Eventually, sufficient pressure is achieved where the plastic region reaches the free surface, allowing the displaced material to escape via "uncontained" plastic flow along the sides of the indenter.

The onset of plastic yield, or constrained deformation, is assessed by applying an appropriate yield criterion. The two most commonly applied criteria are the Tresca's maximum shear stress criterion, where yielding occurs when the maximum shear stress, or half the difference between the maximum and minimum principle stresses, reaches the yield stress in pure shear or half the yield stress in simple compression (or tension):[4]

$$\max\left[\frac{1}{2}|\sigma_1 - \sigma_2|, \ \frac{1}{2}|\sigma_2 - \sigma_3|, \ \frac{1}{2}|\sigma_3 - \sigma_1| \right] = k = \frac{Y}{2} , \qquad (6.1\text{-}1)$$

and the von Mises' shear strain-energy criterion, where yielding occurs once the deformation energy equals the deformation energy at yield in simple compression or pure shear.[5] Therefore, by the von Mises criterion, yielding occurs when the square root of the second invariant, J_2, of the stress deviator tensor, S_{ij}, reaches the yield stress in simple shear or $1/\sqrt{3}$ of the yield stress in simple compression:

$$\sqrt{J_2} = \left[\frac{1}{2}S_{ij}\right]^{1/2} = \left\{\frac{1}{6}\left[(\sigma_1 - \sigma_2)^2 + (\sigma_2 - \sigma_3)^2 + (\sigma_3 - \sigma_1)^2\right]\right\}^{1/2} = k = \frac{Y}{\sqrt{3}} \qquad (6.1\text{-}2)$$

where σ_1, σ_2, and σ_3 are the principle stresses in the state of complex stress, and k and Y represent the yield stresses in pure shear and simple compression (or tension), respectively. For detailed analysis of the state of complex stress and formulation of the yield criteria, the reader is referred to [6].

Experiments on isotropic metals support the von Mises criterion over Tresca's; however, the discrepancy between the two is relatively small considering the variability in k or Y and the inherent anisotropies in most materials. Therefore, it is generally acceptable to apply Tresca's criterion for its mathematical simplicity.

Relating the stresses from the yield criteria to the mean contact pressure under the indenter,

$$p_m = cY \qquad (6.1\text{-}3)$$

where, for the onset of constrained plastic yield, c has a value of about 0.5 for conical indenters, and may vary depending on the indenter geometry and the friction at the interface.[4]

The onset of unconstrained plastic flow, i.e. the point when the plastic yield zone reaches the free surface, is expected to occur when the contact pressure reaches the yield stress given by rigid-plastic theory. Based on a number of numerical analyses and indentation measurements with rigid spheres and cones in elastic-plastic half-spaces, Johnson has determined a value of $c \sim$ 2.8, in equation 6.1-3.

In the transitional regime, when the contact pressure lies between $0.5\sim3Y$, plastic flow is contained by the surrounding elastic material. The resulting deformation is generally in the form of radial expansion with roughly hemispherical contours of equal strain.[4] Based on these observations, Johnson (1970)[7] has developed a simple cavity model of elastic-plastic indentation, Figure 6.1-1. The cavity model assumes that directly beneath the indenter contact surface, a hemispherical core with a radius equal to that of the projected contact area, a, has a hydrostatic stress component equal to the mean contact pressure, p_m. Immediately beyond the core lies the plastic zone, and at the core-plastic boundary, the radial stress component in the plastic zone equals the hydrostatic stress of the core.
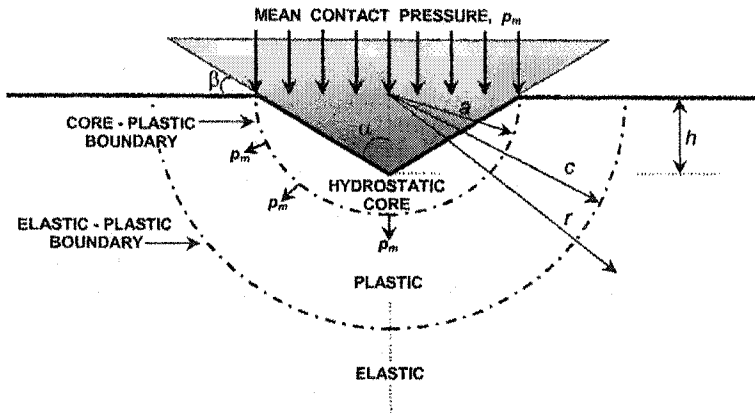
Figure 6.1-1: Cavity model elastic-perfectly plastic indentation by a cone .

Within the plastic zone, stresses and displacements have radial symmetry, and the plastic strains gradually dimish with increasing radial distance, until they match the elastic strains at the elastic-plastic boundary, c $(c > a)$.

Based on Hill,[6] the stresses in the plastic zone, $a \leq r \leq c$, are characterized by:

$$\frac{\sigma_r}{Y} = -2\ln\left(\frac{c}{r}\right) - \frac{2}{3} \ , \qquad \frac{\sigma_\theta}{Y} = -2\ln\left(\frac{c}{r}\right) + \frac{1}{3} \qquad \text{(6.1-4a,b)}$$

and in the elastic zone, where $r \geq c$

$$\frac{\sigma_r}{Y} = -\frac{2}{3}\left(\frac{c}{r}\right)^3 , \qquad \frac{\sigma_\theta}{Y} = \frac{1}{3}\left(\frac{c}{r}\right)^3 \qquad \text{(6.1-5a,b)}$$

At the core-plastic boundary, the core pressure is given by:

$$\frac{p_m}{Y} = \left(-\frac{\sigma_r}{a}\right)\bigg|_{r=a} = 2\ln\left(\frac{c}{a}\right) + \frac{2}{3} \qquad \text{(6.1-6)}$$

Equation 6.1-6 implies that the elastic-plastic boundary coincides with the core-plastic boundary, $c = a$, at $p_m = \frac{2}{3}Y$, and at reduced pressures, no plastic flow occurs. Therefore, the cavity

model predicts that the onset of plastic yield occurs at $p_m = {}^2/_3 Y$ which is close to the value of $c \sim 0.5$ reported by Johnson (1970).[7] The difference is attributed to β, and friction at the interface.

Radial displacement of matter at the core-plastic boundary, $r=a$, during an increment of penetration, dh, must accommodate the volume of material displaced by the indenter. Neglecting core compressibility, conservation of core volume requires:

$$2\pi a^2 du(a) = \pi a^2 dh = \pi a^2 \tan(\beta) da \tag{6.1-7}$$

The radial displacements within the plastic zone are given by:[6]

$$\frac{du(r)}{dc} = \frac{Y}{E}\left[3(1-v)\left(\frac{c}{r}\right)^2 - 2(1-2v)\left(\frac{r}{c}\right)\right] \tag{6.1-8}$$

Equations 6.1-7 and 6.1-8 are used to locate the elastic-plastic boundary, c, recognizing that for a conical indenter, geometrical similarity of the strain field with continued penetration requires $dc/_{da} = {}^c/_a = constant$:

$$\left(\frac{c}{a}\right)^3 = \frac{1}{6(1-v)}\left[\frac{E\tan\beta}{Y} + 4(1-2v)\right] \tag{6.1-9}$$

The core pressure is determined via substituting ${}^c/_a$ into equation 6.1-6, and for an incompressible material, i.e. $v=0.5$:

$$\frac{p_m}{Y} = \frac{2}{3}\left[1 + \ln\left(\frac{1}{3}\frac{E\tan\beta}{Y}\right)\right] \tag{6.1-10}$$

The hydrostatic core pressure appears solely dependent on the parameter $(E/Y)\tan\beta$, which represents the ratio of the strain imposed by the indenter $(\tan\beta)$ to the strain capacity of the indented material (Y/E). The indentation pressure under elastic, elastic-plastic, and fully plastic conditions is generally correlated as dimensionless contact pressure, P_m/Y, versus dimensionless strain, $(E/Y)\tan\beta$,

The above analysis was limited to elastic-perfectly plastic materials with a constant yield stress; however, Tabor has shown that the analysis for a perfectly plastic solid may be applied,

with good approximation, to work (or strain) hardening materials if Y is replaced by a "representative" flow stress Y_R, measured in simple compression at a representative strain ε_R, where for a material whose strain hardening is described by a power law relation:[8]

$$Y_R = \sigma_o \left(\frac{\varepsilon_R}{\varepsilon_o} \right)^{\frac{1}{n}}$$ (6.1-11)

where n is the reciprocal of the work hardening index, and σ_o is the work hardening coefficient. Substituting into equation 6.1-3 and using a value of c corresponding to perfect plastic yielding, i.e. 3:

$$\varepsilon_R = \varepsilon_o \left(\frac{p_m}{3\sigma_o} \right)^n$$ (6.1-12)

Equation 6.1-12 enables ε_R to be determined given the appropriate expression for p_m, and for a conical indenter, is approximated by:[4]

$$\varepsilon_R \approx 0.2 \tan \beta$$ (6.1-13)

The scenario is somewhat more complicated for the case of viscoelastic plastic indentation. As discussed in Chapter 1, many materials, notably polymers, exhibit viscoelastic behavior, which is characterized by a time and temperature dependent stress-strain relationship. In the context of non-conforming contacts, such as indentations, the issue becomes one of determining the variation with time of the contact area and pressure distribution resulting from a prescribed loading or penetration schedule. In cases where the corresponding solution for a purely elastic material is known, the simplest approach to this problem, based on Radok, consists of replacing the elastic constant in the elastic solution with the corresponding integral operator from the viscoelastic stress-strain relations, i.e. the creep compliance or relaxation functions.[4]

6.2 Thermoelastic Contact Mechanics

The analysis of this thermoelastic contact problem consists of three parts: (i) heat transfer analysis to determine the temperature distribution within the two contacting bodies; (ii) analysis of the thermal expansion of the bodies to determine the thermal distortion of the contact area; and (iii) analysis of the isothermal contact problem to assess the contact stresses resulting from the deformed profile. With a conical indenter, a symmetrical body of revolution, we will only be concerned with the two dimensional case (z and r in cylindrical coordinates). Assuming that the indenter reaches its final hot temperature before the polymer reaches T_g (when significant penetration begins), the problem may formulated as follows: a hot body at an initial uniform temperature T_H is pressed into contact with a colder body at initial uniform temperature T_C, and the interfacial temperature, T_i, is uniform throughout the contact region. The contact area is circular with radius a. Initially, we will assume a frictionless interface. The distribution of heat flux, $\dot{q}$, across the interface is given by:[4]

$$\dot{q}(r) = \frac{2k_H(T_H - T_i)}{\pi(a^2 - r^2)^{1/2}} = \frac{2k_C(T_i - T_C)}{\pi(a^2 - r^2)^{1/2}} \tag{6.2-1}$$

where k_i is the thermal conductivity of the respective body. Integrating over the contact area gives the total heat flux, $\dot{Q}$:

$$\dot{Q} = 4k_H a(T_H - T_i) = 4k_C a(T_i - T_C) = 4\bar{k}a(T_H - T_C) \tag{6.2-2}$$

where $\bar{k} = k_H k_C / (k_H + k_C)$. The surface profile resulting from the thermoelastic distortion is then determined by:

$$\bar{u}_z(r) = -\frac{2}{\pi}c\bar{k}a\left(T_H - T_C\right)\left\{\ln\left(\frac{r_o}{a}\right) - \ln\left[1 + \left(1 - \frac{r^2}{a^2}\right)^{\frac{1}{2}}\right] + \left(1 - \frac{r^2}{a^2}\right)^{\frac{1}{2}}\right\}; \quad r \le a \tag{6.2-3a}$$

$$\bar{u}_z(r) = -\frac{2}{\pi}c\bar{k}a\left(T_c - T_o\right)\ln\left(\frac{r_o}{r}\right); \quad r > a \tag{6.2-3b}$$

where $c = (1 + v)\alpha/k$ is refered to as the *distortivity* of the material, v is the Poisson ratio, α is the coefficient of thermal expansion, and r_o is the position on the surface where $\bar{u}_z = 0$. The distorted surface profile affects the contact area and thus the contact pressure. The thermally induced pressure component may be expressed as:

$$p_t(r) = (c_2 - c_1)\frac{\dot{Q}E^*}{2\pi^2 a}\left\{\frac{\pi^2}{8} - X_2\left[\frac{a - \left(a^2 - r^2\right)^{\frac{1}{2}}}{a + \left(a^2 - r^2\right)^{\frac{1}{2}}}\right]\right\}$$

(6.2-4)

where E^* is the reduced modulus and X_2 is Legendre's Chi function, i.e.

$$X_2(x) = \frac{1}{2}\int_0^x \ln\left(\frac{1+s}{1-s}\right)\frac{ds}{s} = \sum_{m-1}^{\infty}\frac{x^{2m-1}}{(2m-1)^2}$$

(6.2-5)

The thermal component to the mean contact pressure is given by:

$$P_t = \frac{1}{2\pi}(c_2 - c_1)\dot{Q}E^*a = \frac{2}{\pi}\bar{k}(T_H - T_C)E^*a^2$$

(6.2-6)

The net pressure, corresponding to the total load, is found by adding the thermal component to the isothermal contact pressure. For a Hertzian contact pressure it is:

$$P = P_t + P_{iso} = P_t + \frac{4E^*a^3}{3R}.$$

(6.2-7)

The total load, P, provides the following relationship:

$$\beta\left(\frac{a}{a_o}\right)^2 + \left(\frac{a}{a_o}\right)^3 = 1$$

(6.2-8a)

with

$$\beta = \frac{3kR}{2\pi a_o}(c_2 - c_1)(T_1 - T_2)$$

(6.2-8b)

and $a_o = (3RP/4E^*)^{1/3}$ assuming an isothermal Hertzian contact. From equation 6.2-8a, it may be inferred for $\beta > 0$, that an increase in the differential distortivity or temperature difference causes the relative curvature of the two surfaces to increase and the contact area, a, to decrease.[4]

6.3 Rim Formation During Indentation

During indentation of a rigid plastic solid, the displaced material appears in the piled-up rim around the periphery of the indentation site; but with elastic-plastic materials, most, if not all, of the displaced material is accommodated by radial expansion of the elastic surroundings, with an imperceptible change in the surface dimensions of the indented material.

Briscoe et al. have found for indentation and scratch hardnesses studies of PMMA, the measured yield stress is strongly dependent on both the indenter geometry (related to strain) and applied strain rate. During normal indentation with conical indentors of large excluded angles ($\beta=75°$), PMMA deforms by extrusion to the free surface with the creation of a piled-up rim. With blunter cones, i.e. lower β, deformation occurred elastoplasticly resulting in little or no pile-up.[9] In nano-scratch studies on PMMA, Adams et al. have demonstrated that the height of the pile-up will increase with $\tan\beta$.[10] In a similar study on polycarbonate, Jardret et al. have observed distinctly different pile-up formations during nano-scratching on samples of identical hardness. The difference in pile-up height was attributed to the strain magnitude, with an increased rim height for larger strains, i.e larger $\tan\beta$.[11] With a 2D finite element approach, Ramond-Angélélis has modeled piled-up rim formation in viscoelastic-perfectly plastic materials as a function of the rheological factor X, defined as ratio between the strain imposed by the indenter ($\varepsilon \sim \tan\beta$) and the strain capacity of the material ($\varepsilon \sim Y/E$), i.e. $X = E/Y \tan\beta$. These results are presented in Figure 6.3-1, and suggest for values of $X < \sim 10$, the deformation during indentation is mainly elastic with little pile-up, and for $X > \sim 100$, the deformation is primarily plastic resulting in substantial pile-up.[12]

Pile-up formation in viscoelastic materials is also dependent on the strain rate. At high strain rates, PMMA displays a noticeable strain softening behavior that becomes more pronounced with increasingly higher strain rates and is absent at reduced strain rates ($< \sim 10^{-5}$/s).[9] Consequently, the yield stress decreases with increased strain rate, and is accompanied by the appearance of shear bands, which has been attributed to the onset of pile-up.[13,14] The effect of a high strain rate at large strains, i.e. high $\tan\beta$, may also induce adiabatic heating within the shear

bands, which would promote large inhomogeneous strains, as well as, enhanced strain softening.[9]

Figure 6.3-1: Cross-sectional view of elasto-plastic indentation under load and after unloading for a rheological factor, X, ranging from 1-1000. Results obtained by Ramond-Angélélis with a 2-D finite element model.[12]

Pile-up is also influenced by the strain hardening behavior of the material. A large capacity for strain hardening advances the plastic zone further into the material, thus decreasing pile-up adjacent to the indenter.[15] For an elastic-plastic material which strain hardens according the following power law:

$$Y_R = \sigma_o \left(\frac{\varepsilon_R}{\varepsilon_o} \right)^{\frac{1}{n}} \qquad (6.3\text{-}1)$$

where n is the reciprocal of the work hardening index, and σ_o is the work hardening coefficient, Matthews has proposed the indenter penetration depth, h, follows:[15]

$$\frac{\xi}{h} = \frac{1}{2} \left(\frac{2n+1}{2n} \right)^{2(n-1)} - 1 \qquad (6.3\text{-}2)$$

where ξ represents the vertical dimension with respect to the neutral surface of a piled-up rim or sunken depression at the periphery of the indentation, Figure 6.3-2.
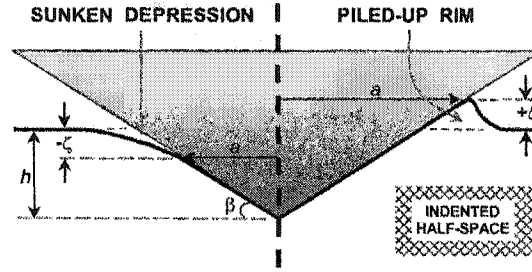
Figure 6.3-2: Peripheral deformation for opposing extremes of stress sensitivity. Sunken depression observed on materials that exhibit strong strain hardening, and piled-up rims are observed on materials that exhibit slight strain hardening.

For a conical indenter:

$$h + \xi \cong a \tan \beta \qquad (6.3\text{-}3)$$

Combined with equation 6.3-2, the indentation depth becomes:

$$h = 2\left(\frac{2n}{2n+1}\right)^{2(n-1)} a \tan \beta \qquad (6.3\text{-}4)$$

For $h/(a\tan\beta)>1$ (i.e. $n<3.8$), a sunken depression is formed, and when n exceeds 3.8, $h/(a\tan\beta)<1$ and a piled-up rim is formed.

In viscoelastic materials, such as polymers, strain hardening must also be addressed. The pile-up formed during the nano-scratch studies on PMMA was analyzed by Adams et al. Indentation hardness measurements of the piled-up rim revealed a maximum hardness value at the rim apex, which decayed asymptotically to the hardness of the unperturbed film with increasing distance from the indentation site. Both the rim height and the extent of strain hardening within the pile-up were increased with the applied strain, i.e. $\tan\beta$.[10] In addition, Adams et al. observed that the hardened pile-up of an existing scratch reduces the depth of a subsequent parallel scratch within the strain hardened area. This is important in the context of thermomechanical data storage where ultra high storage densities are sought by minimizing the pitch of indented data-bits. A tight indentation pitch with overlapping strain hardened zones would likely result in non-uniform indentation depths, sacrificing device reliability.

6.4 Interfacial Constraints in Nano-Contact Mechanics

The above discussion has been limited to bulk materials, and the formation of piled-up rims has been attributed primarily to the applied strain and strain rate, and strain capacity and strain hardening susceptibility of the material. In confined systems, for example substrate supported polymer thin films, it may be expected that the presence of the underlying substrate affects the stress-strain behavior of the polymer film. A rigid boundary interacting with the stress field during indentation (bit writing) is capable of altering the imposed stress and strain distributions, leading to bulk-deviating mechanical responses.[16-19] For indentations in compliant films, increased rim heights are observed when elastic strain and plastic flow are constrained, or shielded, by a rigid substrate[16-19] In the case of rigid films on compliant substrates, the plastic yield of the underlying substrate accommodates an enhanced *sink-in* of the surface around the periphery of indentation sites.[17]

To investigate the effect of film thickness, i.e. proximity of a rigid substrate, on the indentation response of thin polymer films, polystyrene films (PS) ($M_W = 12k$), 16 to 163 nm thick, were spin cast from cyclohexanone solutions onto silicon wafers (<100>, N-doped, resistivity = 0.1 Ω/cm). To provide a means of decoupling substrate effects from film thickness effects, one sample (45 nm PS) was prepared with a 230 nm buffer layer of crosslinked polystyrene-vinylbenzocyclobutene (PS-BCB) between the silicon substrate and the PS film. All films were annealed between 160 and 175°C under argon for 30 minutes. The thin films were indented using heated tip scanning force microscopy (HT-SFM) with a cantilevered probe setup identical to the ones used for TDS, Figure 6.4-1.
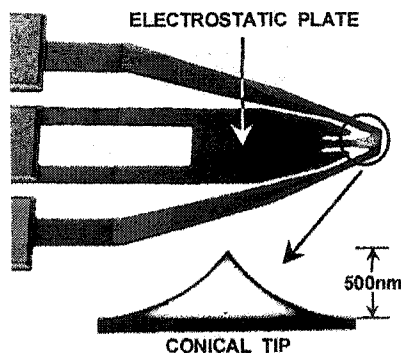

Figure 6.4-1: Scanning electron microscopy (SEM) images of the cantilever used in this study, a typical design for ultrahigh density thermomechanical recording. Loading is controlled by the electrostatic field between the cantilever plate and the sample.

The indenting probe was operated with a modified commercial scanning force microscope (SFM) (DI Dimension 5000, Veeco). For this study, the indentations were created at room temperature. The normal indentation load, F_N, was provided through an electrostatic force generated with a bias between the substrate and the electrostatic plate on the lever. The magnitude of F_N is proportional to the square of the lever-sample voltage bias, ΔV, i.e. $F_N(\Delta V) = \alpha |\Delta V|^2$, where α is a calibration constant. The lever is calibrated through a series of force-displacement (FD) curves conducted over a range of lever-sample biases. For each FD curve, the electrostatic force is determined from $F_N(\Delta V) = C_N * \Delta z(\Delta V)$, where C_N is the normal spring constant of the lever (~0.1 N/m) and $\Delta z(\Delta V)$ is the additional z-piezo displacement required to reach the snap-out instability for a given bias, pictured in the inset of Figure 6.4-2.

The indentation loads were provided in the form of 10 μs pulses. A short pulse-time was chosen in accordance with operating rates used for thermomechanical writing.[2] For each film thickness, arrays of 10×10 indentations were generated at loads ranging from 50 to 250 nN. The uncertainty associated with the absolute force values is approximately ± 20%, but the relative uncertainty between force measurements is within 9%.
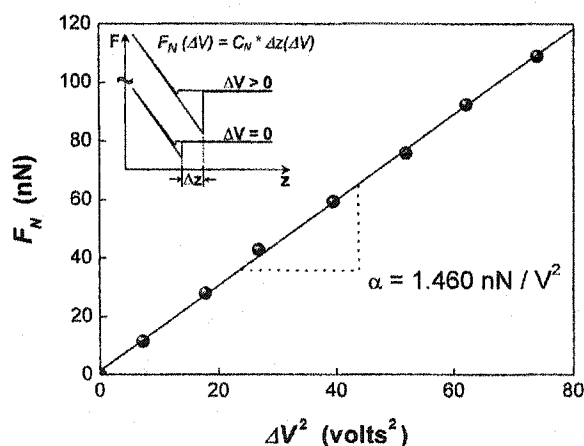
Figure 6.4-2: Electrostatic force calibration of the cantilever probe. (inset) The electrostatic force, F_N for a given bias, ΔV, is determined from the additional displacement, Δz, necessary to reach the snap-out instability during a force-displacement curve.

Topography images of the residual indentation impressions were acquired using the same probe with the optical detection scheme of the SFM system. Figure 6.4-3 illustrates such an indentation array for a 45 nm PS film on a 230 nm PS-BCB buffer film.
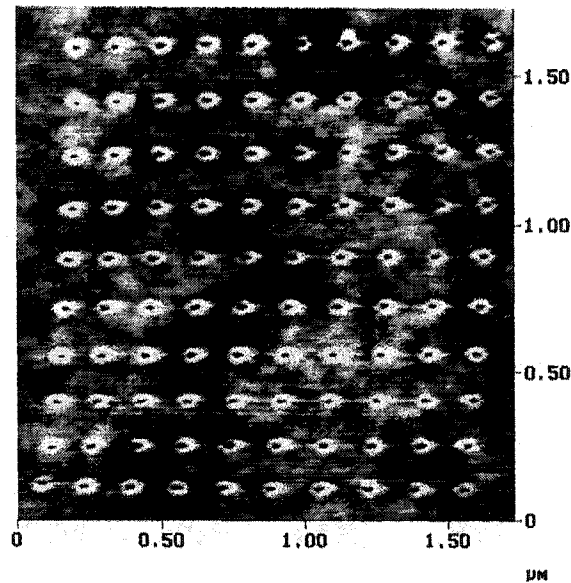
Figure 6.4-3: SFM image of a 10 × 10 indentation array in a 45 nm PS film on a 230nm crosslinked PS-BCB substrate (grayscale range = 15 nm).

Figure 6.4-4 illustrates the parameters deduced from each indentation, which are categorized into vertical parameters (indent depth, d, rim height, z) and horizontal parameters (indent diameter, D_i, rim diameter, D_R). The slight eliptical shape of the indentations, apparent in Figure 6.4-4, results from an approximate 4° relative cantilever-sample declination necessary to avoid optical interference on the photodiode. Because of this asymmetry, the geometric features for each indentation were measured at the four cardinal points and averaged. Individual datum points in subsequent figures represent a collective average of 20 separate indentations.

The indentation parameters in a silicon supported 69 nm film are correlated to the applied load in Figure 6.4-5, which is qualitatively representative of each film thickness and substrate configuration. Considering all sample thicknesses and indentation loads, the residual indentation depth ranged from 0.4 to 3.5 nm, with the rim height always some fraction of the depth. The residual indent diameter ranged from 15 to 50 nm; while the rim diameter ranged from 70 to 160 nm. With an indenter aspect ratio close to one, the discrepancy in the magnitude between the vertical and lateral parameters suggest a significant elastic recovery on unloading. However, in the discussion below, we will argue that it is the high strain rate, not elastic recovery, that is responsible for the dimensional mismatch.
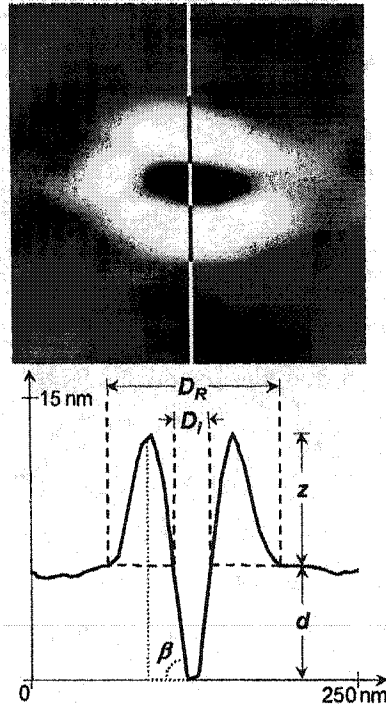
Figure 6.4-4: Geometric evaluation of a residual indentation (45 nm PS film on a 230nm crosslinked PS-BCB buffer layer). *Vertical indentation parameters*: Rim height, z, and the indentation depth, d. *Lateral indentation parameters:* Rim diameter, D_R, and the indentation diameter, D_i.

Figure 6.4-5: The load dependence of the vertical and lateral indentation parameters of residual indentations in a silicon supported, 69 nm PS film.

The extent of elastic versus plastic deformation can be estimated by considering the ratio of the strain imposed by the indenter to the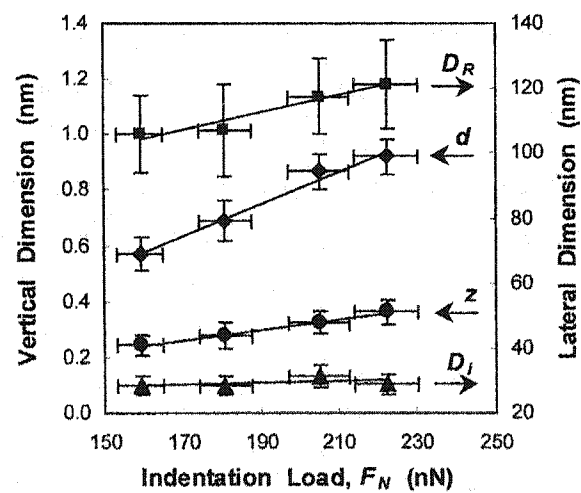 strain capacity of the material;[4] i.e. $E \tan\beta_{TIP} / Y$, where E is the sample modulus, β_{TIP} is the excluded tip-sample angle (imposed strain), and Y is the material yield stress. Bulk PS under quasi-static conditions exhibits a 3.0 GPa [20] and 110 MPa [21] modulus and yield stress, respectively. β_{TIP} was determined with scanning electron microscopy to be 52°. Thus, assuming bulk material behavior, the imposed strain versus strain capacity ratio for this system is 38, which exceeds the critical value (~30) for fully plastic deformation [4]. Moreover, for a ratio of 38, the elastic-plastic indentation simulations of Ramond-Angélélis indicate a uniform elastic recovery of roughly 10% in both the indent depth and diameter[12] This suggests that elastic recovery is not responsible for the high radial aspect of the indentations.

The model above assumes a quasi-static indentation process, which does not apply to the fast indentation rates employed here. Assuming that the plastically deformed volume is hemispherical with a diameter, D_p, equal to the rim diameter, D_R,[4,19] we would expect the plastic zone diameter to range from 20 to 40 nm for quasi-static conditions. This is based on Johnson's cavity model for elastic-plastic indentation[4] pictured in Figure 6.4-6 and on Nayebi's quasi-static plastic zone analysis, which relates D_p to the applied load and the material yield stress, through $D_p = 2(F_N / (2\pi Y))^{1/2}$.[22] The quasi-static case clearly underestimates the observed 70-160 nm rim diameter, and suggests that the strain rates have to be considered. The strain rates in our study ranged between 2×10^3 to 1×10^4 s^{-1}, determined from the measured residual strains (see below) and the short 10 µs indentation time. These rates exceed those of classical quasi-static indentation, and fall within the regime of impact dynamics.[23] At high strain rates, the material response becomes less sensitive to the indenter geometry, and depends more heavily on the material properties.[23] In other words, inertial forces may not be neglected, and the propagation of elastic-plastic stress waves may lead to large plastic deformations, as observed in this study.

Substrate effects have been neglected so far in our discussion. Examining the ratio of the rim height to the indentation depth, z/d, provides an initial assessment of any substrate constraints imposed during the indentation process. In Figure 6.4-7, the z/d ratio is reported as a function of film thickness, δ. The inset of Figure 6.4-7 shows the ratio of the $z(F_N)$ and $d(F_N)$ slopes, which are determined from the linear fits represented in Figure 6.4-5. For film thicknesses exceeding ~100 nm, the z/d ratio displays a constant value of approximately 0.2, and reflects the bulk material response. For film thicknesses below 100 nm, the rim height increases with decreasing film thickness.

MEAN CONTACT PRESSURE, p_m

CORE - PLASTIC BOUNDARY a_c

β_{TIP}

p_m

HYDROSTATIC CORE

ELASTIC - PLASTIC BOUNDARY

p_m

r_p

p_m

PLASTIC ZONE
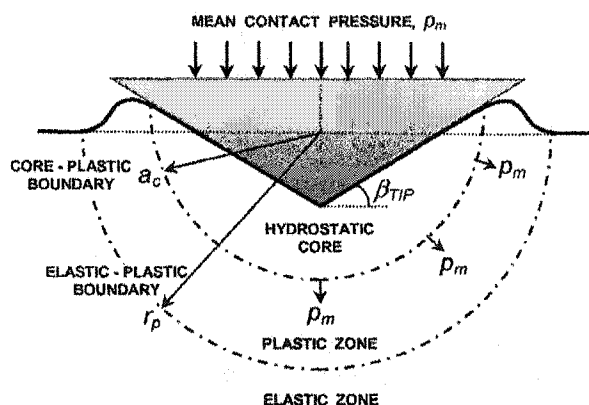
ELASTIC ZONE

Figure 6.4-6: Cavity model of elastic-plastic indentation by a rigid cone. Directly beneath the contact, the pressure is supported by a hydrostatic core. Beyond the core, lies the plastic deformation zone, where the pressure exceeds the material yield stress by roughly three-fold.[4] The plastic front is preceeded by elastic strain that accomodates pressures insufficient of producing yield. p_m is the mean contact pressure, a_c it the contact radius, r_p is the plastic radius ($^1/_2$ of the plastic diameter, D_p), and β_{TIP} is the excluded tip-sample angle.

This behavior was found to depend on the substrate material. The 45 nm film on the 230 nm PS-PCB buffer layer clearly did not display the enhanced rim formation apparent in the 45 nm film supported directly on silicon. This indicates that the rim enhancement phenomena is related to the distance from the rigid silicon substrate, not the film thickness itself.

Figure 6.4-7: Film thickness effect on the ratio of rim height to indentation depth. (inset) Averaged film thickness effect on the rim height expressed as the slope ratio of $z(F_N)/d(F_N)$ determined from Figure 6.4-5. The 45 nm PS film supported on the PS-BCB buffer layer exhibits bulk values.

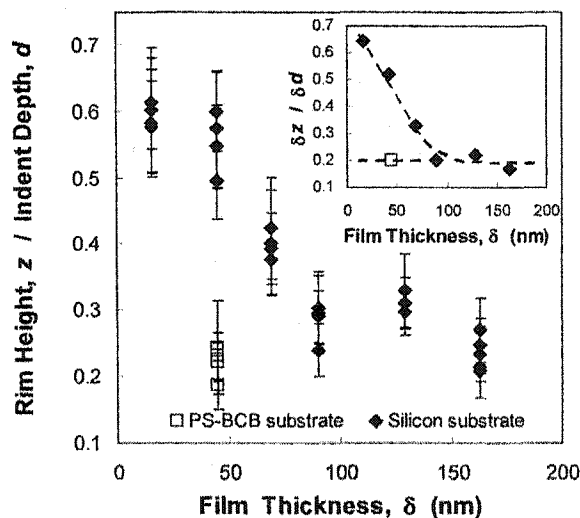Substrate effects during quasi-static indentations, such as enhanced rim heights because of strain shielding, are well known for indentation depths exceeding 10 to 30 % of the film thickness [16-19]. However, this high strain rate study clearly reveals that substrate effects are noticeable for residual indentation depths significantly less than 10% of the film thickness. This is not unexpected, as we have established above, that the large plastic deformations are due to elastic-plastic stress waves, which penetrate the material over larger length scales than those involved with quasi-static indentation.

An additional approach to acertaining substrate effects is by scaling the indentation contact radius, a_c, with the film thickness.[19,24] In terms of the indentation parameters, a_c is defined as $(z+d)/\tan\beta_{TIP}$. Following the formalism of Kramer et al.,[19] the evolution of the plastic zone radius, r_p, with respect to the contact radius, a_c, is plotted as function of a_c/δ in Figure 6.4-8. Recall that we have assumed that the plastic radius is equivalent to half of the rim diameter D_R. A collapse of the data onto a single curve is apparent, as noted by.[19] However, we find that the boundary $r_p = \delta$, indicated by the solid line in Figure 6.4-8, divides the plot into two regimes: (i) For $r_p < \delta$, the plasticity remains unconfined and increases with decreasing a_c/δ; (ii) For $r_p > \delta$, the plastic radius exceeds the contact radius by a constant multiple of approximately 25, indicating that additional plastic deformation is confined at the rigid silicon substrate. Contrary to quasi-static indentation (with an indenter aspect ratio close to one), this transition occurs for a contact radius equal to approximately 4% of the film thickness.

The z/d ratio is revisited in Figure 6.4-9 as a function of the plastic radius normalized by the film thickness. A sudden increase in the rim height is found when the plastic radius exceeds ~65 % of the film thickness. The rim height enhancement is a direct consequence of elastic strain shielding. The z/d ratio levels off once the plastic deformation zone comes into direct contact with the rigid substrate, i.e. the point corresponding to the onset of confined plasticity in Figure 8. The origin of the plateau for $r_p/\delta > 1$ is not entirely clear, but may arise from geometric changes of the plastic domain boundary (spherical to cylindrical) or from an increasing hydrostatic interaction with the substrate. Again, no strain shielding is evident in the PS-BCB supported 45 nm film, even for plastic zone radii in excess of the film thickness. This suggests that, relative to silicon, the modulus and yield stress of the crosslinked PS-BCB are sufficiently similar to the PS homopolymer to promote a more effective stress distribution across the interface. This can be referred to as a *modulus-matched interface*. In the absence of modulus-matching, shear stresses will concentrate at the interface,[25] and potentially compromise film stability.
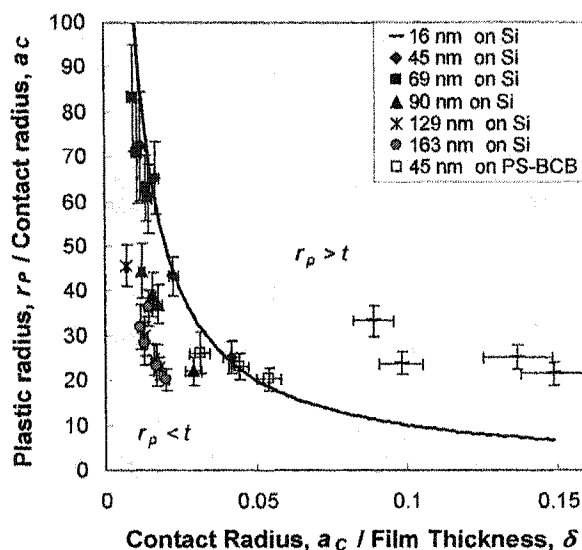
Figure 6.4-8: Evolution of the normalized plastic zone radius for increasing indentation depths, expressed in terms of the contact radius with respect to the film thickness. The solid line represents the boundary $r_p = \delta$.

To this point, the large plastic deformation relative to the indentation size has been attributed to inertial effects associated with high strain rates. The rim diameter appears to be the appropriate parameter to address the extent over which plastic stress waves have propagated from the indentation site.

So far, we have assumed that the films are homogeneous. Now, let us consider the repercussions of a structural anisotropy of the PS in the vicinity of the substrate. This discussion is motivated by multiple studies of thin films, which suggest strain and diffusion induced restructuring over a length scale on the order of 100 nm.[26-31] For instance, an anisotropic interfacial boundary layer in PS films of the same material studied here was shown to impact the glass transition temperature, T_g, within 200 nm of the substrate.[26] This is particularly relevant to the TDS process, in which the polymer storage medium is on the order of 50 nm thick.[2] Qualitatively, the nature of the interfacial T_g profiles in [26] suggests a non-monotonic gradient in the thermomechanical properties. That is, along with the T_g, the modulus is expected to increase with increasing distance from the substrate until a maximum, exceeding the bulk value, is reached at approximately 60nm from the interface. Beyond this point, the modulus is expected to decrease asymptotically to the bulk values at roughly 150-200 nm from the substrate.
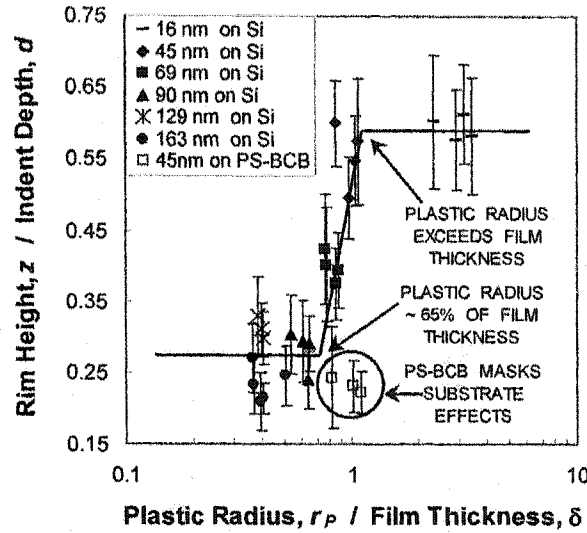
Figure 6.4-9: Evolution of the rim height for increasing plastic radius. Strain shielding and higher rims are observed when the plastic zone radius reaches approximately 65% of the film thickness on the silicon supported PS films. No strain shielding is observed for PS films supported on crosslinked PS-BCB substrates, even when the plastic radius exceeds the film thickness.

In the current study, the existence of structural anisotropy and its implication on the indentation process are found in analyzing the evolution of the indentation pressure with regard to the imposed strain, $\tan\beta$. The indentation pressure under elastic, elastic-plastic, and fully plastic conditions may be correlated in a dimensionless plot of p_m/Y as a function of $E\tan\beta/Y$, where p_m is the mean contact pressure defined as $p_m = F_N/\pi a_c^2$.[4] The angle β is illustrated in Figure 6.4-4, and for this analysis, represents the residual plastic strain. With a lack, a priori, of any spatial relationship of the film modulus and yield stress, the bulk, quasi-static values reported above are initially assumed. The data are plotted under this assumption in Figure 6.4-10.

The qualitative shape of the curve in Figure 6.4-10 deviates substantially from the isotropic bulk material case, in which the horizontal plateau is attributed to fully plastic deformation with a value of $p_m/Y \sim 3$.[4] Recall that the quasi-static, bulk material values for E and Y have been used. Strain rate hardening[32-34] is not accounted for; hence, the absolute values in Figure 6.4-10 are likely inflated and no inference of the asymptotic values is made. Nevertheless, this systematic error does not preclude a relative analysis regarding film anistropy.

The collapse of the indentation data into a continuous curve between two asymptotic limits suggests a distribution, or transition, between two mechanical scenarios: (i) a compliant surface

with a more rigid sub-surface, represented by the vertical asymptote in Figure 10; and (ii) a rigid surface with a more compliant sub-surface, represented by the horizontal asymptote.[35]
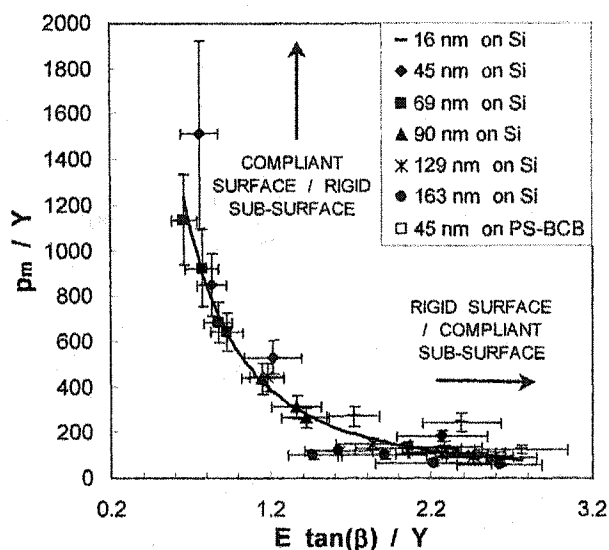

Figure 6.4-10: The non-dimensional indentation pressure – strain plot reveals a distribution between the two asympototic behaviors of (i) a compliant surface with a rigid sub-surface and (ii) a rigid surface with a compliant sub-surface.

Conceptually, this may be rationalized as follows: For a compliant surface with a rigid sub-surface, a finite strain is easily achieved as the surface yields. Additional strain becomes restricted as the more rigid sub-surface is capable of supporting much higher pressures. In the opposite scenario, a critical pressure is required to penetrate the rigid surface. Once the surface has been penetrated, the more compliant sub-surface is incapable of supporting the pressure and succumbs to large strains. Each asymptotic limit has been theoretically predicted for indentations of monotonically graded materials.[35] It is because of the non-monotonic rheological gradient within the thin PS films, that both asymptotes may be observed here in a single experiment.

Interestingly, the vertical asymptote in Figure 6.4-10 is comprised of indents in the intermediate thickness films, while both thicker and thinner films constitute the horizontal asymptote. The implications become apparent in comparing the thickness dependence of $p_m/\tan\beta$ to the interfacial T_g profiles, Figure 6.4-11. The ratio of $p_m/\tan\beta$ may be considered an effective modulus, where the pressure represents the applied stress, and $\tan\beta$ is the resulting

strain. Both the relative modulus and T_g are determined by normalizing by the corresponding film thickness dependent values to the bulk values obtained for the thick films (δ >150 nm).

Significant similarities exist between the modulus and T_g profiles in Figure 6.4-11. Viewing the glass transition as a mobility barrier, an increase in T_g offers additional resistance to intermolecular mobility, which intuitively, is accompanied by an increase in the modulus. Hence, the individual thermal and mechanical responses should be expected to coincide. The formation of these rheological gradients has been attributed to shear induced structuring during the spin casting process and to anisotropic diffusion during annealing (reference Chapter 5). The shape of the thermomechanical profile in Figure 6.4-11 implies: for films thicker than 150 nm, the material responds like the bulk; for film thicknesses between 60-120 nm the surface is more compliant than the immediate sub-surface; and for film thicknesses below ~ 60 nm, the surface is more rigid than the immediate sub-surface. For the latter case of a more compliant sub-surface, one would expect a *negative* rim height, or enhanced *sink-in* effect;[17] however, interaction of longer range plastic stress waves with the rigid substrate in the distant sub-surface most likely counterbalances any sink-in tendencies.
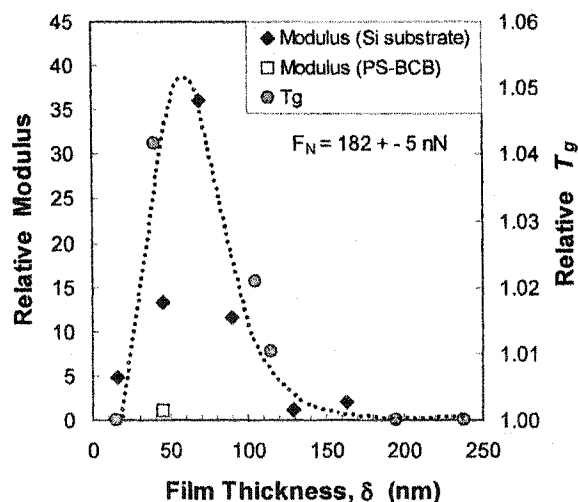
Figure 6.4-11. The interfacial thermal and mechanical response profiles for thin PS films is consistent with rheological boundary layer models (Chapter 5), and offers further support of a non-monotonic anisotropic configuration adjacent to the interface. The modulus data were determined from indentations with applied loads ranging between 170-190 nN, and the T_g data are from Figure 5.4-4.

The dotted line in Figure 6.4-11 is drawn so that the film thickness at the peak coincides with the thickness value of the peak in the T_g profiles determined from Figure 5.4-4, t~60 nm.

The 45 nm silicon supported film is somewhat of an anomaly, in that is spans the entire range between both asymptotes in Figure 6.4-10. While the shallowest indentations in the 45 nm PS-Si film fall on the vertical asymptote, the deepest indentations fall on the horizontal asymptote. This behavior may suggest that the actual peak in the thermomechanical response profile is close to 45 nm from the interface, which is still consistent with the T_g data obtained on separate films.

6.5 Chapter Summary

We have explored how the contact mechanics associated with thermomechanical storage in thin polymer films are compounded by: (i) high strain rates, (ii) the proximity of the underlying substrate, and (iii) material anisotropy near the interface. Strain shielding and confined plasticity at the polymer-substrate interface have led to bulk-deviating mechanical responses, which are manifested through the rim formation process during indentation.

For quasi-static indentations on thin film systems, substrate effects have traditionally been considered with regard to the rule of thumb: they may be avoided for indentation depths less than 10 % of the film thickness. Under high strain rate (10^3-10^4 s^{-1}), impact conditions, the scenario changes and inertial effects must be considered. While neither the indentation depths nor the contact radii exceed 10 % of the film thicknesses in this study, it is the radial aspect of the piled-up rims that indicates the plastic zone boundary and foretales of substrate constraints. This shift in scaling parameters is attributed to the propagation of plastic stress waves originating during impact.

Strain shielding becomes evident once the plastic radius reaches ~65% of the film thickness. At this point, the deformation front becomes confined by the underlying rigid substrate. Consequently, enhanced rim heights are observed, and the ratio of the rim height to indentation depth increases from 0.2 in the bulk material to 0.6 when the plastic zone spans the entire film thickness. Interfacial shearing is expected as the plastic boundary is pressed against a rigid interface, possibly activating dewetting instabilities and leading to delamination. In this context, superior film stability would be expected for systems in which the radii of piled-up rims do not exceed the film thickness. However, the mechanical constraints associated with rigid substrates are alleviated with the use of a thick, modulus-matched buffer film (230 nm crosslinked PS-BCB) between the surface film and the substrate.

Rheological anisotropy is apparent in the strain dependence of the contact pressure, and a non-monotonic mechanical gradient within the polymer is corroborated with interfacial glass transition profiles. Under these conditions, the indentation pressures are distributed between two asymptotic limits: (i) a compliant surface with a rigid sub-surface and (ii) a rigid surface with a compliant sub-surface. While enhanced rim formation is expected for the former, and enhanced sink-in for the later, it appears that, for the given thermomechanical profile, inertial confinement at the silicon substrate dominates the anisotropic constraints.

Beyond the immediate implications to the thermomechanical storage process, the work presented here shines a new light on the development of polymer thin film applications. With an understanding of how the interfacial boundary layers are formed (Chapter 5), and knowledge of how they influence rheological behaviors, one could imagine, that the ability to exercise control over the thermomechanical profiles offers a spectrum of possible outcomes: frictional dissipation, wear resistance, and film stability may be engineered for sundry applications. To this end, we foresee a resurgence of design methodologies, moving from the traditional approach of applying special coatings and surface treatments, to one where internal rheological gradients are catered to achieve the desired performance characteristics.

6.6 Notes to Chapter 6

[1] G. K. Binnig, G. Cherubini, M. Despont, U. T. Duerig, E. Eleftheriou and P. Vettiger, in *Springer Handbook of Nanotechnology*, ed B. Bhushan (Springer-Verlag, Heidelberg, 2004).

[2] P. Vettiger, G. Cross, M. Despont, U. Drechsler, U. Duerig, W. Heberle, M. I. Lantz, H. E. Rothuizen, R. Stutz and G. K. Binnig, *IEEE Trans. Nanotechnol.* 1, 39 (2002).

[3] I. Karapanagiotis, D. F. Evans and W. W. Gerbrich, *Polymer* 43, 1343 (2002).

[4] K. L. Johnson, *Contact Mechanics* (Cambridge University Press, Cambridge, UK, 1985).

[5] B. Bushan, *Principles and Applications of Tribology* (John Wiley & Sons, New York, 1999).

[6] Hill, *The mathematical theory of plasticity* (Oxford University Press, London, 1950).

[7] K. L. Johnson, *J. Mech. Phys. Solids* 18, 115 (1970).

[8] D. Tabor, *The hardness of Metals* (Oxford University Press, London, 1951).

[9] B. J. Briscoe, P. D. Evans, S. K. Biswas and S. k. Sinha, *Trib. Int.* 29, 93 (1996).

[10] M. J. Adams, A. Allan, B. J. Briscoe, P. J. Doyle, D. M. Gorman and S. A. Johnson, *Wear* 251, 1579 (2001).

[11] V. D. Jardret and W. C. Oliver, *Mat. Res. Soc. Symp. Proc.* 594, 251 (2000).

[12] C. Ramond-Angélélis, , Ecole Nationale Supérieure des Mines de Paris, 1998.

[13] R. Vaisyanathan, M. Dao, G. Ranichandran and S. Suresh, *Acta Mater.* 49, 3781 (2001).

[14] T. R. Malow, C. C. Koch, P. Q. Miraglia and K. L. Murty, *Mat. Sci. Eng.* A252, 36 (1998).

[15] J. R. Matthews, *Acta Met.* 28, 311 (1980).

[16] T. Y. Tsui and G. M. Pharr, *J. Mater. Res.* 14, 292 (1999).

[17] T. Y. Tsui, J. Vlassak and W. D. Nix, *J. Mater. Res.* 14, 2204 (1999).

[18] N.X. Randall, C. Julia-Schmutz and J.M. Soro, *Surf. and Coat. Tech.* 108-109, 489 (1998).

[19] D.E. Kramer, et al., *J. Mater. Res.* 16, 3150 (2001).

[20] D. Schrader, in *Mechanical Properties of Polymers*, edited by L. E. Nielsen (Reinhold Publishing Corp., Ney York, 1962), pp. V/91.

[21] C. Creton, J.-L. Halary and L. Monnerie, *Polymer* 40, 199 (1998).

[22] A. Nayebi, R. E. Abdi, O. Bartier and G. Mauvoisin, *Mat. Sci. Eng.* A333, 160 (2002).

[23] J. A. Zukas, T. Nicholas, H. F. Swift, L. B. Greszczuk and D. R. Curran, *Impact Dynamics* (John Wiley & Sons, New York, 1982).

[24] H. Gao, C.-H. Chiu and J. Lee, *Int. J. Solids Structures* 29, 2471 (1992).

88

25   A. E. Giannakopoulos, *Thin Solid Films* **332**, 172 (1998).

26   S. Sills, R. M. Overney, W. Chau, V. Y. Lee, R. D. Miller and J. Frommer, *J. Chem. Phys.* **120**, in press (2004).

27   S. Sills, J. Frommer and R. M. Overney, in *Applications of Scanned Probe Microscopy to Polymers*, ed. J. D. Batteas, G. C. Walker, and C. Michaels (Americal Chemical Society, Washington D.C., 2004), (in press).

28   R. M. Overney, D. P. Leta, L. J. Fetters, Y. Liu, M. H. Rafailovich and J. Sokolov, *J. Vac. Sci. Technol.* **B 14**, 1276 (1996).

29   R. M. Overney, L. Guo, H. Totsuka, M. Rafailovich, J. Sokolov and S. A. Schwarz, *Interfacially confined polymeric systems studied by atomic force microscopy* (Material Research Society, 1997).

30   R. M. Overney, C. Buenviaje, R. Luginbuehl and F. Dinelli, *J. Thermal Anal. and Cal.* **59**, 205 (2000).

31   C. Buenviaje, S. Ge, M. Rafailovich, J. Sokolov, J. M. Drake and R. M. Overney, *Langmuir* **19**, 6446 (1999).

32   G. Dean and B. Read, *Poly. Testing* **20**, 677 (2001).

33   H. Zhao, *Polymer* **39**, 1103 (1997).

34   H. Eyring, *J. Chem. Phys.* **4**, 283 (1936).

35   S. Suresh, A. E. Giannakopoulos and J. Alcala, *Acta mater.* **45**, 1307 (1997).

7. Interfacial Stability, Stress Transmission, and Mechanical Grading

7.0 Overview

Polymer thin film applications are, by nature, intricately dependent on the interfacial conditions between the polymer and its supporting substrate. The influence of substrate imposed dimensional constraints on rheological modifications in the polymer phase were discussed in Chapter 5, and the manifestations of these constraints in nano-contact mechanical operations was illustrated in Section 6.4. Here, issues pertaining to the stability and durability of both diffuse polymer-polymer and discrete polymer-substrate interfaces are addressed. Various approaches to promoting interfacial adhesion through mechanical and chemical coupling are presented in Sections 7.1 and 7.2, respectively, and the impact of residual interfacial stress on film adhesion is highlighted in Section 7.3. Once the critical aspects of interfacial stability have been established, a discussion of mechanical stress transmission across interfaces ensues in section 7.4; and the concept of mechanically graded, or *modulus-matched*, polymer films for enhanced interfacial stress transmission is investigated in section 7.5.

7.1 Mechanical Interlocking

A strong polymer-polymer interface is crossed by many chains that mechanically couple the adjacent materials. This interconnection can occur with long chains that physically entangle with each other or by chemically joining the chains through cross-linking.[2] For both elastomers and thermoplasts, the primary joining mechanism, or adhesion, across interfaces is polymer interdiffusion and entanglement between the opposing faces. The interdiffusion causes the strength of the interface to increase with time until it reaches the cohesive strength of the bulk material.[3] In order for interdiffusion to occur, the polymer chains must have sufficient mobility.[4]

One way to promote interdiffusion is to ensure that the polymers are at a temperature exceeding their respective glass transition temperatures, T_g.[3] Another way is to dilute the polymers at the interface by dissolving them in a solvent, which serves to increase their effective diffusivities. The later approach is best suited for solvent casting applications where one film is layered, by spin or dip casting, upon an existing film. During the *solvent exposure time*, i.e. exposure of the existing film to solvent prior to spinning or during dipping, the solvent in the polymer solution re-dissolves a fraction of the existing polymer surface, and the new polymer

can mix with the dissolved surface layer of the existing film. This effect creates an interdiffusion zone between each polymer film, pictured in Figure 7.1-1. The inderdiffusion zones constitute an entangled mix of the polymers from each film and act as a mechanical and possibly chemical bond between each film. The thickness of each interdiffusion zone, and hence the degree of inter-entanglement, is a function of the *solvent exposure time*. For polystyrene-polymethylmethacrylate interfaces, it has been found that the maximum interfacial strength is obtained when the interdiffusion zone thickness reaches approximately three times the mean entanglement spacing in the bulk.[5]
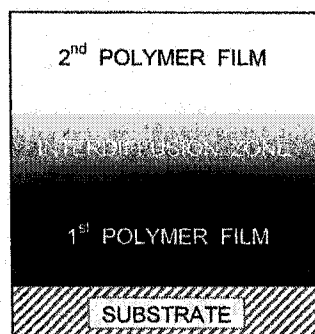

Figure 7.1-1: Illustration of the interdiffusion zone formed at polymer-polymer interfaces.

Interdiffusion zone thickneses may be measured by transition electron microscopy (TEM) or LFM on cross sections of the layered films. In addition, SM-SFM techniques may be used to measure the relative shear moduli of each polymer film and of the interdiffusion zone, allowing the mechanical gradient to be quantified. Because the interdiffusion zones are composed of a mix of the polymers from each adjacent film, modulus values of the interdiffusion zones are expected to fall between that of each adjacent film; therefore, the interdiffusion zones will contribute to smoothing the mechanical gradient across the interface.

For the case of polymers on rigid substrates, adhesion of polymer films may be enhanced by maximizing the interfacial area, i.e. by roughening the substrate surface. This provides the mechanical interlocking between the substrate and polymer.[1,6] If the surface roughness is sufficiently large, mechanical interlocking can be a dominant adhesion mechanism.[7] For metal substrates, several methods for inducing surface roughness include: pickling or etching in concentrated acid solutions (HF/HNO_3 or HCl/H_2SO_4)[8-10], alkaline etching,[11,12] hydrogen peroxide (H_2O_2) treatment[13-15], anodic oxidation,[16] and abrasive grit blasting.[8,17] Of the above techniques, only the acid etching techniques are capable of removing residual surface stresses, a

necessary condition for maximum adhesion (see below), because it consumes the milled/machined surface exposing the thermodynamically more stable and relatively stress free crystalline metal grains.[18] The HF/HNO$_3$ pickling process has been reported to leave a fluorine residue that can remain after post-etch thermal treatments.[18] The fluorine residue may lead to interfacial contamination, possibly activating dewetting instabilities in the polymer film.

The HCl/H$_2$SO$_4$ etching process was investigated with commercially available milled titanium foil (Alpha Aesar). Etching was performed by placing the titanium samples in a 50/50 vol.% solution of concentrated H$_2$SO$_4$ and HCl for a specified period of time. Figure 7.1-2 reports the titanium surface roughness measured by SFM as a function of etch time, and illustrates before and after SFM images of the titanium surface. The optimum etching time is 2.5 hrs; to little time in the acid solution will not maximize the roughness, and too much time in the acid solution will excessively consume the metal surface. Prior to etching, Figure 7.1-2B, smooth planar regions and milling defects are apparent on the titanium surface. After 6 hrs of etching, Figure 7.1-2C, terraced angular domains indicating HCP crystallized Widmanstatten plates[19] are obtained.
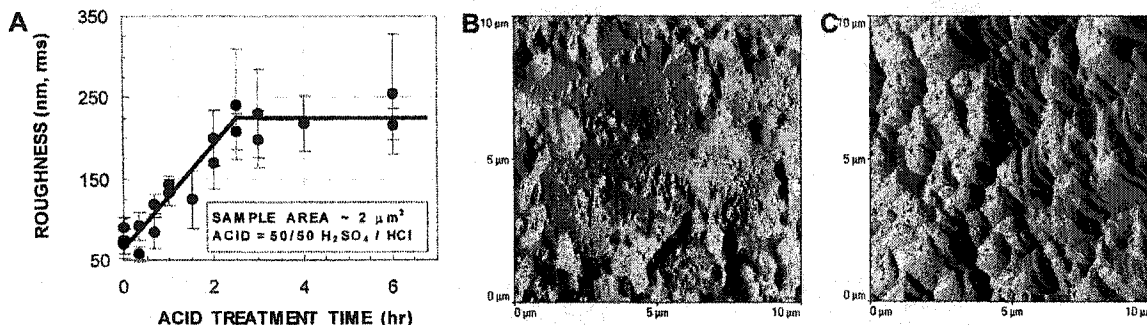
Figure 7.1-2: (A) Effect of acid etching time on titanium surface roughness. (B) 10μm SFM image of titanium surface without acid etching. (C) 10 μm SFM image of titanium surface after 6hrs of acid etching.

7.2 Chemical Coupling

In addition to mechanical interlocking, use of a chemical coupling agent, or adhesion promoter, further increases adhesion of the polymer interfaces.[1,6] For polymer-polymer interfaces, chemical coupling may be provided by chemical-crosslinking during or after the formation of the interface. Chemical coupling polymers to rigid substrates is somewhat more delicate because of the discrete (not interdiffuse) interface, i.e. on a molecular scale, the

interfacial area, thus the number of coupling sites, is much less with discrete interfaces. Adhesion is directly related to the concentration of coupling agents at the interface. Studies of elastomer adhesion on glass using a silane coupling agent, found that the threshold interfacial toughness, G_o, increases linearly with the number of chemical bonds across the interface.[20] Therefore, maximizing the interfacial area allows for the greatest number of potential bonding sites; however, the sites must be active with the appropriate chemistry for the coupling reaction.

For the case of titanium substrates, the surface oxide layer, TiO_2, is relatively inert. Only a few reagents are able to form strong chemical bonds with its surface: silanes, phosphates, and some photosensitive chemicals. Silane chemistry has been applied to TiO_2, surfaces for metal-metal and metal-polymer adhesion; however, silanes have a tendency to form multilayers through uncontrolled polymerization, where phosphates have been shown to form relatively stable, well defined monolayers.[21] On TiO_2 surfaces, the phosphate has been shown to replace the basic hydroxide (OH-) sites located on the outer most surface of the TiO_2 film.[22,23] Therefore, one may postulate that the degree of hydroxylation at the outermost TiO_2 surface is an important parameter for chemical coupling. Although evidence has been presented for the existence of hydroxides at TiO_2 surfaces exposed to air or vacuum, these surfaces may not be fully hydroxylated; however, TiO_2 surfaces in contact with water or H_2O_2 are believed to be highly hydroxylated.[24]

For the sequential process of introducing roughness for mechanical interlocking, followed by chemical coupling, one must consider that the acid etching step consumes the native oxide layer on the titanium surface. The TiO_2 surface is naturally regenerated under ambient conditions, and the surface chemistry prior to the coupling reaction will be a function of time between acid etching and reaction. The regeneration of the TiO_2 layer was measured on acid etched titanium as a function of post-etch ambient exposure time using electron scanning for chemical analysis (ESCA) and is illustrated in Figure 7.2-1.
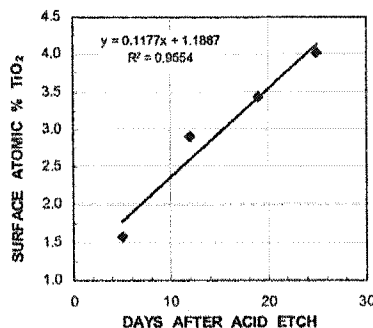

Figure 7.2-1: Post acid-etch regeneration of natural TiO_2 layer under ambient conditions.

The phosphate coupling reaction was conducted by submerging titanium samples in liquid phosphorus oxychloride ($POCl_3$) at room temperature for 1 hour. Following reaction, the titanium surface was dried under nitrogen. The concentration of phosphorus on the titanium surface was measured with ESCA, and preliminary results are presented as a function of titanium oxidation state in Figure 7.2-2.
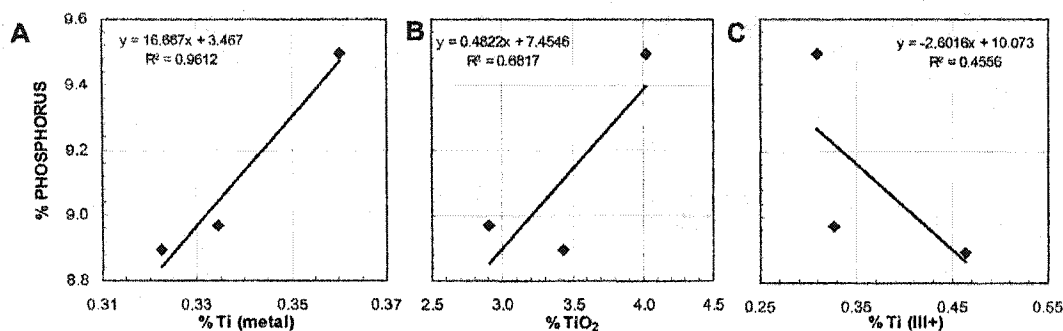

Figure 7.2-2: Phosphate coupling reaction yield: preliminary ESCA results indicating the surface phosphorus concentration as a function of A) titanium metal, Ti^0, B) TiO_2, and C) Ti^{III+} surface concentrations.

These preliminary results indicate that the surface concentration of phosphorus, representative of phosphate coupling groups, increases with the concentration of both titanium metal and TiO_2, and decreases with the presence of titanium in its less stable III+ state. The greater slope in Figure 7.2-2A compared to 7.2-2B suggests that coupling reaction yield is more sensitive to the presence of titanium in the metal form that to TiO_2. This study did not resolve the degree of hydroxylation of the TiO_2 surface, so the above hypothesis was not tested; however, it appears that the $POCl_3$ has a greater affinity of the metallic Ti^0 than for TiO_2.

Knowledge of the $POCl_3$ reaction yield alone is not sufficient to access the efficiency of the coupling; the homogeneity of phosphate coverage must be investigated. Ideally, a dense uniform coverage of coupling agents is desired. Any regions of reduced or absent phosphate coverage may act as delamination nucleation sites. The extent of phosphate coverage was examined by lateral force microscopy (LFM). Forward and reverse lateral force and topography images of the $POCl_3$ treated titanium are presented in Figure 7.2-3.

Uniform linkage group coverage is indicated by exact negative forward and reverse lateral force images. Inhomogeneous surface chemistry would be manifested through regions of

different friction coefficients and would appear as islands of negative contrast in the forward and reverse lateral force images.
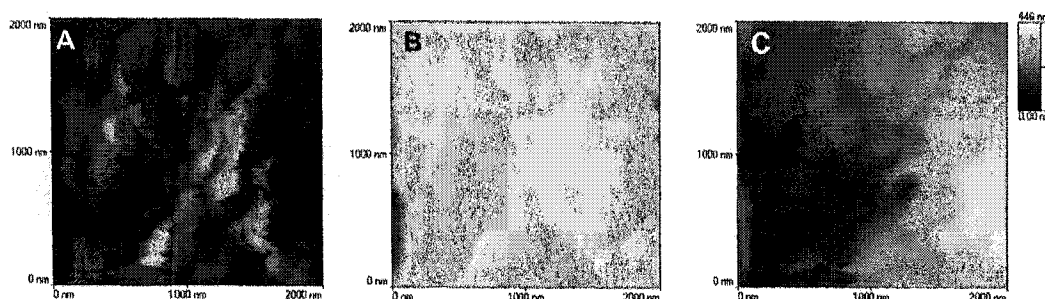

Figure 7.2-3: Determining phosphate linkage group coverage on the titanium surface. A) Forward scanning lateral force, B) Reverse scanning lateral force , and C) Topography images (2μm) of $POCl_3$ treated titanium.

Some lighter shaded features are apparent in Figure 7.2-3A that do not appear as dark regions in Figure 7.2-3B. However, these regions are also apparent on the topography image, Figure 7.2-3C, and are dismissed as topography induced artifacts. Hence on the ~10-2000nm scale, uniform phosphate coverage is indicated for $POCl_3$ coupling reaction.

7.3 Residual Stress Relief

Finally, to maximize the adhesion and stability of polymer interfaces, residual stresses in the substrate surface must be relieved and the polymer film must be anchored in a relatively low strain state. It is well known that residual stresses significantly influence the overall mechanical properties of multilayer systems, and it has been reported that, for polymer-metal interfaces, practical adhesion increases as residual stresses at the interface are reduced.[25] Several treatments are available for stress relief in metal substrates, the most common being thermal annealing.[19] Other treatments include pickling or etching in HF/HNO_3 or HCl/H_2SO_4 solutions, and electropolishing.[18] Electropolishing produces smooth uniform surfaces, counter productive for the goal of mechanical interlocking. The HF/HNO_3 pickling treatment has been attributed to interfacial contamination because of residual fluorine (see above). The HCl/H_2SO_4 etching discussed above, appears to be an acceptable treatment for both surface roughening and stress relief. Originally, thermal annealing was believed to be a suitable stress relief treatment, and

various combinations of acid etching and annealing have been tested. Thermal treatments were conducted by heating titanium samples in a O_2 rich laminar flame for 1 minute at ~800°C. We found that flame treating samples prior to acid etching rendered the titanium nearly inert in the acid solution, where acid etching followed by flame treatment produced an entirely different surface. Surface roughness values for the various treatment sequences were measured by SFM and are reported in Table 7.3-1.

Table 7.3-1: Effect of Surface Treatment Sequence on Titanium Surface Roughness

TITANIUM SURFACE TREATMENT SEQUENCE	SURFACE ROUGHNESS (nm,rms)
No surface treatments	71 ± 18
Flame Treated – no acid etching	74 ± 7
Flame Treated (air cooled) followed by Acid Etching	67 ± 11
Acid Etched followed by Flame treatment (air cooled)	173 ± 22
Acid Etched Titanium – no flame	206 ± 28

It is apparent that the flame treatment alone has no effect on surface roughness. Furthermore, acid etching the flame treated samples has no significant effect on surface roughness, suggesting a thermally induced change in surface chemistry. Lee has reported that thermal annealing reduces the concentration of titanium in its less stable states, II+ and III+, in the outermost nanometers of the oxide film. In addition, annealing in excess oxygen at temperatures >200°C, increases the oxide layer thickness from several nanometers to several tens of nanometers, and changes the oxide structure from amorphous or nanocrystalline to microcrystalline.[26] The combination of a more stable surface with fewer crystalline defects may present a pacified surface less susceptible to acid etching solution.

Acid etching alone produced a three fold increase in surface roughness compared to the untreated samples, and annealing the etched samples had a smoothing effect which appeared dependent on the cooling rate. In order to maximize surface roughness, acid etching must be the first treatment; however, if post-etch annealing is considered, the effects of cooling rate on roughness must be understood. Furthermore, it is generally known that rapid cooling or quenching may introduce residual stresses and a varied surface structure because of different internal and surface cooling rates. Three different cooling treatments were studied: air cooled, water quenched, and $POCl_3$ quenched, and the effect of cooling treatment on surface roughness is reported in Figure 7.3-1.

Figure 7.3-1A indicates that surface roughness is reduced by roughly a factor of two for quench cooled titanium. The roughness of water quenched vs. $POCl_3$ quenched titanium is similar, within experimental error. This suggests that chemistry of the quenching medium has little effect on the final surface roughness, and that cooling rate is a dominant factor in resulting surface structure.
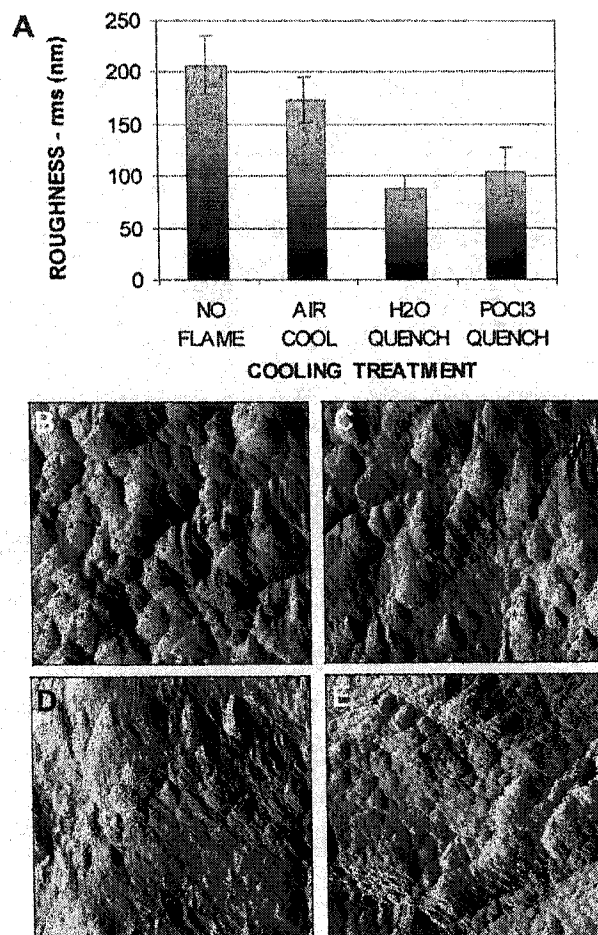
Figure 7.3-1: A) Effect of flame treatment on titanium surface roughness. 10μm SFM images of titanium surface after B) no flame, C) flame treated / air cooled, D) flame treated / water quenched, and E) flame treated / $POCl_3$ quenched. All samples were acid etched for 6 hrs. prior to flaming. The reduction in surface roughness for the quenched samples is seen in the images to the right.

Roughness of the air cooled surface is comparable to that of the non-flamed surface, indicating that slower cooling rates may offer a more thermodynamically equilibrated metal structure with lower degree of *frozen* internal stresses than the quenched samples. Our results suggest that

annealing at 800°C offers no specific advantage to acid etching alone from the standpoint of surface roughness and residual stresses; however, because the annealing may have changed the surface chemistry, the effects on the coupling agent reaction must be considered.

The POCl₃ coupling reaction was performed on acid etched titanium samples with and without the 800°C flame treatment, then the surfaces were analyzed with ESCA for surface compositions. The phosphorus concentration on the annealed titanium was only 55% of that on the un-annealed sample, indicating a reduced reactivity for the annealed surface. Lee has reported that annealing above 400°C leads to a considerable reduction in the surface hydroxyl concentration due to desorption.[26] Since hydroxides are believed to be involved in the phosphate coupling reaction (see above), it is possible that the reduced reactivity of the annealed surface results from the lower hydroxide concentration. Finally, annealing above ~500°C, causes a reduction in the strength and fatigue resistance of commercially pure (c.p.) titanium and most of its alloys. For load bearing implants, this is generally unacceptable.[24] Hence, the results of our surface chemistry and morphology studies combined with the detrimental bulk mechanical effects, suggest thermal annealing is not an appropriate treatment for the fabrication of a strong and stable titanium-polymer interface.

Considering the polymer side of the interface, the first polymer film, and any subsequent films, must be anchored in a relatively strain free state. Two predominant polymer film application techniques are spin casting[27,28] and dip casting.[29] Spin casting is generally employed for coating flat surfaces and is a viable technique for small sample preparation. To coat three dimensional surfaces, i.e. hip implant stems, dip casting is a more appropriate process. With respect to the incorporation of residual stresses in the polymer films, the high shear spin casting process has been reported to radially strain the polymer molecules from their thermodynamically stable *coiled* state (see Chapter 4). The residual stresses within the polymer at the interface are frozen within the structure, and remain present even following annealing above the polymer's glass transition temperature, T_g.[30] Compared to spin casting, dip casting is a much less dynamic process, and any incorporation of residual stresses within the polymer at the interface are postulated to be negligible.

7.4 Stress Transmission Across Interfaces

The capacity to transmit mechanical stresses across an interface is intricately related to the interfacial conditions, such as, morphology, chemistry, and residual internal stresses. In essence,

if the applied stress exceeds the elastic limit of the interface, i.e. the work of adhesion, the interface may fail. Adhesion fails when a crack propagates along the interface, thus adhesion studies require an understanding of crack propagation mechanisms in polymers. Resistance to crack propagation originates in viscoelastic and or plastic energy loss processes that occur close to the crack tip.[2] There are three primary mechanisms involved in crack propagation and interfacial failure: chain pull-out of the interdiffused molecules; chain scission, or breaking, of molecular bonds spanning the interface; and craze formation, an inhomogeneous nonelastic deformation involving stretching and simultaneous opening of voids within the polymer structure.[31] Three fracture mechanism regimes have been identified, depending on degree of polymerization of the interfacial molecules, N, and the number of molecules per unit interfacial area, or aerial chain density, Σ. (1) For $N >> N_e$, where N_e is the degree of polymerization for entanglements, the interfacial entanglement is adequate to prevent chain pullout, and chain scission is the dominant failure mechanism when $\Sigma < \Sigma_c$, where Σ_c denotes the critical aerial density necessary to initiate crazing. When $\Sigma > \Sigma_c$, a transition from chain scission to crazing occurs. (2) The second regime corresponds to $N \leq N_e$, where interfacial entanglement is weak, thus chain pullout dominates interfacial failure for $\Sigma < \Sigma_c$. In this regime, when $\Sigma > \Sigma_c$, a transition from chain pullout to crazing occurs. (3) In the third regime, $N << N_e$ and chain pullout occurs so easily that crazing is not possible for any value of Σ.[32] Higher fracture toughness, or adhesion, values have been associated with the chain scission compared to chain pullout;[3] however, the highest fracture toughnesses are generally achieved at interfaces with sufficient N and Σ to initiate crazing.[2,3,5,31,32] This is because the majority of the failure energy is dissipated during the deformation associated with the formation of craze fibrils.[31]

The efficiency of stress transmission across an interface is related to the bulk moduli of both phases comprising the interface. The more similar the adjacent moduli, the more efficient the stress transmission across the interface. This was illustrated in Figure 6.4-9 and discussed in section 6.4, where the mechanical constraints associated with rigid silicon substrates are alleviated with the use of a thick, polymer buffer film between the surface film and the substrate. These findings suggest that, relative to silicon, the modulus and yield stress of the polymer buffer film are sufficiently similar to the surface film to promote a more effective stress distribution across the interface. This can be referred to as a *modulus-matched interface*. In the absence of modulus-matching, shear stresses will concentrate at the interface,[33] and potentially compromise film stability. With the idea that modulus-matching improves interfacial stress

transmission, the problem of unstable *modulus-mis-matched* interfaces may be approached by generating quasi-continuous modulus gradients in the interfacial region (see below).

7.5 Designing Mechanically Graded Polymer Films

In this section, we will discuss a methodology for developing mechanically graded polymer films for improved stress transmission between two *modulus-mis-matched* faces. One relevant example is the transmission of physiological stress from a rigid titanium artificial hip implant (E = 100GPa) and the relatively compliant femur (E = 20 Gpa) (see section 7.1). One means of creating the mechanical, i.e. elastic modulus, gradient, is through successive layering of thin polymer films, each film synthesized with the specific mechanical properties necessary to achieve the desired gradient across the final layered composite, Figure 7.5-1.
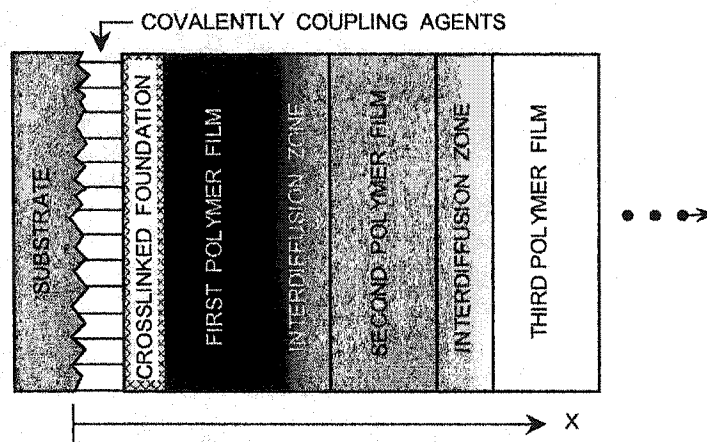
Figure 7.5-1: Schematic illustrating a mechanically graded, i.e. modulus-matched, interface: etched titanium surface, phosphate coupling agents, a crosslinked foundation, and successive polymer films with interdiffusion zones.

The specific materials investigated were those considered for stress matching in artificial hip implants (see section 7.1). These bio-polymers include: various custom synthesized hydroxalated branched polyurethanes (HBPU); and two commercial medical grade polyurethanes as control materials, Biospan SPU and Dow Pellethane. The HBPU molecules are comprised of a specific ratio of hard and soft segments; 4,4' diphenylmethane diisocyanate (MDI) / 1,3diamino-2-hydroxypropane (DAHP), and polytetramethyleneoxide (PTMO), respectively. The mechanical properties of the HBPU films are controlled by adjusting the ratio

of hard and soft segments. Three different HBPU polymers have been chosen to model the proposed application: HBPU 1, HBPU 2, and HBPU 3. Their MDI / DAHP / PTMO ratios are 15/14/1, 5/4/1, and 2/1/1, respectively.

The hypothesis that the desired polymer film properties can be tuned so that a stiffness gradient can be established in layered polymer film applications was quantitatively verified. Hardness and elastic modulus measurements on single layer titanium supported thick films were conducted with nanoindentation. The three HBPU films were studied and compared to the two commercial medical-grade polyurethanes in Figure 7.5-2.
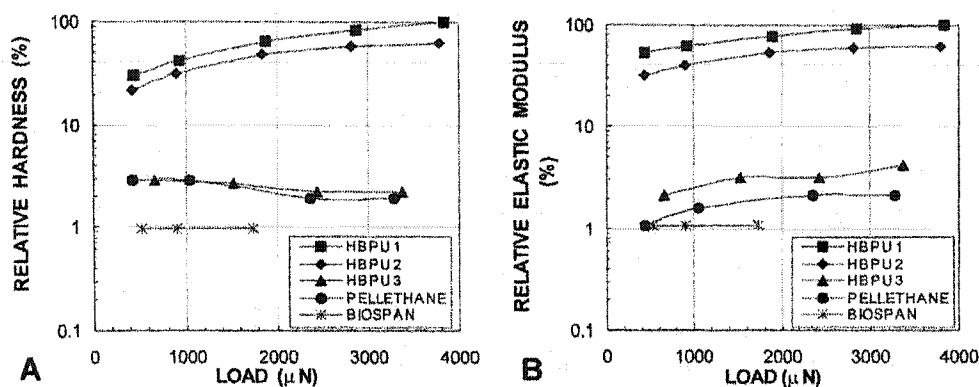

Figure 7.5-2: A) Relative hardness vs. applied load and B) Relative elastic modulus vs. applied load measured by nanoindentation on 25μm thick polyurethane films.

It is apparent that the relative polymer mechanical properties can be varied by changing the ratio of soft to hard segments in the polymer synthesis step. It is also seen that the properties of HBPU 3 are closest to the commercial samples, as this sample was modeled after the Pellethane. The hardness of the studied HBPU films is significantly lower than that of titanium. Future work will investigate the maximum hardness attainable by adjusting the segment ratio of HBPU and explore other variations in the polymer chemistry necessary to obtained the desired maximum polymer hardness., i.e. crosslinking.

Room temperature SFM topography images of the five polymer samples are presented in Figure 7.5-3. HBPU 1 reveals nearly circular domains, where both HBPU 2 and 3 appear to have more continuous wavy surfaces. When the hard-soft segmental ratio exceeds a critical value, crystallization of the hard segments may occur. Thus, it is believed the circular domains in HBPU 1 represent crystalline regions, indicating that the composition exceeds the critical

crystallization concentration of hard segments. The *cracks* in the Pellethane image are not *frozen* stress fractures $(T>>T_g\sim -40°C)$, but may indicate a degree of crystallinity within the sample. The depressions on the Biospan surface are ~0.5µm deep conical craters, possibly indicating contaminants present on the surface during film preparation. None of the PU films indicate any signs of dewetting on the Ti surface.

RMS ROUGHNESS VALUES

A) HBPU 1,   R=65±9 nm
B) HBPU 2,   R=79±9 nm
C) HBPU 3,   R=27±8 nm
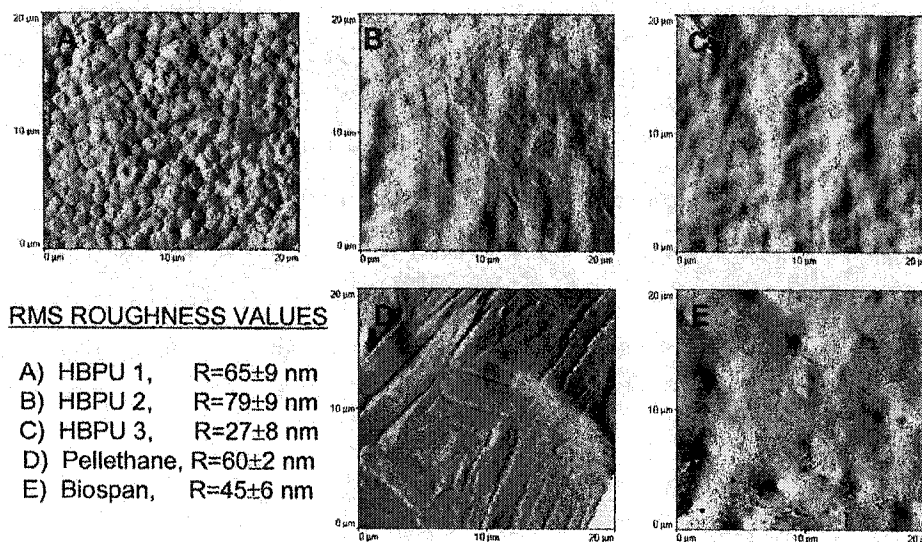D) Pellethane, R=60±2 nm
E) Biospan,   R=45±6 nm

Figure 7.5-3: SFM images and rms roughness values of the various bio-polymers.

Once the ability to tune the polymer hardness and modulus was quantified, the effect of these properties on film shearing behavior was investigated. The polymer shear response was measured as dynamic friction using LFM. Film hardness and adhesion were ascertained by nanoindentation and SFM, respectively, and compared to the dynamic friction measurements. For Pellethane and HBPU 1, the results are reported in Figure 7.5-4. Figure 7.5-4A indicates Similar adhesion forces for Pellethane and HBPU 1, and Figure 7.5-4B reveals that the hardness of HBPU1 exceeds that of Pellethane by an order of magnitude. The relative polymer shear responses, friction, are reported in Figure 7.5-4C.

The friction force on HBPU 1 is approximately 25% of the friction measured on Pellethane. Adhesive forces contribute to friction through the apparent normal load however, in this case, the friction results cannot be explained by adhesion alone, and the mechanical properties must be considered.
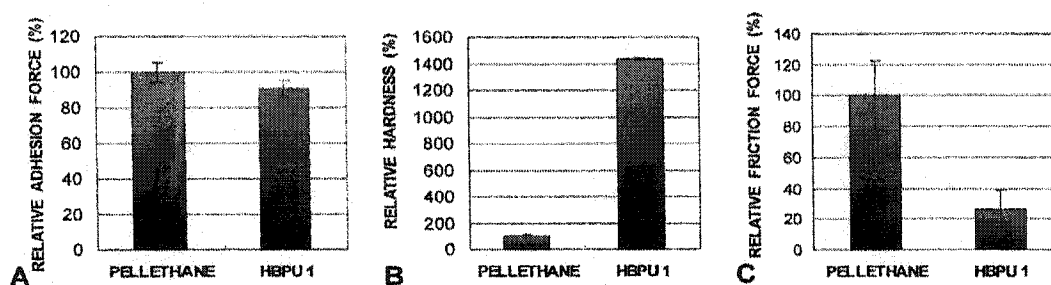
Figure 7.5-4: Comparing (A) adhesion and (B) hardness to (C) friction to understand shearing behavior of the polymer films. Results reported for Pellethane and HBPU 1.

A harder surface is less susceptible to elastic deformation under shear; therefore, less energy is dissipated in the process. Thus, lower friction force values are obtain for harder surfaces, given similar adhesion forces. This confirms that a gradient in polymer mechanical properties, i.e. hardness and elastic modulus, will produce a gradient in the shearing nature of the layered PU films.

7.6 Chapter Summary

Specifically for polymer-titanium interfaces, thermal annealing is not a suitable means for residual stress relief in titanium because of its negative effects on roughness, surface chemistry, and bulk mechanical properties. Acid etching has proved to be the best suited technique for inducing surface roughness and relieving residual surface stresses. SFM topography measurements have allowed us to determine the optimum etching time in the H_2SO_4 / HCl acid solution, and the preliminary ESCA studies provided insight to the regeneration rate of the surface TiO_2 layer following the etching process. Phosphate coupling agents have been identified as viable adhesion promoters to chemically anchor polymer films to titanium, and the preliminary ESCA studies suggest the yield of the coupling reaction is dependent on the oxidation state of the titanium at the surface. Additional ESCA studies must be conducted to validate the preliminary results, and to test the hypothesis that the reaction yield depends on the degree of hydroxylation of the TiO_2 surface. In order to vary the surface hydroxyl concentration, various titanium treatments must be considered: ambient exposure, aqueous treatment, and hydrogen peroxide treatment (see above). A more vigorous hydroxylation of the TiO_2 surface has been reported for hydrogen peroxide treatment, which results in a 10-fold increase in the

oxide layer thickness with a large hydroxyl concentration on the surface.[13]   Finally, The homogeneity of phosphate surface coverage on the micron scale was confirmed at short times with LFM; however, the long time stability of the phosphate-titanium bonds remains to be determined.

In general, interfaces can be designed for maximum stability through careful control of the interfacial conditions, such as, morphology, chemistry, and residual internal stresses. Several process for creating mechanical interlocking and chemical coupling of polymer interfaces were highlighted. In addition, methods for residual stress relief at interfaces were presented. The idea of using mechanically graded polymer film composites was introduced as one approach for creating modulus-matched interfaces with improved stress transmission characteristics and enhanced stability. The utility of modulus-matching was illustrated for thermomechanical data storage in polymer films and for improved stress transmission in artificial hip implants; however, a vast array of nano-mechanical applications stand to benefit from modulus-matching techniques.

7.7 Notes to Chapter 7

[1]   Y. Fujinami, H. Hayashi, A. Ebe, O. Imai and K. Ogata, *Mat. Chem. Phys.* **54**, 102 (1998).

[2]   H. Brown, *Mat Res Soc Symp Proc* **264**, 183 (1992).

[3]   H. Brown, *IBM J Res Develop* **38**, 379 (1994).

[4]   D. Allara, F. Fowkes, J. Noolandi, G. Rubloff and M. Tirrell, *Mater Sci Eng* **83**, 213 (1986).

[5]   H. Brown, *Macromolecules* **2001**, 3720 (2001).

[6]   S. Das, H. Manohara and C. Malek, *Proceeedings of the SPIE: The International Society for Optical Engineering.* **3225**, 85 (1997).

[7]   E. Kondoh, *Thin Solid Films* **359**, 255 (2000).

[8]   D. Buser, T. Nydegger, T. Oxland, D. Cochran, R. Schenk, H. Hirt, D. Snetivy and L. Nolte, *J Biomed Mater Res* **45**, 75 (1999).

[9]   C. Sitting, M. Textor, N. Spencer, M. Wieland and P. Vallotton, *J Mater Sci: Mater Med* **10**, 35 (1999).

[10]   M. Wong, J. Eulenberger, R. Schenk and E. Hunziker, *J Biomed Mater Res* **29**, 1567 (1995).

[11]   S. Nishiguchi, T. Nakamura, M. Kobayashi, H. Kim, F. Miyaji and T. Kokubo, *Biomaterials* **20**, 491 (1999).

[12]   H. Kim, F. Miyaji, T. Kokubo, S. Nishiguchi and T. Nakamura, *J Biomed Mater Res* **45**, 100 (1999).

[13]   J. Pan, H. Liao, C. Leygraf, D. Thierry and J. Li, *J Biomed Mater Res* **40**, 244 (1998).

[14]   C. Ohtsuki, H. Iida, S. Hayakawa and A. Osaka, *J Biomed Mater Res* **35**, 39 (1997).

[15]   J. Pan, D. Thierry and C. Leygraf, *J. Biomed. Mater. Res.* **30**, 393 (1996).

[16]   C. Larsson, P. Thompsen, B. Aronson, M. Rodahl, J. Lausmaa, B. kasemo and L. Ericson, *Biomaterials* **17**, 605 (1996).

[17]   M. Cabrini, A. Cigada, G. Rondelli and B. Vicentini, *Biomaterials* **18**, 783 (1997).

[18]   J. Lausmaa, in *Titanium in Medicine*, edited by D. Brunette (Springer-Verlag, Berlin, 2001), pp. 231.

[19]   D. Askeland, *The Science and Engineering of Materials* (PWS_KENT Publishing Company, Boston, 1989).

[20]   H. Brown, *Annu Rev Mater Sci* **21**, 463 (1991).

[21]   S. Xiao, G. Kenausis and M. Textor, in *Titanium in Medicine,*, edited by D. Brunette (Springer-Verlag, Berlin, 2001), pp. 417.

[22]   K. Healy and P. Ducheyne, *Biomaterails* **13**, 553 (1992).

23   T. Hanawa, in *The Bone-Biomaterial interface*, edited by J. Davies (University of Toronto Press, Toronto, 1991), pp. 49.

24   M. Textor, C. Sittig, V. Frauchiger, S. Tosatti and D. Brunette, in *Titanium in Medicine*, edited by D. M. Brunette (Springer-Verlag, Berlin, 2001), pp. 171.

25   J. Bouchet, A. Roche and E. Jaquelin, *J Adhesion Sci Technol* **15**, 345 (2001).

26   T. Lee, E. Chang and C. Yang, *J Mater Sci* **9**, 439 (1998).

27   A. Borkar, J. Tsamopoulos, S. Gupta and R. Gupta, *Physics of Fluids* **6**, 3539 (1994).

28   S. Middleman, *J Appl Phys* **62**, 2530 (1989).

29   T. Ito, Y. Okayama and S. Shiratori, *Thin Solid Films* **393**, 138 (2001).

30   C. Buenviaje, S. Ge, M. Rafailovich, J. Sokolov, J. Drake and R. Overney, *Langmuir* **15**, 6446 (1999).

31   J. Benkoski, J. Bates and E. Kramer, *ACS National Meeting; Orlando, FL* , **7** (2002).

32   J. Washiyama, E. Kramer and C. Hui, *Macromolecules* **26**, 2928 (1993).

33   A. E. Giannakopoulos, *Thin Solid Films* **332**, 172 (1998).

8. Stability Issues at Biological Interfaces

8.0 Overview

This chapter considers the design of bio-synthetic interfaces, with a primary focus on the interface between an artificial hip implant and the surrounding boney environment. Relevant terminology is defined, and the critical biophysical and biochemical phenomena are presented. Recent developments in the field are reviewed and discussed in the context of artificial hip design. Finally, a novel concept for prosthetic design is proposed that includes the necessary biomechanical modulus matching, biocompatibility in the sense of osseointegration, and both continuous drug delivery and diagnotsic sampling to and from the healing site.

8.1 Biomechanical Stability: Stress Matching in Artificial Hip Implants

Total hip arthroplasty (THA) has become a widely accepted practice with over 800,000 hip replacements carried out each year.[1] The standard prosthetic hip consists of a metallic femoral stem and head in contact with a metal backed ultra-high molecular weight polyethylene acetabular cup. Most of today's titanium implants are press fit into the medullary canal of the femur, and have an average life expectancy of 10-15 years.[2] Over the years, dominant hip implant failure modes have shifted from gross acetabular wear or catastrophic femoral stem failure in earlier years, to stem loosening caused by interfacial breakdown.[3] Usually, loosening of the femoral stem leads to failure of the prosthetic device.[2,4-6] Stem loosening results primarily from cortical bone atrophy in the vicinity of the prosthesis.[7,8] It is accepted that the bone loss results from stress shielding effects associated with an altered stress distribution within the femur.[8-12] The physiological load transfer mechanism in an intact femur is along the longitudinal axis in the proximal to distal direction and across the entire cross section of the fumur; however, in the artificial hip, loads are transferred by shear stresses across the implant-bone interface. The bone's response is an adverse adaptive remodeling, or resorption, resulting in a concentration of stresses at the interface.[1,13] Furthermore, the relative high stiffness of the titanium stem compared to that of the femur leads to an additional concentration of stresses at the interface.[9,13] This altered mechanical environment at the bone-implant interface can, in turn, cause or contribute to stem loosening.[13,14]

Effective long-term femoral stem stability requires a durable interface between the prosthesis and the surrounding bone. The interface must be capable of transferring high hip joint loads from the implant to the surrounding skeletal structure, and the loads should be transferred over an area large enough to minimize local stresses and relative stem-bone motion.[15,16] The apparent solution to the stress shielding problem will be a prosthesis which loads the proximal end of the femur in a manner similar to the natural process. Many studies have analyzed different stem geometries in order to understand and improve load transfer properties across the implant-bone interface. Gross et al. have shown that greater proximal load transfer and reduced stress shielding can be obtained with lower stiffness femoral stems (still stiffer than cortical bone).[1] Crownshield et al. have reported decreased interfacial stresses for increased stem cross section.[17] Kuiper et al. have indicated more favorable interfacial stresses with the use of shorter stems[18]; however, reducing stem length may have an adverse effect on bone-implant interfacial stability.[13] Gross et al., Schmidt et al., and Mattheck et al. have reduced stem stiffness by considering various hollow stem designs, and have reported up to 32 % increases in proximal bone stress, i.e. significantly reduced stress shielding.[1,19,20] Similarly, Engelhardt et al. have used transverse holes through the stem in order to reduce stiffness.[21] Prendergast et al. and Lewis et al. have studied the effects of collared stems as another means of increasing proximal femur loading.[14,22] Increased compressive axial and hoop stresses within the femur, i.e. reduced stress shielding, were reported for collared stems; however, difficulties maintaining sufficient collar-femur contact have arisen in clinical applications.[14] One critical issue with all reduced stiffness implants is that the shear stresses at the implant-bone interface increase with decreasing implant stiffness. Therefore, regardless of the degree of stress shielding abatement, the stem may become loose due to interfacial failure, if the additional shear stresses are not distributed effectively.[23]

In addition to geometry, the material properties, i.e. elastic modulus, play an important role in the resulting stiffness of the femoral stem. The compliance of prosthetic coatings, such as polymer films, serving as interpositional substances between metal stems and bone can have a profound influence on the stress distribution within the bone.[9] To address stress shielding, the concept of an *isoelastic* prosthesis has arisen, i.e. an artificial hip designed with the elastic stiffness to match that of the natural joint.[3] A number of isoelastic designs have been developed. In these cases, isoelasticity is usually achieved by using some type of composite materials. The most promising materials for endoprosthetic use consists of carbon fibers with a thermoplastic or thermoset epoxy matrix, which are either milled out of multi-ply laminates or filament wound using oriented continuous fibers.[23] Srinivasan et al. have studied the structural response and

relative strength of laminated fiber reinforced composite hips, and found that the neck of the femoral stem failed for all activities with the exception of the mid-stance phase of level walking.[24] Due to optimized fiber orientation, higher failure loads can be achieved with the filament winding process. The oriented fiber composite design investigated by Weinstein et al. utilized a ± 45° fiber winding around a unidirectional core. These prostheses were reported to be superior to metal designs with respect to stress distribution and resistance to loosening; however, problems were reported with their fracture strength.[25] Rotem has offered substantial improvements to composite designs by using a high strength / stiffness unidirectional composite core wound with an outer fiber layer which gradually reduces its elastic moduli from those of the core to those of the bone. The elasticity and stiffness gradients were controlled by varying the fiber volume fraction and winding orientation. Finite element analysis studies of this mechanical gradient design indicated that loads are successfully transferred from the composite hip in a manner resulting in the same bone stress levels as in the intact femur.[25] One of the most critical design issues with the composite prostheses remains the risk of femoral stem neck fractures, not generally an issue with stronger metal prostheses. At equal loads, higher strains are generated inside flexible implants compared with stiffer ones. Therefore, more flexible, less stiff, implants require superior fatigue properties to avoid stem fatigue fractures.[23] In order to build on the successful stress distributing attributes of the mechanical gradient composite hip of Rotem, we have applied the same *modulus* or *stress matching* concept to titanium hip implants, where stem fatigue fracture is not a critical issue.

The primary objective of this work focuses on improving the stress distribution from the artificial hip to the surrounding skeletal structure in order to reduce the effects of stress shielding, which have been attributed to cortical bone atrophy and subsequent catastrophic implant loosening. Furthermore, we intend to combine the hypothesized mechanical improvements with recent advances in the surface chemical and morphological aspects of cell osseointegration at the implant-bone interface (see section 8.2). The net result will be a unique design incorporating both biomechanical and biocompatibility technologies for enhanced artificial hip performance.

In our initial approach, we set out to develop a novel, polymer implant coating based on the concept of establishing a continuous mechanical gradient between the stiffer titanium implant (100GPa) and less stiff cortical bone (20GPa). To create the mechanical, i.e. elastic modulus, gradient, we have explored the idea of successive layering of polymer thin films, each film synthesized with the specific mechanical properties necessary to achieve the desired gradient

across the final layered composite (see section 6.5). As illustrated in Figure 8.1-1, three types of interfaces are relevant to stress matching with polymer thin films: *polymer-substrate* at the titanium surface, *polymer-polymer* between the films, and *polymer-biological* between the outer film and the cortical bone. The relevant issues and research results pertaining to the *polymer-substrate* and *polymer-polymer* interfaces were discussed in Chapter 6, and the specific concerns for the design of *polymer-bone* interfaces is discussed below.
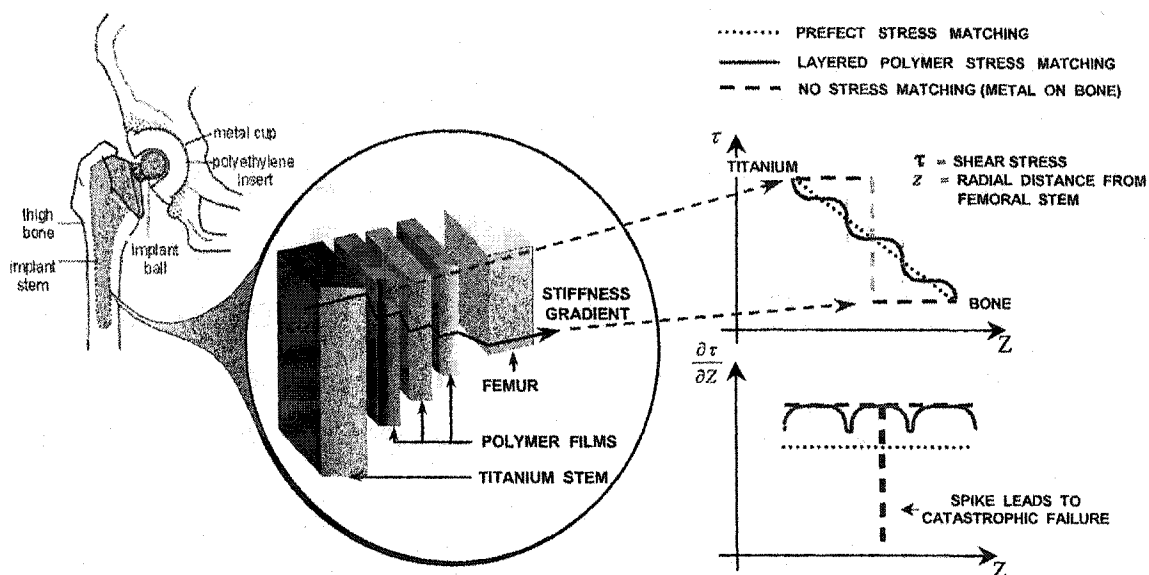

Figure 8.1-1: Qualitative illustration of how the layered polymer film assembly may be used to create a mechanical gradient across the titanium-bone interface. The mechanical properties of each polymer film are controlled during synthesis and are designed to provide stress matching between the relatively harder titanium and softer cortical bone. A mechanical interpretation of the stress matching is graphically illustrated. Only three polymer films are shown for example; however, the final polymer film assembly may consist of several films.

8.2 Biocompatibility: Osseointegration of Biological Interfaces

In addition to biomechanical integration, i.e. interfacial stress distribution (see above), a successful implant requires a biocompatible surface. The implant must be osseointegratable, or able to promote bone bonding, which is characterized by the attachment, proliferation, and differentiation of osteoblast cells on the implant surface, Figure 8.2-1.
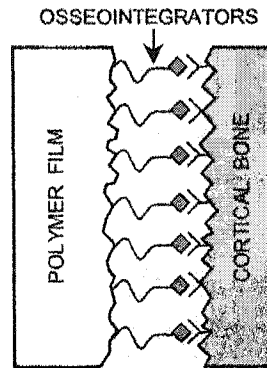
OSSEOINTEGRATORS

POLYMER FILM

CORTICAL BONE

Figure 8.2-1: Schematic illustration of an osseointegrated polymer-bio-interface.

The term *bone bonding* describes direct bone-implant contact with the absence of an intervening fibrous tissue layer at the interface. Generally, artificial materials implanted into bone environments are encapsulated by a fibrous tissue isolating them from the surrounding bone and preventing direct bone bonding.[26] Implant surface chemistry, surface roughness, surface energy, and surface topography have all been implicated in affecting bone bonding to implant surfaces.[27,28] It has been shown that the essential requirements for an artificial material to bond with living bone is the ability to form a bonelike apatite, i.e. hydroxyapatite, on the surface within the body, and that this formation of bonelike apatite can be reproduced in simulated body fluid (SBF).[26]

Various bioactive materials are used to treat implant surfaces for enhanced bone bonding.[29] Over the past three decades, researchers have shown that some ceramic glasses, glass-ceramics containing crystalline apatite, and sintered hydroxyapatite (HA) can bond to living bone.[30] The use of ceramics under highly loaded conditions, i.e. in artificial hips, poses a problem since their fracture toughnesses are not as high as that of cortical bone.[26] HA plasma spray coating is one of the most widely investigated and used methods for orthopedic implants. However, while HA plasma spray coated hip implants have produced encouraging short- and mid-term results, there have been several problems associated with the porosity, low fatigue strength, degradation, and delamination of the HA coating during long term implantation.[29] Inflammatory reactions and third-body joint wear resulting from the delamination of HA particles pose serious limitations on the use of plasma sprayed HA coatings in artificial hips.[31] In an *in vivo* study of plasma sprayed HA coatings, delamination and fibrous tissue infiltration beneath the delaminated HA were observed, and plasma sprayed HA coatings were not recommended for load bearing applications

without additional mechanical fixation.[32] The instability of the HA coating, whether applied by plasma spray coating, sputtering, electrolysis, or electrophoresis, arises from the inclusion of resorbable molten phases, leading to a degradation of the coating with time, thereby decreasing adhesion with both the bone and metal substrate.[33]

More recently, researchers have focused on biomimetic preparation of bonelike apatite coatings, i.e. processes mimicking the natural biological process, yet conducted ex-situ of the body. Sol-gel techniques have been applied to the titanium surface to produce a composite oxide layer of titanium, calcium, and silicon.[30,33] The porous composite is then soaked in SBF with physiologic pH and concentrations of calcium and phosphate ions. During the soaking, heterogeneous nucleation and growth of a carbonated apatite layer is achieved. The presence of carbonate ions aligned with the apatite lattice induces structural disorder and crystallographic defects, which are believed to favor biological apatite nucleation.[30] In a similar approach, the titanium surface is chemically treated with an alkali hydroxide solution and subsequently thermally treated.[26,29,31] The alkali treatment transforms the titanium surface into a hydrated titanium oxide gel containing alkali ions. The heat treatment dehydrates and densifies the gel to form an amorphous alkali titanate layer that is tightly bound to the titanium substrate. Next, the sample is soaked in SBF and the alkali ions are replaced with hydronium ions, resulting in the formation of a titanium oxide hydrogel surface. The release of the alkali ions increase the degree of apatite supersaturation within the SBF, hence the titanium oxide hydrogel experiences a bonelike apatite nucleation on its surface.[26] In both of the above techniques, the presence of bonelike apatite on the implant surface has been attributed to substantial increases in the bone bonding ability. However, the problem of stress distribution across the implant-skeleton interface remains. It is valuable to consider the relative success of these biomimetic approaches and to extend this process to polymer systems that may serve as an outer layer in the stress distributing polymer film assembly.

The use of degradable polymers as bone regeneration scaffolds has shown encouraging potential.[27,34-36] Tyrosine-derived polycarbonates have been proposed as biodegradable polymers capable of stimulating bone bonding and bone cell growth. The cell response was influenced by the chemical structure of the polymer, and a more stimulating response was found for the least hydrophobic polycarbonates, having the shortest ethyl ester pendent chains. These polymers were not cytotoxic toward cultured rat lung fibroblasts.[36] It has been proposed that the ability of these polycarbonates to induce bone bonding, stems from the facile hydrolysis of the ethyl ester groups, which creates calcium ion chelation sites at the surface carboxylate groups.[27] Similar to

the biomimetic processes above, the common theme in successful bone bonding appears to be the ability of carbonate ions or carboxylate groups to promote the mineralization of calcium and phosphate ions. Because these tyrosine-derived polycarbonates may be easily incorporated into the surface of the polyurethane films, they are considered an excellent candidate for osseointegration of the polymer film assembly.

8.3 Drug Delivery at Biological Interfaces

A major limitation in bone tissue engineering is the inability to induce rapid vascular ingrowth during bone tissue development. The vitality of cells that migrate from the native tissue into a regenerative site or scaffold is highly dependent on the ability to transport nutrients and wastes to and from the cells. Initially, transport occurs solely by diffusion, and cells more than several hundred microns from blood vessels either fail to engraft or rapidly die due to oxygen depletion.[35] Hence, it is necessary to provide the ingredients that promote both the formation of bonelike apatite, i.e. osseointegration, and the vascularization necessary to provide nutrients for the osteoblasts.

This vascularization process may be enhanced by the delivery of bioactive factors, i.e. growth factors, that trigger endothelial cells to behave in a specific manner.[36] Murphy et al. have developed a poly(lactide-co-glycolide) (PLG) degradable porous polymer scaffold capable of sustained release of vascular endothelial growth factor (VEGF) with simultaneous bone cell generation.[35] Similar to the biomimetic processes, a bonelike apatite layer is formed within the pores of the PLG scaffold and serves as a foundation for the mineralization of new bone. Concurrently, the VEGF is released at a controlled rate to induce vascularization. The presence of VEGF was reported to have no mitogenic effects on the bone formation process.[35] Such a *dual delivery* polymer scaffold is believed to be an ideal system for long term osseointegration of hard tissue implants with the cortical bone.

With these drug delivery concepts in mind, an alternate approach to stress matching in artificial hip implants is to incorporate the modulus gradient within the titanium itself. This is conceptually founded on the fabrication of a porosity gradient in the outer surface of the implant. One prospective method considers a novel foaming technique which yields the hypothetical titanium structure illustrated in Figure 8.3-1. The details of the foaming technique are still under development and go beyond the scope of this work.
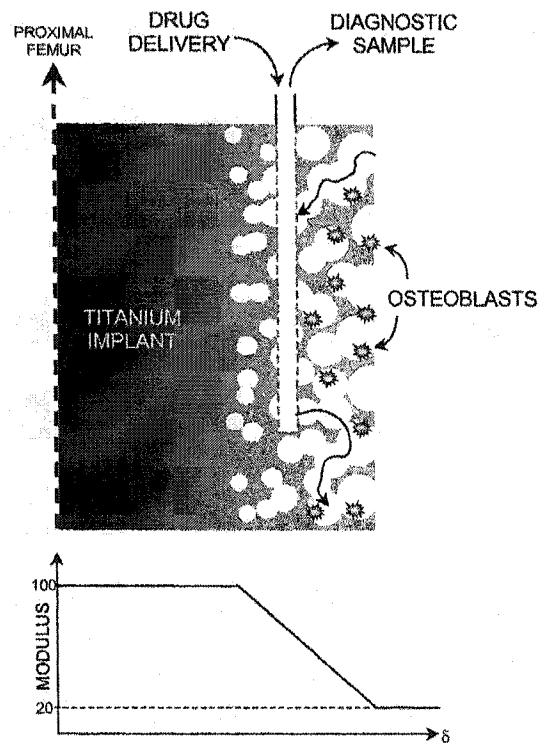
Figure 8.3-1: Modulus matching in artificial hip implants with a porosity gradient. The nature of the pore structure permits continuous drug delivery and diagnostic sampling to and from the healing site.

The surface of the *raw*, porous titanium would then be prepared for bio-implanting via the osseointegration process of Kukubo[26], or similar thereto. The nature of the pore structure permits continuous drug delivery and diagnostic sampling to and from the healing site. Drug doses will be dependent on the diffusion properties within the porous structure, which requires an understanding of the microscopic fluid flux within the porous titanium. One novel SFM based technique[37] shows great potential in-situ flux measurements, with local resolution on the submicron scale. Briefly, this method involves LFM friction studies on membrane surfaces as a function of the membrane pressure drop. In order to relate the LFM results to the membrane flux, I have developed the following model and tested it against the LFM nitrogen permeability measurements of He.[37]

The model assumes that uniform Knudsen diffusion occurs through the membrane pores. The diffusive stream produces a confined, pseudo-adsorbed monolayer film on the downstream membrane surface beneath the cantilever tip. The film, locally a two-dimensional bubble, grows

outward from each pore with a radial dimension related to the upstream pressure, as illustrated in Figure 8.3-2. The presence of the films, or two dimensional bubbles, provides a surface lubrication effect leading to reduced friction force measurements in LFM.
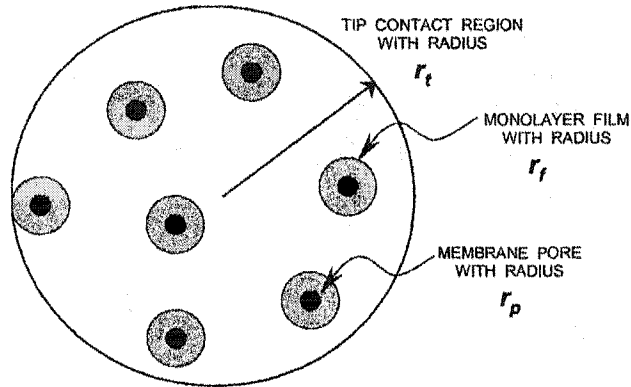

Figure 8.3-2: Monolayer film formation at membrane pores beneath a cantilever tip.

For membranes with a nominal pore size small relative to the contact area between an SFM cantilever tip and the membrane surface, the lubrication effect is modeled as a reduction in the actual contact area by the surface area of the bubbles between the tip and membrane surface. For a fixed number of pores within the tip contact area:

$$A_{real} = A_{tip} - \phi \cdot A_f \qquad (8.2\text{-}1)$$

where ϕ is the number of pores per tip contact area;

$$\phi = \frac{\varepsilon_m \pi r_t^2}{\pi r_p^2} \qquad (8.2\text{-}2)$$

and ε_m is the fraction of the membrane surface as open pores, a membrane property. The film radii are assumed to be a function of the number of molecules present within each film. It follows, that the number of molecules in one film is proportional to the flux through the membrane. The flux is related to the upstream pressure via:

$$q = -\frac{\beta \cdot \rho}{\mu \cdot h} \cdot \Delta P \tag{8.2-3}$$

where

β = coefficient of permeability

ρ = density

μ = viscosity

h = membrane thickness

ΔP = pressure drop across membrane (negative)

Assuming uniform flux throughout the membrane, the molecular flow rate in the area beneath the tip is :

$$\dot{n}_t = q \cdot N_{AV} \cdot \pi r_t^2 \tag{8.2-4}$$

The number of molecules permeating through the membrane while the tip is in contact with that area is:

$$n_t = \frac{\dot{n}}{t_c} \tag{8.2-5}$$

where the contact time, t_c, is defined here as:

$$t_c = \frac{2r_t}{v_{scan}} \tag{8.2-6}$$

with v_{scan} = cantilever scanning velocity. Combining equations (4), (5), and (6) yields:

$$n_t = \frac{2\pi r_t^3 \cdot N_{AV} \cdot q}{v_{scan}} \tag{8.2-7}$$

The number of molecules per bubble is then:

116

$$n_b = \frac{n_t}{\phi} = \frac{2\pi r_t \cdot r_p^2 \cdot N_{AV} \cdot q_s}{\varepsilon_m \cdot V_{scan}} \qquad (8.2\text{-}8)$$

Knowing the number of molecules per bubble, the size of the bubbles can be estimated if the size and orientation of the molecules in the monolayer films are known. Approximating the molecules as rigid spheres in hexagonal close packing yields:

$$A_f = \frac{n_b \cdot \pi r_m^2}{(1 - \varepsilon_{hcp})} \qquad (8.2\text{-}9)$$

where

ε_{hcp} = 2-D void fraction for hexagonal close packed circles

r_m = radius of rigid spherical gas molecule

The above assumes that the films are perfectly circular and that the contact time is small enough that the bubbles never grow large enough to come in contact with one another. In terms of flux through the membrane, the resulting expression for the actual tip contact area is:

$$A_{real} = \pi r_t^2 \left[1 - \frac{2\pi r_t \cdot r_m^2 \cdot N_{AV} \cdot q}{(1 - \varepsilon_{hcp}) \cdot V_{scan}} \right] \qquad (8.2\text{-}10)$$

Incorporating equation (3), the real tip contact area may be expressed in terms of the membrane pressure drop as:

$$A_{real} = \pi r_t^2 \left[1 + \frac{2\pi r_t \cdot r_m^2 \cdot N_{AV}}{(1 - \varepsilon_{hcp}) \cdot V_{scan}} \cdot \frac{\beta \cdot \rho}{\mu \cdot h} \cdot \Delta P \right] \qquad (8.2\text{-}11)$$

The model was tested against the LFM results of He for friction measured on the downstream surface of zeolite membranes during nitrogen flux[37] The model was used to describe the origin of the frictional dependence on the applied N_2 pressure. The problem, which we pose, is to find the critical pressure at which the tip-membrane contact is fully lubricated. Because of the very low viscous properties of gases we can assume that above the critical pressure, the frictional force should be close to zero. Our prototype membrane chamber allowed for

maximum pressures of 30 psig. Within that limit, we obtained frictional forces on zeolite membranes that were far from being close to zero. If the model is correct, then we can expect that the critical pressures of the investigated zeolite membranes are above 30 psig. The results from the mathematical model are plotted in Figure 8.3-3, and confirm our assumptions of critical pressures above 30 psig. The model prediction is consistent with He's results, however, further validation is required.
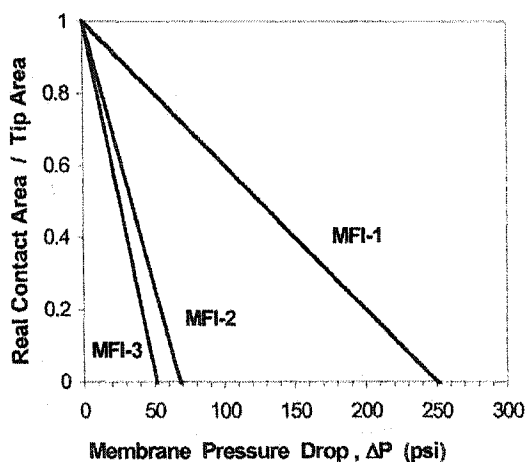

Figure 8.3-3: Predicted contact area vs. pressure drop. A reasonable molecular N_2 radius of 1.1 nm was assumed. The cantilever tip radius was restricted from 0.5 to 1 nm to avoid inconsistency. For this plot, the tip radius was chosen to be 0.5 nm.

8.4 Chapter Summary

The bio-synthetic interface concerns both bio-mechanical and bio-chemical integrations. The proposed artificial hip modulus matching technique is still in its conceptual stages, and constitutes an ongoing collaboration of scientists, engineers, and surgeons.

118

8.5 Notes to Chapter 8

[1]   S. Gross and E. Abel, *J. Biomech.* **34**, 995 (2001).

[2]   V. Barron, *Materials World* **5**, 656 (1997).

[3]   D. Taylor, C. Martin, B. Cornelis and M. Jones, *Proc Instn Mech Engrs* **207**, 121 (1993).

[4]   A. A. McBeath and R. N. Foltz, *Clinical Orthopaedics* **141**, 66 (1979).

[5]   R. N. Stauffer, *J. Bone Joint Surgery* **64-A**, 983 (1982).

[6]   C. J. Sutherland, A. H. Wilde, L. S. Borden and K. E. Marks, *J. Bone Joint Surgery* **64-A**, 970 (1982).

[7]   D. R. Summer, T. M. Turner, R. Igloria, R. M. Urban and J. O. Galante, *J. Biomechanics* **31**, 909 (1998).

[8]   H. Weinans, R. Huskies and H. J. Grootenboer, *J. Biomechanical Eng.* **116**, 393 (1994).

[9]   R. Poss, P. Walker, M. Spector, D. T. Reilly, D. D. Robertson and C. B. Sledge, *Clinical Orthopaedics* **235**, 181 (1988).

[10]   M. J. Silva, K. L. Reed, D. D. Robertson, C. Bragdon, W. H. Harris and W. J. Maloney, *J. Ortho. Res.* **17**, 525 (1999).

[11]   Z. Wan, L. D. Dorr, T. Woodsome and A. Ranawat, *J. Arthroplasty* **14**, 149 (1999).

[12]   H. Weinans, R. Huskies, B. V. Rietbergen, D. R. Summer, T. M. Turner and J. O. Galante, *J. Ortho. Res.* **11**, 500 (1993).

[13]   M. Joshi, S. Advani, F. Miller and M. Santare, *J. Biomech.* **33**, 1655 (2000).

[14]   P. Prendergast and D. Taylor, *J Biomed Eng* **12**, 379 (1990).

[15]   R. Crowninshield, *Clinical Orthopaedics* **235**, 166 (1988).

[16]   P. S. Walker and D. D. Robertson, *Clinical Orthopaedics* **235**, 25 (1988).

[17]   R. Crownshield, R. Brand, R. Johnston and J. Milroy, *Clinical Orthopaedics* **146**, 71 (1980).

[18]   J. Kuiper and R. Huskies, *J Biomech Eng* **14** (1997).

[19]   J. Schmidt and M. Hackenbroch, *Archives of Orthopaedic Trauma Surgery* **113**, 117 (1994).

[20]   C. Mattheck, U. Vorburg and C. Kranz, *Biomedizinische Technik* **35**, 316 (1990).

[21]   J. Engelhardt and S. Saha, *Med Bio Eng Computing* **26**, 38 (1988).

[22]   J. Lewis, M. Askew, R. Wixson, G. Kramer and R. Tarr, *J Bone Joint Surgery* **66-A**, 280 (1984).

[23]   C. Kaddick, S. Stur and E. Hipp, *Med Eng Phys* **19**, 431 (1997).

[24]   S. Srinivasan, J. d. Andrade, S. B. Jr and R. L. Jr, *Biomaterials* **21**, 1929 (2000).

25   A. Rotem, *J Med Eng & Tech* **18**, 208 (1994).

26   T. Kukubo, F. Miyaji and H. Kim, *J Am Ceram Soc* **79**, 1127 (1996).

27   K. James, H. Levene, J. Parsons and J. Kohn, *Biomaterials* **20**, 2203 (1999).

28   C. Larsson, P. Thompsen, B. Aronson, M. Rodahl, J. Lausmaa, B. kasemo and L. Ericson, *Biomaterials* **17**, 605 (1996).

29   S. Nishiguchi, T. Nakamura, M. Kobayashi, H. Kim, F. Miyaji and T. Kokubo, *Biomaterials* **20**, 491 (1999).

30   Q. Chen, N. Miyata, T. Kukubo and T. Nakamura, *J Mat Sci: Materials in Medicine* **12**, 515 (2001).

31   S. Nishiguchi, H. Kato, H. Fujita, M. Oka, H. Kim, T. Kokubo and T. Nakamura, *Biomaterials* **22**, 2525 (2001).

32   I. Kangasniemi, V. CC, E. van der Velde and K. de Groot, *J Biomed Mater Res* **28**, 563 (1994).

33   A. Stoch, W. Jastrzebski, A. Brozek, J. Stoch, J. Szaraniec, B. Trybalska and G. Kmita, *J Molecular Structure* **555**, 375 (2000).

34   T. Richardson, M. Peters, A. Ennett and D. Mooney, *Nat Biotech* **19**, 1029 (2001).

35   W. Murphy, M. Peters, D. Kohn and D. Mooney, *Biomaterials* **21**, 2521 (2000).

36   S. Ertel and J. Kohn, *J Biomed Mater Res* **28**, 919 (1994).

37   M. He, *private communication*, University of Washington, 2002.

9. Meso-mechanical Probing Techniques

9.0 Overview

Polymer surface and thin film technologies are receiving increased attention as unique mesoscale properties of polymeric systems become technologically important.[1-3] In particular, material property measurements at the submicron level are essential for the characterization of miniaturized electronic, optical, mechanical, and biomedical devices.[1,4] Furthermore, the need to understand the thermal behavior of polymer films is of critical importance when considering non-isothermal applications. For example, if a polymer coated device is implanted into a human body, engineering design must consider: the material properties at body temperature, polymer thermal transitions at or near body temperature, and any change in performance of the coating if the body temperature changes due to fever. In such thin film applications, bulk polymer studies are not always sufficient to address these issues, and techniques for evaluating the thermal properties of polymer surfaces and thin films on the nanometer scale are necessary.

Progress in this scientific field strongly depends on the development of appropriate techniques used to analyze surface and rheological properties on the micro- and nanometer scales. Over the last few decades, at least three techniques have been developed to meet these needs: the surface forces apparatus (SFA),[5] the scanning force microscope (SFM),[6] and depth sensing nanoindentation.[7] Interest in these techniques has been motivated by the attainable high spatial and force resolutions.[8] Numerous variations of these methods have evolved to allow for quantitative measurements on the nanometer scale.

9.1 Principles of Scanning Force Microscopy (SFM)

Scanning force microscopy originally evolved from the principles of scanning tunneling microscopy (STM). Like STM, a sharp probing tip is used for sub-micron analytical measurements on a sample surface. However, unlike STM, which requires a conductive sample in order to measure tunneling currents, SFM is based on the detection of mechanical forces and may be used on any type of surface. A typical SFM configuration is illustrated in Figure 9.1-1. The probing tip is attached to the end of a *Hookean* cantilever, and the normal force applied to the tip is directly proportional to the degree of bending, or displacement, of the lever. Following Hooke's law, the proportionality constant is the normal spring constant, k_N.
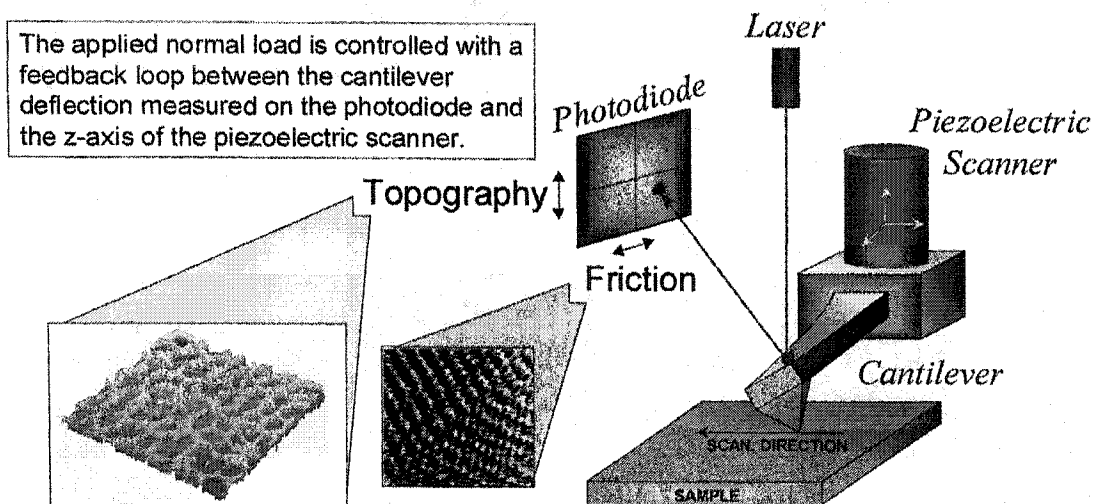
The applied normal load is controlled with a feedback loop between the cantilever deflection measured on the photodiode and the z-axis of the piezoelectric scanner.

Figure 9.1-1: Working principle of scanning force microscopy (SFM).

Piezoelectric actuators are used to drive the tip throughout x, y, z space. The forces acting on the cantilever are measured using a light deflection scheme. A laser beam is focused on the top side of the cantilever, and as the cantilever bends, the reflected laser beam is detected on a four quadrant photodiode. The magnitude of the laser deflection on the photodiode is directly related to the displacement o the cantilever. Both normal and lateral deflections are analyzed simultaneously, allowing concurrent topography and friction measurements. The applied normal load, F_{APP}, is controlled with a feedback loop between the normal deflection signal of the photodiode and the normal displacement of the z-piezo actuator.

SFM has a spacial resolution down to ~1nm and a force sensitivity ranging from $(10^{-11}-10^{-6})$N, depending on the cantilever spring constant. The versatility of the SFM is manifold. SFM may be used on hard and soft samples, conductors and insulators, and in a multitude of environments: air, liquids, magnetic fields, electrochemical settings, and under vacuum. The laboratory set-up of our Veeco Explorer SFM is pictured in Figure 9.1-2. SFM offers a multitude of analytical techniques, and creative new modes of operation continue to be developed. The four modes pertinent to the current work are discussed below.
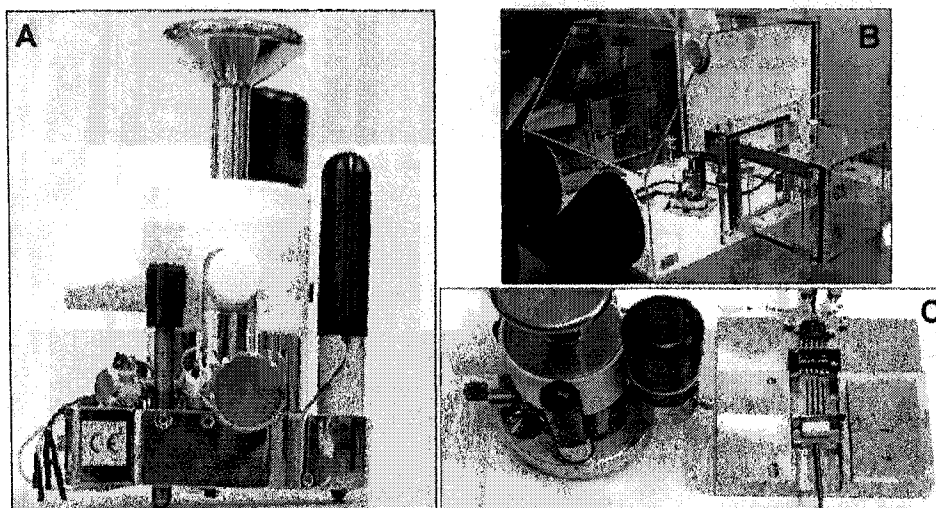
Figure 9.1-2: A Veeco Instruments Explorer SFM (A) is housed in a glove box (B) for environmental control. A MMR Technologies heating / cooling stage is used to control sample temperature (C).

9.2 Force Spectroscopy

Force spectroscopy is commonly referred to as the measurement of force-displacement curves. The principle of force spectroscopy relies on measuring the normal forces acting on the cantilever as a function of the distance between the tip and the sample. A typical force-displacement curve, pictured in Figure 9.2-1, is generated by a controlled approach of the tip to the sample, followed by contact with the surface. Once a specified applied load, F_{APP}, has been reached, the cantilever is retracted to its original displacement. The approach toward the surface starts with a free cantilever in a neutral position.
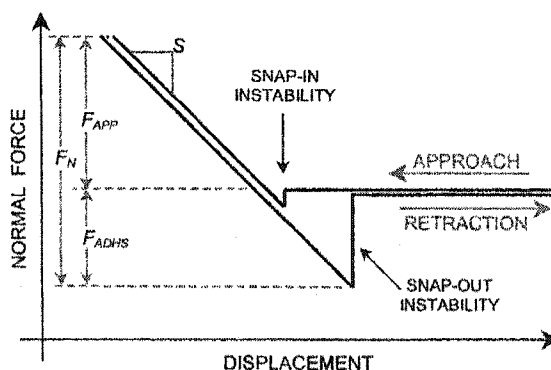

Figure 9.2-1: Generalized Force-Displacement Curve

In close proximity to the surface, a *snap-in* instability occurs when the attractive force gradient exceed the normal spring constant of the lever. Once contact is achieved, the cantilever is driven further into the sample until F_{APP} is reached. The slope, S, of this portion of the curve is referred to as the sensitivity, and is related to the both the cantilever and sample spring constants, via S^{-1} = k_N^{-1} + k_S^{-1}. When F_{APP} is achieved, the retraction cycle begins and the cantilever is *lifted* from the surface. The *snap-out* instability is reached when the adhesive force, F_{ADH}, between the tip and sample is overcome by retraction force of the cantilever. The total normal force, F_N, is the sum of the applied load and the adhesion force. Although various force spectroscopy techniques are possible, i.e. modulated approach curves,[9] in context of the current work, the application of force spectroscopy has been limited to measuring the force sensitivity and adhesion forces.

9.3 Lateral (Friction) Force Microscopy (LFM)

Lateral Force Microscopy (LFM) simulates a single asperity provided by an ultra-sharp tip on a soft cantilever. The small contact area, on the order of the molecular dimensions, is insufficient to coherently reorganize macromolecules and allows discussing LFM results in terms of thermodynamic equilibrium. The lateral force is measured as the torsional bending experienced by the cantilever during scanning under a constant load, pictured in Figure 9.3-1.
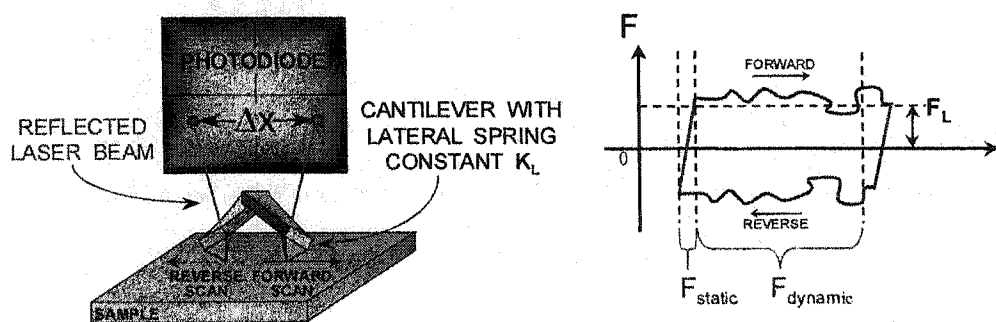

Figure 9.3-1: Lateral Force Microscopy. As the cantilever is scanned across the surface (left), the lateral deflection, Δx, is analyzed with an oscilliscope (right).

The magnitude of the hysterisis between forward and reverse scans is proportional to the energy dissipated through friction. For SFMs with optical detection schemes, the laser beam is deflected laterally on the photodiode, and the magnitude of the deflection is proportional to the extent of torsional bending, illustrated in Figure 9.3-1.

LFM images may be used to distinguish materials displaying different coefficients of friction, illustrated in Figure 9.3-2A. LFM imaging is valuable for assessing surface heterogeneity and decomposition of blends. Quantitative friction measurements are possible by analyzing the lateral displacement signal with an oscilloscope, Figure 9.3-1. The magnitude of the hysterisis between forward and reverse scans is proportional to the energy dissipated through friction. LFM offers sufficient sensitivity for friction measurements on the molecular scale, and has been used to detect molecular stick-slip behavior, pictured in Figure 9.3-2B.[10]
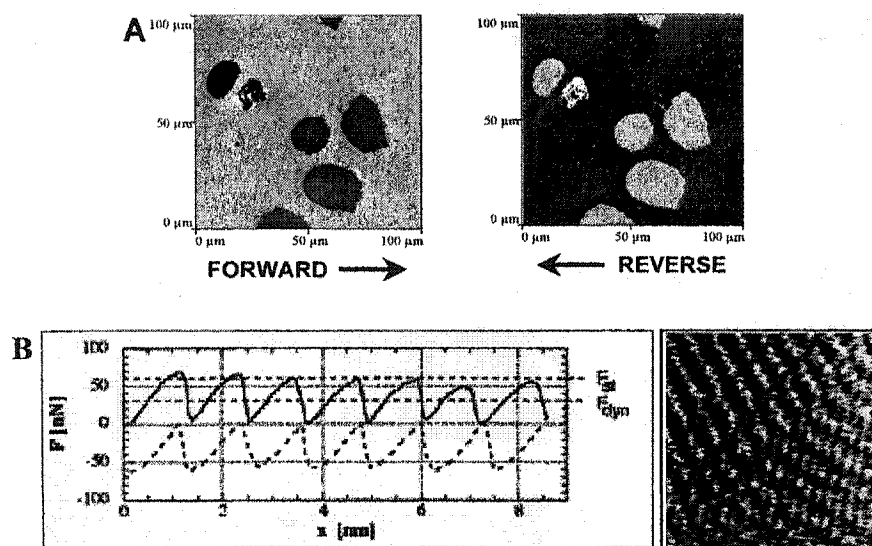

Figure 9.3-2: (A) LFM images reveal heterogeneous regions with different coefficients of friction – adapted from[11] (B) LFM molecular stick-slip measurements of a bilayer lipid system (5-(4'-N,N-dihexadecylamino)benzylidene barbituric acid)–adapted from [10].

Absolute values of friction force, F_F, may be determined by first calibrating the cantilever on a sample with a known coefficient of friction.[12] The coefficient of friction, μ, may be deduced from plots of F_F vs. F_N, where F_N is the total normal force. It is important that friction analyses on compliant materials are adhesion corrected, shown in Figure 9.3-3, to account for load dependent changes in the contact area, i.e. F_F must be described in terms of the normal force which is the sum of the applied load, F_{APP}, and the adhesion force, F_{ADHS}.
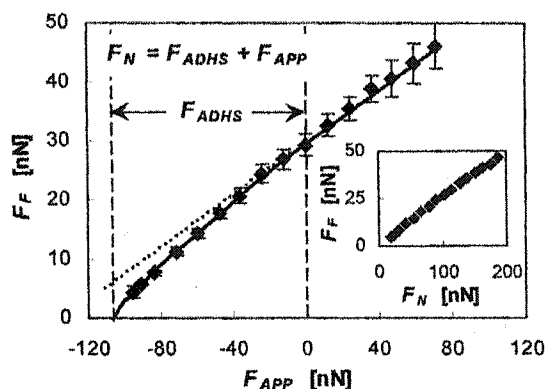
Figure 9.3-3: Adhesion correction of friction measurements on a PMMA film.

The ability to vary the scan velocity during friction measurements combined with a sample heating stage makes LFM especially well suited for investigating the frequency-temperature dependencies of viscoelastic materials. This is discussed in detail in section 3.5 and in Chapter 4.

9.4 Shear Modulated Force Microscopy (SM-FM)

Modulation techniques have offered significant improvement to SFM and nanoindentation capabilities. Normal force modulation techniques applied to both SFM and nanoindentation measurements offer improved sensitivity and have broadened the field of polymer research. For example, through normal force modulated SFM studies, a correlation between friction and elasticity of organic thin films has been obtained.[13] Shear modulated SFM techniques have proved to be particularly successful in determining crosslinking densities and structural phase transitions of ultrathin films.[1,14]

The working principle of the shear modulation force microscopy, SM-FM, method is sketched in Figure 9.4-1. It is a non-scanning nanorheological method that is well suited for any surface rheological study involving thermally activated transitions or relaxations. The method involves a nanometer sharp SFM cantilever tip that is maintained in contact with a sample surface under a constant load of (5-100)nN. The tip is laterally modulated with a nanometer amplitude, ΔX_{MOD}, that avoids any tip-sample slipping. The modulation response, ΔX_R, is analyzed relative to ΔX_{MOD} using lock-in techniques. The response amplitude is

a measure of the contact stiffness (i.e. sample modulus),[15] and is useful for tracking thermo-rheological transitions.

The cantilever is maintained in contact at a constant applied load, and is modulated in a sinusoidal manner, either laterally (shear) or normally, at a frequency exceeding the feedback response and at a specified amplitude, ΔX_{MOD} or ΔZ_{MOD}.

The modulation response, ΔX_R or ΔZ_R, is analyzed with two-channel lock-in technique, comparing the response signal to the input signal.

Amplitude Response contains modulus & contact information
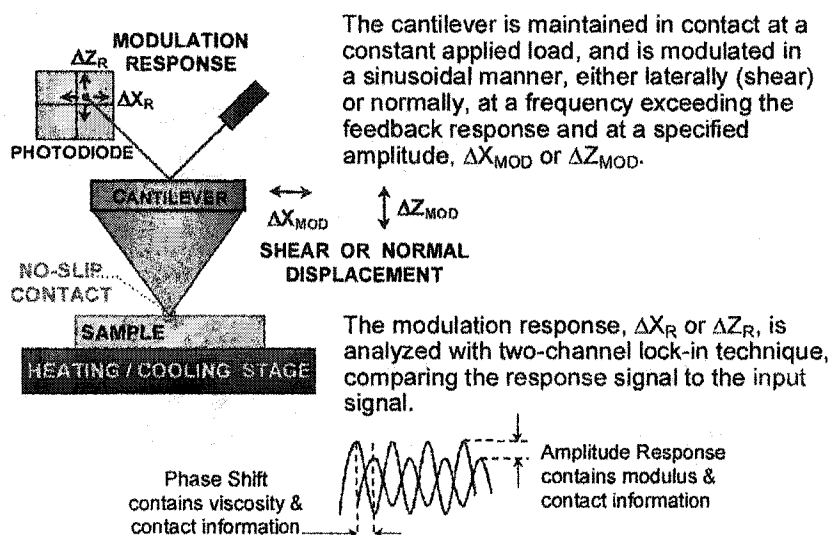
Phase Shift contains viscosity & contact information

Figure 9.4-1: Working Principle of Shear Modulated Force Microscopy

For thermal analyses, the sample temperature is increased stepwise by $(0.5\text{-}2.0)^{\circ}C$ increments. At each temperature, thermal equilibrium is obtained before any viscoelastic responses are recorded. The response amplitude is plotted versus temperature. For glass transition measurements, the T_g is determined from the "kink" in the response curve as reported in Figure 9.4-2A. Below the T_g, the probing depth of the SM-FM is on the order of 1nm, which allows *substrate-independent* measurements down to film thicknesses of a few nanometers. Any surface effects less than 1nm in depth[16] cannot be addressed under these conditions. The slow creeping process above T_g is documented elsewhere.[17] While the accuracy of SM-FM T_g measurements compares well with other techniques,[18] Figure 9.4-2B, SM-FM also offers the versatility for probing rheological properties in confined sample geometries.

It is important to note that the SM-FM method is a non-scanning method. The reason is briefly describe: To obtain high accuracy in T_g measurements it is essential, not to induce by other means than temperature, changes in the contact area. This is to avoid system-driven artifacts in the contact stiffness, k_c. To be precise, $k_c(A_L, G^*)$, i.e. the resistance of the contact to deform, is dependent on (a) the laterally projected contact area, A_L, (e.g., the side wall of an indentation dip), and (b) the relative shear properties of the two materials, G^*. Thus, any local

plastic deformation, for instance, the generation of a deformation wave (Schallamach wave)[19] that travels ahead of a scanning SFM tip can change k_c. Any plastic deformation is intrinsically rate and load dependent. Therefore, it is not astonishing that scanning methods, such as the friction force microscopy, revealed scanning velocity dependent apparent transition values for T_g.[15] By placing the SFM tip stationary at constant load onto the polymer surface, contact area changes occur only due to temperature induced changes in the rheological properties of the material. Consequently the experimental observable in our SM-FM method, k_c, is changing only due to changes in the polymer material properties. Hence, the "kink", observed in Figure 9.4-2A is a true measure of the transition property.
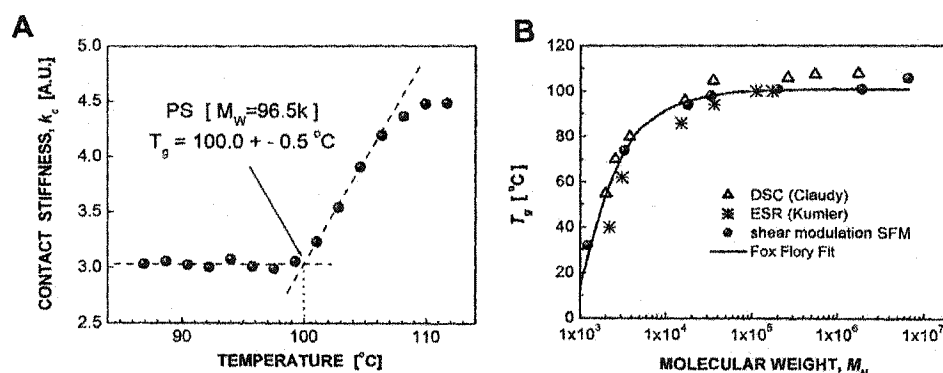

Figure 9.4-2: SM-FM glass transition temperature, T_g, measurements. (A) The modulation amplitude response indicating T_g. (B) Comparison of SM-FM T_g values as a function of molecular weight against other methods and theory- adapted from [18]

9.5 Heated Tip –Force Microscopy

Heated tip, or hot tip, scanning force microscopy (HT-FM) is an extension from conventional SFM, in that a resistive heating circuit is incorporated directly above the scanning probe, at the distal end of the cantilever. In addition to the typical SFM control parameters, HT-FM offers the ability of varying the probe temperature during operation. A spectrum of isothermal, non-isothermal, static, and dynamic experimental modes are possible with HT-FM. Thermo-mechanical indentation is of particular interest, considering recent developments in high density thermomechanical data storage.[20] The HT-FM cantilevers used in the current studies were designed for this purpose and fabricated at IBM's Zurich Research Laboratory. The and are designed with two heaters, one for bit writing and one for bit reading, and an electrostatic plate that is used for mechanical loading, illustrated in Figure 9.5-1.
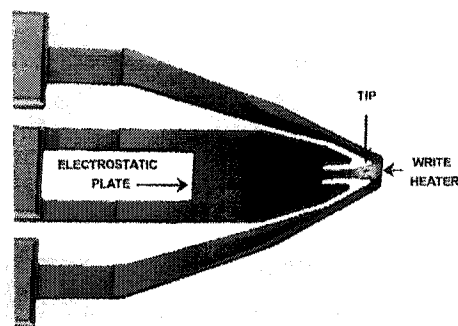
Figure 9.5-1: SEM image of an IBM HT-FM cantilever.

The electrostatic plate on the cantilever acts as a quasi-parallel plate capacitor with the sample, and when biased, generates an electrostatic force that drives the two plates together, i.e. pulls the cantilever tip into the fixed sample. The electrostatic loading mechanism offers a response time that exceeds that of conventional piezoelectric actuators, allowing high strain rate (exceeding to 10^{-4} s^{-1}), or nano-impact, indentation studies.

HT-FM operation requires, in addition to a complete SFM system, a cantilever holder designed to make electrical contacts with the cantilever, a heater bias buffering and sensing circuit, and a sample bias buffering circuit. Refer to Appendix A for cantilever holder designs for Digital Instrument and Topometrix SFM systems. Refer to Appendix B for an electrical diagram of the heater and sample bias buffering circuits. Ancillary equipment necessary for HT-FM operation includes: a storage oscilliscope, a pulse generator, a DC power supply (0-25V, 0-1A), and a multimeter. Differential amplifiers (1X) may be necessary to buffer both the heater and sample input biases, depending on the impedence of the bias source. One possible configuration of electronic components is illustrated in Figure 9.5-2.

For SFMs using an optical detection scheme, the angle of the lever with respect to the incident beam is critical. The combination of a short lever (100 μm) and an unusually thick chip on which the lever is attached may lead to a *shadowing* of the lever from the incident beam, i.e. the incident beam is eclipsed by the top side of the chip and does not hit the lever. In the event of a shadowing problem, the angle between the lever and incident beam must be adjusted. Aluminum foil shims may provide a quick fix to this problem. Following the above angle adjustments, the angle between the lever and sample may become sufficiently shallow that light reflected off the sample interferes with the detection signal, and the sample angle may need to be adjusted. In addition, the combination of a very wide lever with a short tip (500 nm) requires that

the lateral angle about the cantilever axis and with respect to the sample surface is must be minimized in order to avoid hitting the sides of the lever into the sample.
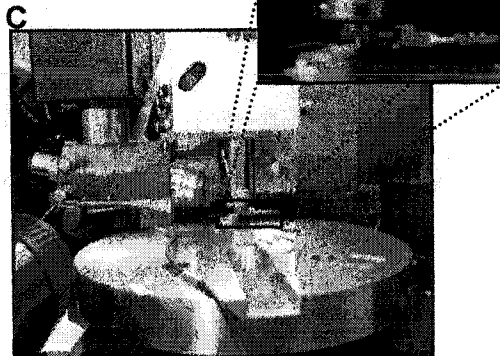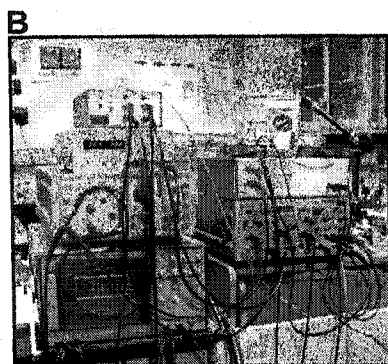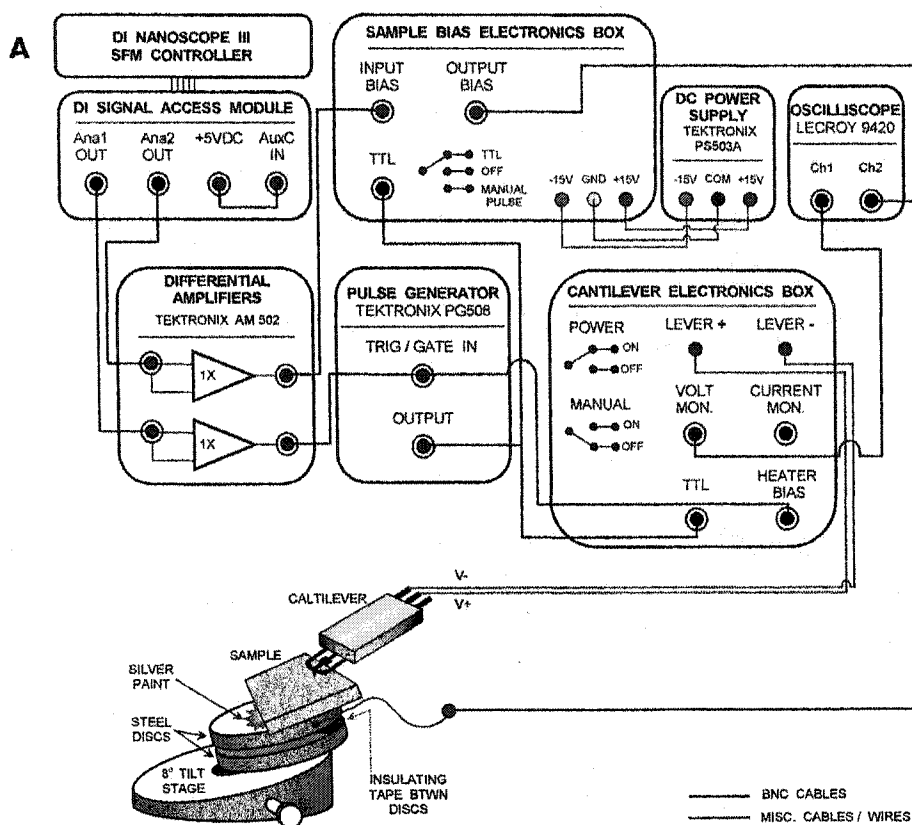

Figure 9.5-2: (A) Electronic configuration for HT-FM operation with a Zurich 3 leg cantilever, shown with a schematic of the sample stage - cantilever assembly. (B) Actual electronic setup. (C) Cantilever and sample holders mounted on a Digital Instruments Multimode / Dimension 5000

9.5.1 HT-FM Thermal Calibration

The tip heater incorporated into the cantilever is a resistive heating element, whose temperature is a function of the electrical resistance measured across the cantilever, R_{HEATER}. The objective of this calibration procedure is to determine the functional relationship $R_{HEATER}(T)$ and to relate this to the applied bias, ε. The HT-FM heater circuit is, in essence, a bias source with two resisters in series, illustrated in Figure 9.5.1-1.

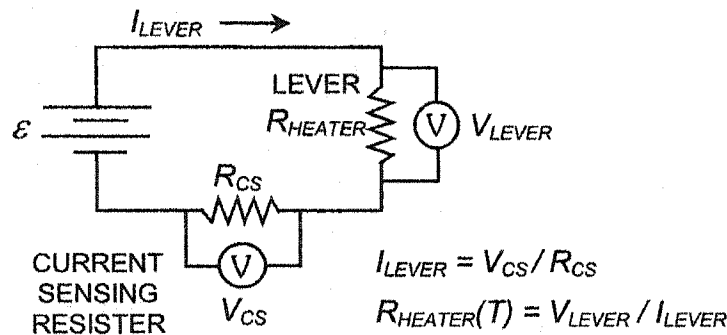Figure 9.5.1-1: HT-FM tip heater circuit.

One resister is the tip heater, and the second is the *current sensing resister*. For a given input bias, ε, the current flow through the circuit, I_{LEVER}, is determined from the voltage drop across the current sensing resister, V_{CS}. With the current and the voltage drop across the lever, V_{LEVER}, the resistance of the tip heater, R_{HEATER}, may be determined by Ohm's Law.

The details of determining the tip heater temperature from the tip heater resistance are outlined for both steady and pulsed heating in the following procedure. This calibration is expected to yield an absolute heater temperature with an uncertainty of $\pm$ 20%, and is based on the assumptions reported in Table 9.5.1-1. It should be noted that temperature at the apex of the tip will be less than the tip heater temperature; the heater is located on the lever, and heat is transferred by radiation to the air and by conduction through both the lever and the tip.

The first step in the thermal calibration is to measure an I-V curve for the tip heater. This is accomplished by analyzing both V_{LEVER} and V_{CS} (proportional to I_{LEVER}) in the x-y mode of a storage oscilloscope while ramping ε from zero to the *maximum voltage knee* (see Figure 9.5.1-2).

Table 9.5.1-1: Assumptions in HT-FM Thermal Calibration Procedure

1. 100% conversion of electrical power, P, to thermal heat, Q.
2. Electrical resistance, R_{EL}, is independent of time, but depends on temperature.

3. Heat transfer resistance, R_{TH}, is independent of heater temperature.
    a. convective heat transfer is negligible
    b. conductive heat transfer through tip to sample is negligible (small area)
    c. Majority of heat transfer is from heater to air (cond.), heater to sample (cond. through air), and conduction through silicon cantilever legs.

Once the oscilloscope data has been captured with suitable data acquisition software, the current, I_{LEVER}, is calculated from the current sensing voltage, V_{CS}, by:

$$I_{LEVER} = V_{CS}/R_{CS} \qquad (9.5.1\text{-}1)$$

where the current sensing resistance, R_{CS}, is 2200 Ω. A characteristic I-V curve for a HT-FM cantilever is illustrated in Figure 9.5.1-2.
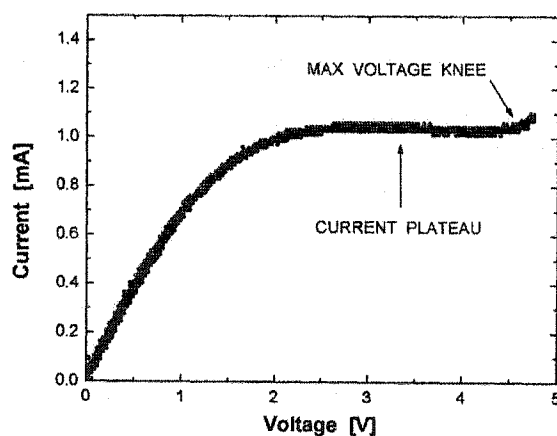

Figure 9.5.1-2. A characteristic I-V curve for IBM HT-FM Cantilevers.

The maximum input voltage is identified by the sharp knee following the current plateau (~5V), Figure 9.5.1-2. Overpowering beyond the knee may cause permanent damage to the lever or burn it out completely, pictured in the scanning electron microscopy image in Figure 9.5.1-3.
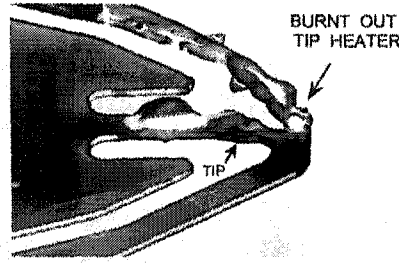
Figure 9.5.1-3: SEM image of overpowered lever reveals a melted tip and catastrophic failure.

Next, an *Equilibrium Temperature Curve* is generated with the I-V data. Determine the electrical power, P, input at each point, i.e.

$$P = I_{LEVER} * V_{LEVER} \qquad (9.5.1-2)$$

Note the value of the electrical power, P_{max}, at the maximum voltage knee, just following the current plateau. The temperature corresponding to this power value, T_{max}, is theoretically determined by the dopant concentration within the heater. The IBM HT-FM heaters are fabricated by doping the silicon with $5*10^{17}$ atoms/cm^3 of Phosphorous (P-doped Si), and the corresponding T_{max} is 550 °C.

The heater temperature for each point on the I-V curve may be approximated by a linear $T_{eq}(P)$ relation, which is interpolated between $T_{eq}(P=0) = T_{rm}$ and $T_{eq}(P=P_{max}) = T_{max}$, i.e.

$$T_{eq} = T_{rm} + \frac{(T_{max} - T_{rm})}{P_{max}} \cdot P \qquad (9.5.1-3)$$

Although the actual $T_{eq}(P)$ relation is slightly concave upward, the error associated with the linear approximation is ±20%. The temperature as a function of power will vary depending on the heat transfer environment, i.e. in or out of contact; hence, the heater temperature is most reliably expressed as a function of the heater resistance, R_{HEATER}. The heater resistance is calculated at each point on the *I-V* curve via:

$$R_{HEATER} = V_{LEVER} / I_{LEVER} \qquad (9.5.1-4)$$

The thermal calibration curve is generated by plotting the equilibrium heater temperature, T_{eq}, from equation 3 versus the heater resistance from equation 4. A characteristic $T_{eq}(R_{HEATER})$ curve for IBM HT-FM cantilevers is illustrated in Figure 9.5.1-4.
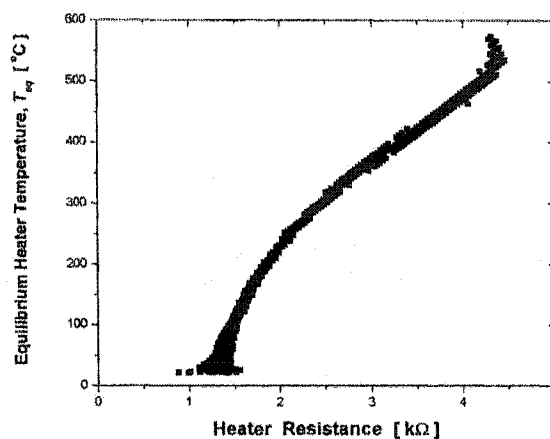

Figure 9.5.1-4: Characteristic thermal calibration curve, $T_{eq}(R_{HEATER})$, for IBM HT-FM levers.

When operating the heated tips in pulsed mode, thermal equilibrium may not be achieved, and the actual heater temperature, T_{ACT}, may be less than the equilibrium temperature. This is generally the case for pulses faster than approximately 100 µs, and is illustrated in Figure 9.5.1-5 for a pulse time of 10 µs.
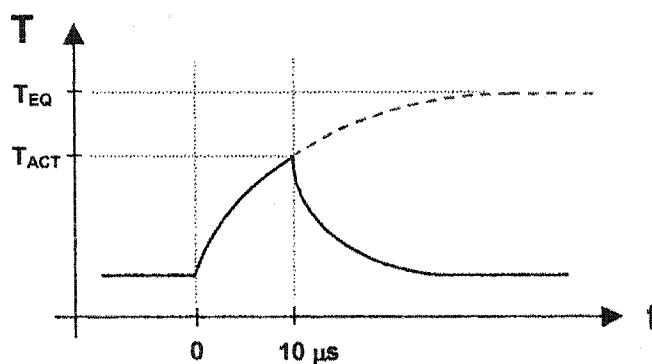

Figure 9.5.1-5: The actual heater temperature, T_{ACT}, is generally lower than the equilibrium heater temperature, T_{EQ}, when the cantilever is operated with 10 µs pulses.

The actual heater temperature, T_{ACT}, is determined from the resistance measured across the heater during the pulse. For a given input bias, V_{INPUT}, the voltage drops across the lever, V_{LEVER}, and the current sensing resistor, V_{CS}, are measured in the oscilliscope, and the resistance across the heater, R_{HEATER}, is calculated as illustrated in Figure 9.5.1-6.
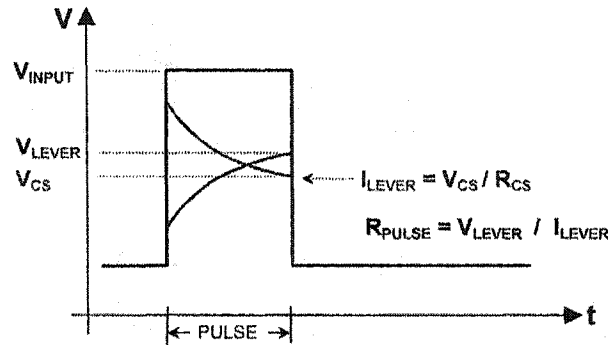
Figure 9.5.1-6: Determining heater resistance as a function of input bias during heating pulses.

The above process is repeated to obtain ~5 points across the input bias range. The measured heater resistance is correlated to the input bias, and an $R_{PULSE}(V_{INPUT})$ curve is generated, as pictured in Figure 9.5.1-7. In Figure 9.5.1-7, it is apparent that the linear approximation of $R_{PULSE}(V_{INPUT})$ breaks down at lower temperatures, i.e. at input bias values below ~3-3.5 V. This calibration must be used with caution, or improved, for pulsed HT-FM operations at these lower temperatures.

Figure 9.5.1-7: Correlation of heater resistance to input bias during pulsing.

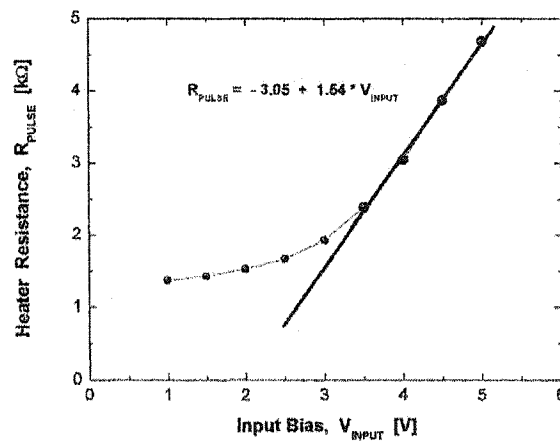Recognizing that R_{HEATER} in Figure 5 = R_{PULSE}, then the actual heater temperature achieved during a pulse, T_{ACT}, may be estimated by scaling the x-axis in Fig. 5 by $R_{PULSE}^{-1}(V_{INPUT})$, i.e. the curve T_{ACT} vs. V_{INPUT} may be generated. A representative thermal calibration curve for pulsed operation is reported in Figure 9.5.1-8.
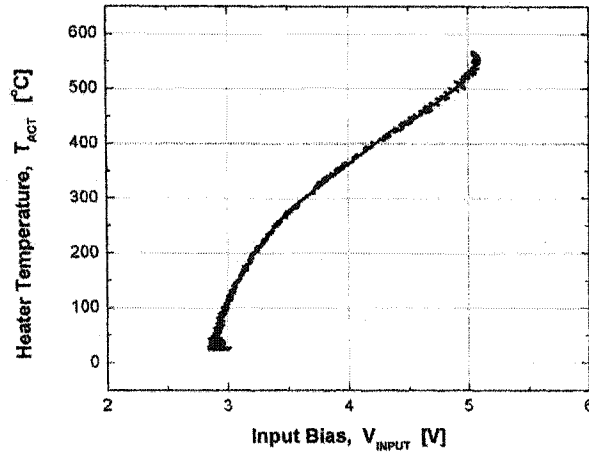
Figure 9.5.1-8: Characteristic pulsed heat calibration curve for the heater temperature of IBM HT-SMF Cantilevers.

Due to slight variations in the fabrication process, each cantilever must be calibrated independently. Furthermore, the thermal calibration for each cantilever is dependent on whether or not the tip is in contact, i.e. the energy balance about the tip is altered in the vicinity of a surface. Because of the fragile nature of the heated cantilevers, it is recommended to first calibrate the tip in close proximity to a sample surface (but not in contact) prior to conducting experiments. A full contact thermal calibration is recommended following the experiments, as this procedure may damage the tip.

9.5.2 HT-FM Electrostatic Force Calibration

When a bias is applied between the tip and the sample, the magnitude of the attractive electrostatic force, F_{ES}, will be proportional to the square of the absolute difference between the tip and sample biases, i.e.

$$F_{ES} = \alpha \left| (V_{INPUT, LEVER} - V_{SAMPLE}) \right|^2 \qquad (9.5.2\text{-}1)$$

Where the proportionality constant, α, represents the force calibration factor with units of force exerted / volt^2 of tip-sample bias. NOTE: with a positive lever bias (for the heater), the sample bias must be negative in order to maximize the capacative loading of the cantilever.

The force calibration is obtained by measuring the additional z-piezo displacement required to reach the snap-out instability during a force – displacement curve, ΔZ, as a function of applied sample bias, Figure 9.5.2-1. The electrostatic force is the product of the additional z-displacement and the normal spring constant of the lever, i.e. $F_{ES} = C_N * \Delta Z$ where C_N is approximately 0.1 N/m.

Using the above method, the electrostatic force is measured for several values of the sample bias. The force is calibrated to the square of the applied bias, and a linear regression fit is applied to determine the value of α in equation 9.5.2-1. Refer to Figure 9.5.2-2. The value of α is the electrostatic force calibration constant.
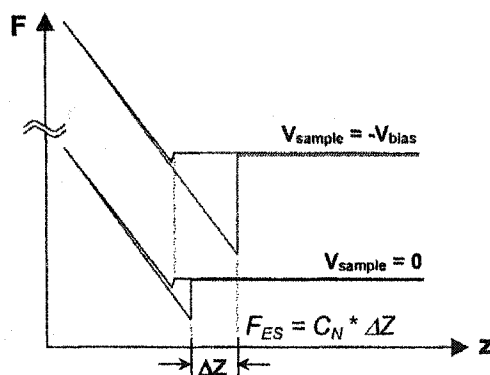
Figure 9.5.2-1: The electrostatic force, F_{ES}, or normal load, for a given sample bias, V_{bias}, is determined from the additional displacement of the z-piezo necessary to reach the snap-out instability, ΔZ.

The electrostatic force is a function of the overall bias between the cantilever and the sample. If a heater bias is applied, the electrostatic force will change, and the force calibration constant will change, see Figure 9.5.2-2. Conducting the force calibration with a hot tip may lead to contamination of the tip; therefore, an initial cold tip calibration is recommended prior to experiments, followed by a hot tip calibration after experiments. Once the cantilever has been calibrated, the system is ready for measurements. The system may be used in contact mode with either constant or pulsed temperature and or force, whichever combination is best suited for the experiment.
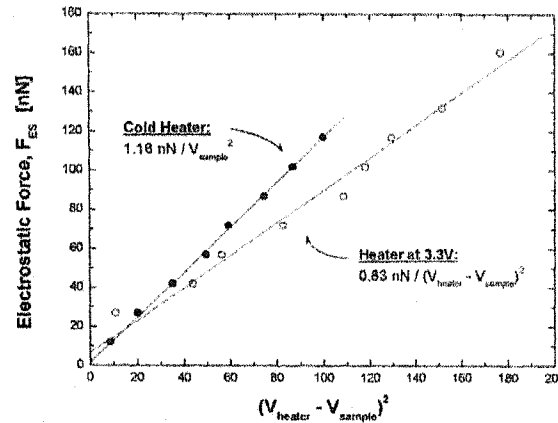
Figure 9.5.2-2: Determining the electrostatic force calibration constant

9.6 Nanoindentation

During a nanoindentation test, a geometrically well defined probe is pressed into a sample with a known rate. Both the applied force and displacement are recorded simultaneously. Once the predetermined maximum load is achieved, the probe is unloaded at a specified rate. Again, both the applied force and displacement are recorded. This technique is similar to the *SFM Force Spectroscopy* technique descriped above. The advantage to nanoindentation is that the actual penetration distance into the sample may be accessed, whereas with SFM, the combined displacement of both the bending cantilever and the sample is measured. A force-displacement curve, Figure 9.6-1, is the general result from the indentation experiment.

Figure 9.6-1: (A) Generalized nanoindentation force-displacement curve. Illustration of indentation geometry (B) under load and (C) after unloading.

138

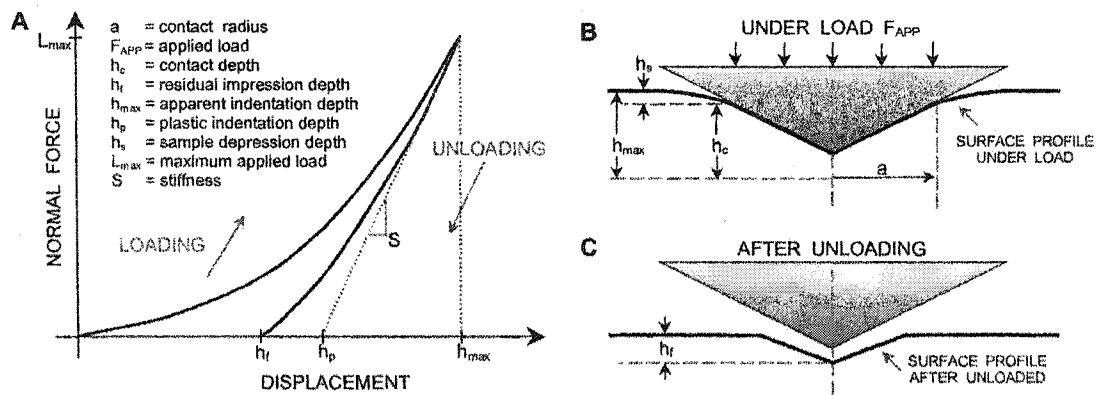Before indentations can analyzed, they must be reproducible. There many factors which may affect the reproducibility, including: sample roughness and inhomogeneities, pile-up or sink-in effects, and viscoelastic effects. The analysis procedes as follows. The contact depth, h_c, is determined by equation 9.6-1.[21]

$$h_c = h_{max} - \varepsilon \frac{L_{max}}{S}$$ (9.6-1)

where $\varepsilon = 0.72$ for conical and Berkovich tips, and the plastic indentation depth, h_p, has the relation:

$$h_p = h_{max} - \frac{L_{max}}{S}$$ (9.6-2)

The sample depression depth, h_s, is the difference between the apparent indention depth, h_{max}, and the contact depth, i.e.

$$h_s = h_{max} - h_c$$ (9.6-3)

The indentation stiffness, S, is measures as the slope of the linear portion of the unloading curve, shown in Figure 9.6-1. This stiffness value is related to the sample modulus via:[21]

$$S = \frac{E_r}{2} \sqrt{\frac{A_c}{\pi}}$$ (9.6-4)

where A_c is the projected contact area and E_r is the reduced modulus:

$$E_r = \left(\frac{1 - \upsilon_i^2}{E_i} + \frac{1 - \upsilon_s^2}{E_s} \right)$$ (9.6-5)

with ν as the Poisson ratio, E as the Young's modulus, and i and s denoting the indenter and sample, respectively. With knowledge of the indenter modulus and Poisson ratio, the sample modulus may be deduced from the indentation experiment provided that the projected contact

area, A_c, may be determined. Tip characterization methods are available,[21] allowing the contact area to be defined as a function of the contact depth. In addition, the contact area may be calculated for specific indenter geometries, for example the contact area for a Berkovich tip is given as:

$$A_c = 24.5 h_c^2 \qquad\qquad (9.6\text{-}6)$$

Finally, the sample hardness, H, is determined by:

$$H = \frac{L_{max}}{A_c} \qquad\qquad (9.6\text{-}7)$$

The sample modulus and hardness are the two primary material properties that nanoindentation measurements provide. Nanoindentation measurements compliment SFM studies, as SFM techniques do not offer means to accurately determine either the contact depth nor the contact area.. Like SFM studies, however, new modes of conducting nanoindentation studies continue to be developed. One such technique is discussed below.

9.7 Shear Modulated Nanoindentation

One limitation of SFM is that no satisfactory quantitative method exists for contact mechanical analysis because of poorly defined tip geometries. With nanoindentation, tip characterization methods are available,[21] allowing the contact area to be defined and permitting an adequate quantitative rheological analysis of thin films. Building on the success of force modulated SFM, Asif et al.[4] developed a normal force modulated nanoindentation technique that has proved useful for nanomechanical property and long range surface forces measurements.

To further expound nanoindentation capabilities, I have developed a new shear modulated nanoindentation procedure for measuring thermal transitions in polymers. The technique was employed to measure the glass transition temperature, T_g, of polymer thin films, and the results are compared to T_g values obtained by SM-FM and differential scanning calorimetry (DSC). The experimental procedure and the effects of critical test parameters are discussed, and an assessment on the accuracy and utility of this method is offered.

The nanoindentation thermal transition measurement procedure discussed herein utilizes a laterally modulated SFM stage (Topometrics Discoverer) combined with a single axis capacitive load-displacement nanoindenter transducer, (Hysitron Triboscope, k_N=149N/m). A sinusoidal shear perturbation was applied to determine the strain-rate of the sample film as function of the temperature. A lateral perturbation is preferred in order to keep the contact area about constant, avoiding the strong rate dependencies in polymer transition measurements.[14] Because the single axis nanoindenter is primarily sensitive to normal displacements, a non-perpendicular tip-sample angle ($< 5°$) was used to create a sub-nanometer normal component of the lateral modulation.

The sample and heating stage are mounted on a piezoelectric actuator that is sinusoidally modulated in the lateral direction. The indenter tip is maintained at a constant applied load and forms a stationary, no-slip contact with the sample. During modulation, the normal force acting on the tip is imposed on the transducer signal and can be analyzed using *lock-in* techniques. Rheological changes in the polymer resulting from thermal transitions, i.e. glass transitions, affect the tip-sample contact stiffness, and with it, the modulation response of the indenter and the transducer signal.

Experimental details are illustrated in Figure 9.7-1. The heater stage consisted of a machined Macor housing, a thermoelectric heater (02/031/018A, Ferrotec America Corp.), and a copper sample mounting disc; items 7, 6, 5 in Figure 9.7-1, respectively. A steel disc in the bottom of the Macor housing (not illustrated) was used to fix the heater stage to the magnet in the head of the piezoelectric scanner, item 8 in Figure 9.7-1.

The polymer sample was spin coated onto silicon (001 crystal), and the substrate was glued to the copper disc of the heater stage. A non-compliant, high conductivity thermal compound was applied between the silicon and copper disc to promote uniform heating. No significant difference in the load frame compliance was observed between glued or mechanically clamped samples.

A thin film detector temperature sensor (Omega Inc.) was fixed to the sample surface with thermal compound and glue. All temperature measurements were recorded directly at the polymer film surface. The sample temperature was monitored with a multimeter (HP 34401A) and controlled from LabView, Figure 9.7-1. A DC power supply (HP 6653A) was used to power the heater.

The indenter load-displacement transducer acts as the modulation response sensor, and was mounted directly on the SFM stage above the sample. Principles of the capacitive load-

displacement transducer have been discussed elsewhere.[4] A conical tungsten stylus with a tip radius of ~5 μm was used in this study.
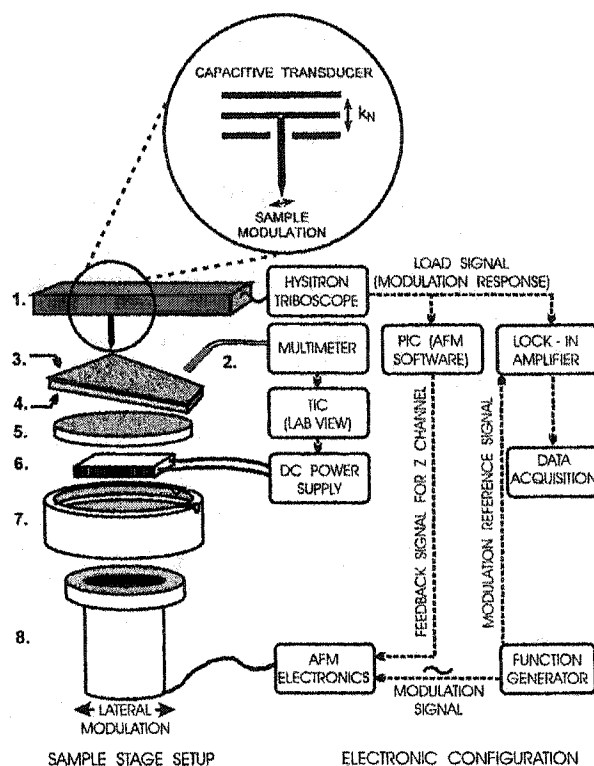

Figure 9.7-1: Physical and electrical configuration of the shear modulated nanoindentation technique used for measuring thermal transitions of polymer films. (1) Hysitron Triboscope (capacitive load-displacement transducer). (2) Thin Film Detector temperature sensor. (3) Polymer film sample. (4) Sample substrate (silicon). (5) Copper disc. (6) Thermoelectric heater. (7) Macor heater housing. (8) piezoelectric tube scanner of a Topometrix Discoverer SFM. Outtake: Schematic illustrating the indenter plate in the capacitive transducer (k_N = indenter normal spring constant.)

Sample shear modulation was provided by using a function generator (SRS D5345) to add a sinusoidal modulation to the piezoelectric SFM scanner. The modulation frequency was selected from a frequency spectrum of the operating system avoiding any system resonance frequencies, and ranging from 0.5-5 kHz. (NOTE: a modulation frequency less than 1 kHz is best for the Hysitron Triboscope because of the low pass filter build into this system.) The lateral modulation amplitude was chosen small enough to avoid sliding across the sample surface, and ranged from 6-9 nm. The corresponding normal component was estimated in the Ångstrom range.

Constant normal loads ranging from 1-5 μN were applied. The normal component of the force modulation was small compared to the applied normal load, and the modulation frequency was much higher than that of the applied load feedback control loop, i.e. the load control feedback was unaware of the small, fast normal modulation component acting on the tip. The transducer signal was analyzed in comparison to the modulation signal with a two phase lock-in amplifier (SRS SR830 DSP). For each temperature step, the amplitude and phase response of the transducer signal were recorded once thermal equilibrium was achieved. Typical values for the lock-in amplifier time constant ranged from 0.3-3 s, and a sensitivity of 20 mV was used.

The results of the T_g measurement are reported in Figure 9.7-2 for a poly-t-butylacrylate (M_w=137.3k) (PtBA)film spin cast onto a silicon <001> and annealed above its glass transition temperature under vacuum. The film thickness was 172±6 nm, measured by ellipsometry.
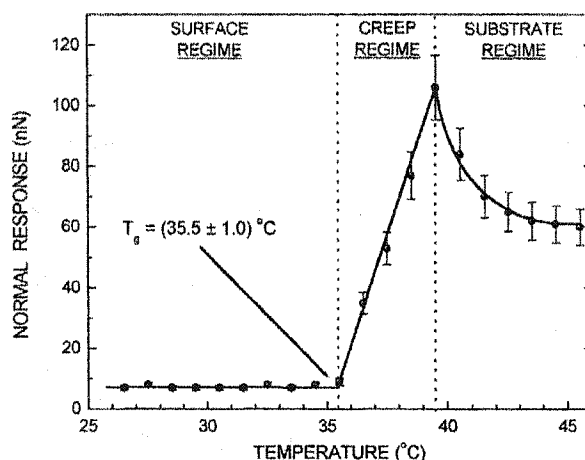
Figure 9.7-2: Shear modulated nanoindention T_g results for PtBA. Heating rate exceeds creep rate. (0.9°C/min, Normal load = 1.0 μN, modulation frequency = 900Hz, modulation amplitude = 7nm). A T_g value of (35.5±1.0) °C is indicated by the discontinuous rise in the shear response.

Three regimes are apparent in Figure 9.7-2: The *surface-regime* where $T < T_g$ and the stylus is on the sample surface; the *creep-regime* where $T \sim T_g$ and the stylus starts to creep into the polymer; and the *substrate-regime* where $T > T_g$ and the stylus approaches a dynamic equilibrium with the sample after creeping through the polymer to the substrate.

In the surface-regime, the indenter normal response remains independent of temperature. It is expected that in this regime, the indenter tip remains on the sample surface without creeping

into the polymer, i.e. the contact area is constant. At $T = T_g$, the *creep-regime* is entered, and rheological changes in the polymer allow the tip to begin creeping into the sample. As the stylus sinks deeper into the polymer, the contact area increases, and the indenter normal response increases. Once the tip has crept through the polymer to the substrate, the substrate-regime is entered. At this point, the modulating sample and indenter tip asymptotically approach a constant normal response value where a dynamic equilibrium is achieved.

Variations in the nature of the transition at T_g have been observed. The constant normal response in the surface-regime and discontinuous transition at T_g, illustrated in Figure 3.4.1-2, indicate that the indenter stylus remains on the sample surface until T_g is reached, then the stylus begins to creep into the polymer. Continuous transitions through T_g have been observed with some indenter stylus geometries, for example, a diamond Berkovich indenter. Such a gradual continuous transition may indicate that the indenter tip has penetrated the polymer surface and began creeping prior to the glass transition. Generally, pre-T_g surface penetration has been observed with sharper and "edged" indenter geometries like Berkovich or cube-cornered tips. We have found a *blunted* indenter geometry better suited for nanoindenter T_g measurements on polymer films because it has less tendency to *cut* into the surface, i.e. reduced contact pressures for a given load. However, in some cases, discrete T_g transitions have been obtained with a Berkovich tip, and continuous T_g transitions were obtained with a blunt conical tip.

Another parameter that contributes to the nature of the measured T_g transition is the sample heating rate. Once T_g has been reached, the slope of the normal response in the creep-regime has been found dependent on the heating rate. If the heating rate is faster than the creep rate, the sample temperature will continually increase while the indenter is creeping into the polymer. This behavior results in a positive, non-infinite slope of the normal response in the creep-regime, as in Figure 3.4.1-2. Conversely, if the heating rate is much slower than the creep rate, the indenter tip will penetrate the polymer film and reach the substrate prior to a noticeable temperature change. As a result, the measured normal response will show an infinite slope in the creep-regime, i.e. a discontinuous jump at T_g from the surface-regime directly to the substrate-regime, illustrated in Figure 9.7-3.

In terms of heating rate, a more precise T_g measurement is obtained for a heating rate much slower than the creep rate. Note the difference in the temperature scales in Figures 9.7-2 and 9.7-3, respectively. Generally, when dealing with a sample of unknown T_g, the best experimental approach has been to first analyze the sample using a fast heating rate, ~1°C/min,

to determine a rough value for T_g. Next, the sample may be re-tested with a slow heating rate over a more narrow temperature range if a more precise value of T_g is desired.
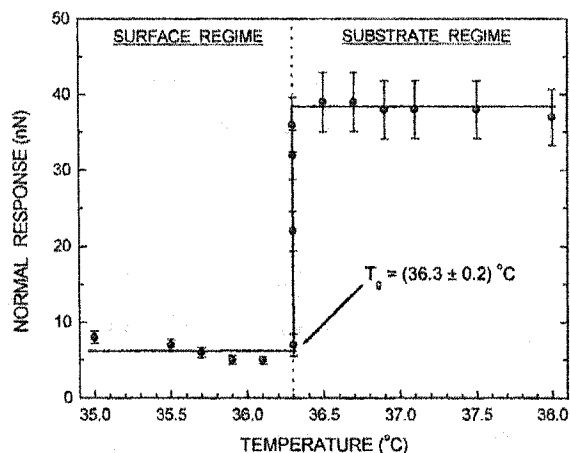

Figure 9.7-3: Shear modulated nanoindention T_g results for PtBA. Heating rate lags creep rate. (0.06°C/min., Normal load = 1.0 µN, modulation frequency = 1250Hz, modulation amplitude = 9nm). A T_g value of (36.3±0.2) °C is indicated by the discrete step in the shear response .

To test the accuracy of the modulated nanoindentation technique, the T_g value of the same polymer film was tested with the SM-FM technique presented elsewhere.[14] The SM-FM data reported in Figure 9.7-4A indicate a T_g value of (37±2)°C for the 172 nm PtBA film. The T_g values of (35.5±1.0) and (36.3±0.2)°C reported in Figures 9.7-3 and 9.7-4A, respectively, are in good correspondence. Additionally, a T_g value of about 40°C was obtained for the bulk polymer analyzed by DSC, Figure 9.7-4B. The T_g values obtained by the various experimental methods are summarized in Table 9.7-1.

Table 9.7-1: T_g Values of PtBA obtained from various experimental methods.

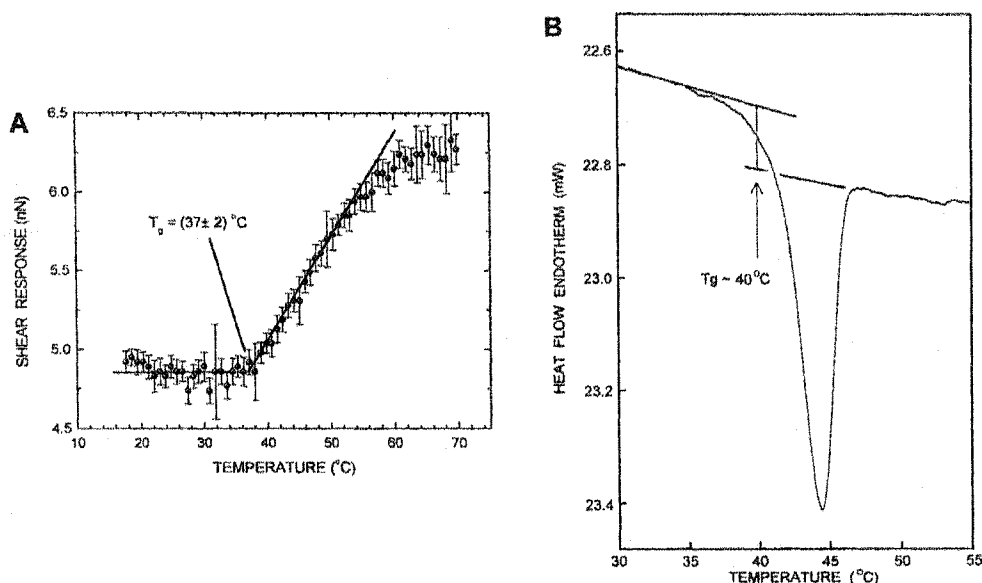| Experimental Method	T_g (°C)
Nanoindentation (heating rate < creep rate)	36.3 ± 0.2
Nanoindentation (heating rate > creep rate)	35.5 ± 1.0
Shear Modulation SFM	37 ± 2
Differential Scanning Calorimetry	~ 40

Figure 9.7-4: (A) No-slip shear modulated SFM results indicating a T_g value of roughly 37°C for the PtBA film (normal load = 1.0nN, modulation frequency = 4kHz, modulation amplitude = 14 nm). (B) Differential scanning calorimetry results for PtBA indicating a T_g value of approximately 40°C.

The versatility of this method may easily be expanded to determine the polymer viscoelastic functions above T_g, i.e. the creep compliance, $J(t)$, and relaxation modulus, $E(t)$, if a 2 axis capacitive load-displacement transducer (Hysitron 2D Transducer) is used instead of the single axis transducer.

Using a 2 axis transducer will offer the lateral sensitivity necessary for conducting shear modulated T_g measurements[14] with a negligible normal component, i.e. constant normal load. Under these conditions, it will be possible to measure the indenter penetration depth, or creep, as a function of time, $\delta(t)|_T$, for each temperature that the shear modulation response is recorded during the T_g measurement. It is important to note that the sample is maintained at isothermal conditions during each measurement. The penetration depth – time data may be used to calculate the viscoelastic creep compliance function for each temperature:[22]

$$J(t)\big|_T = \frac{2\gamma^2(1-\nu^2)}{gk} \cdot \frac{L_o}{\delta^2(t)\big|_T}$$

(9.7-1)

where γ is the proportionality constant between the indenter displacement, h, and the contact depth, h_c (i.e. $h = \gamma h_c$); ν is the sample poisson ratio; L_o is the applied normal load; g is the geometric relation between the contact area, A_c, and the contact depth (i.e. $A_c = gh_c^2$); and k is an indenter-geometry-dependent constant. According to Love's solution for elastic surface deformation, $g = \pi/2$.[22] For a conical indenter, the shape factors $\gamma = \pi \cot^2 \beta$ and $k = \tan \beta$, where β is the inclined face angle of the conical indenter tip.

The experimentally determined expressions for $J(t)|_T$ may be reduced to a *master curve*, $J(t)|_{T_o}$, by applying the well-known rule of *time-temperature superposition*.[23] During this process, an expression for the time-temperature shift factor, $a_T(T)$, may be determined by fitting the results to the WLF equation:

$$\log(a_T) = \frac{-c_1(T - T_o)}{c_2 + T - T_o} \qquad (9.7\text{-}2)$$

where T_o is an arbitrary reference temperature equal to or above T_g; and the constants c_1 and c_2 can be evaluated empirically from the given data[23] or estimated as 17.44 and 51.6 on the absolute temperature scale, respectively, for a wide range of polymers.[24] The effect of the *time-temperature superposition* is to decouple the complicated dependence of the viscoelastic functions on both time (frequency) and temperature into one function of time alone, the $J(t)|_{T_o}$ *master curve*, and one function of temperature alone, the a_T *shift factor* representing the ratio of relaxation times at two different temperatures.

Given the values for c_1 and c_2, the fractional free volume in the glass transition region, f_g, and the coefficient of thermal expansion, α_f, may be determined:[24]

$$f_g = B/(2.303\, c_1) \qquad (9.7\text{-}3)$$

$$\alpha_f = f_g / c_2 \qquad (9.7\text{-}4)$$

where B is a constant taken as unity according to Doolittle.[25] In addition, the apparent activation energy, E_a, for the relaxation process in the WLF region ($T > T_g$) is obtained for any specific temperature by:[26]

$$E_a = -2.303\,(c_1/c_2)RT^2 \qquad (9.7\text{-}5)$$

where R is the gas constant.

Once the $J(t)|_{T_o}$ *master curve* and a_T *shift factor* have been determined, the sample creep compliance at any time and temperature above T_g may be evaluated from:

$$J(t)|_T = \frac{\rho(T)}{\rho(T_o)} \frac{T}{T_o} J(a_T t)|_{T_o} \qquad (9.7\text{-}6)$$

where ρ is the polymer density. The density ratio accounts solely for thermal expansion[23] and is often set to unity in the absence of empirical data.[27]

In the linear viscoelastic regime, the Duhamel's convolution integral offers an implicit relation between the creep compliance function and the relaxation modulus, $E(t)$:[22]

$$t = \int_0^t J(t')E(t-t')dt' \qquad (9.7\text{-}7)$$

Equation 4 is most easily evaluated in Laplace transform space as a simple algebraic equation:

$$L[J(t)] = \frac{1}{s^2} \frac{1}{L[E(t)]} \qquad (9.7\text{-}8)$$

where $L[..]$ indicates the Laplace transform with transform variable s.

In summary, new method for analyzing thermal transitions of organic materials has been developed and successfully applied to measure the glass transition temperature of PtBA thin films. The method employs a lateral and normal perturbation of the polymer surface with the nanoindenter tip. The capacitive load-displacement transducer acts as a rheological sensor for the polymer response to the perturbation, and the response signal is analyzed using a lock-in amplifier. As a polymer undergoes a thermal transition where the material properties affected, i.e. a glass transition, the nature of the stylus-sample contact under the perturbed conditions is altered. The indenter transducer is sensitive to these changes. The accuracy of the presented method has been confirmed by differential scanning calorimetry and shear modulated SFM measurements. The displacement modulated nanoindentation technique offers great precision in determining T_g values of thin polymer films.

For an applied load of 1μN on soft polymers, we have demonstrated that a blunt tip, ~5μm radius, offered enhanced performance over conventional sharp diamond tips, i.e. 50 nm Berkovich or cube-cornered tips. Due to the reduced contact stress, the blunt tips tend to stay on the sample surface where the sharper tips tend to cut into the sample, penetrating to the substrate prior to the onset of a thermal transition. Additionally, the sample heating rate is a critical parameter in the thermal transition measurements. The precision of the T_g measurement depends on the relative heating and creep rates, where the best results are obtained when the heating rate is slower than the creep rate.

Considering other polymer thermal analysis techniques, differential scanning calorimetry is best suited for bulk property measurements and does not allow for mesoscale studies of thin films. Modulated SFM techniques lack satisfactory quantitative contact mechanical analysis methods because of poorly defined tip geometries. However, for indentation, sophisticated methods are available to define the tip geometry, and absolute quantitative analysis of material properties is possible. Advantages of the presented thermal transition analysis method include: high precision in determining T_g values, and temperature dependent qualitative rheological analysis. Combined with the normal modulation technique of Asif et al.,[4] the presented modulation technique will make the nanoindenter uniquely suitable for studying submicron scale systems.

The combined lateral and normal force modulation approach employed in this study was used because of current system limitations, i.e., the single axis nanoindenter was only sensitive to normal perturbations. Therefore, a non-perpendicular tip-sample angle was used to create a normal component of the lateral sample modulation. Future improvements on the presented technique will include work to provide unidirectional force modulation. Strictly normal modulation will allow for temperature dependent normal contact stiffness measurements during the thermal transition analysis, and strictly shear modulation may be employed with a 2 axis capacitive load-displacement transducer (Hysitron 2D Transducer) for simultaneous thermal transition and creep compliance measurements. This later technique, combined with the principle of time-temperature superposition, will lead to the evaluation of the glass transition temperature; viscoelastic functions, i.e. creep compliance and relaxation modulus; apparent relaxation activation energies; coefficient of thermal expansion, and fractional free volume at T_g, all in a single experiment.

9.8 Notes to Chapter 9

[1] R. Luginbuhl, R. M. Overney and B. D. Ratner, *ACS Symposium: Interfacial Properties on the Submicrometer Scale* 781, 178 (2001).

[2] R. M. Overney and S. E. Sills, *ACS Symposium: Interfacial Properties on the Submicrometer Scale* 781, 2 (2001).

[3] G. Haugstad, J. A. Hammerschmidt and W. L. Gladfelter, *ACS Symposium: Interfacial Properties on the Submicrometer Scale* 781, 230 (2001).

[4] S. A. S. Asif, K. J. Wahl and R. J. Colton, *Rev. Sci. Instrum.* 70, 2408 (1999).

[5] J. N. Israelachvili and D. Tabor, *Proc. R. Soc. London, Ser. A* 331, 19 (1972).

[6] G. Binnig, C. F. Quate and C. Gerber, *Phys. Rev. Lett.* 56, 930 (1986).

[7] J. B. Pethica, R. Hutchings and W. C. Oliver, *Philos. Mag. A* 48, 593 (1983).

[8] M. A. Lantz, S. J. O'Shea, A. C. F. Hoole and M. E. Welland, *Appl. Phys. Lett.* 70, 970 (1997).

[9] M. He, A. Szuchmacher-Blum, G. Overney and R. M. Overney, *Phys. Rev. Lett.* 88, 154302 (2002).

[10] R. M. Overney, H. Takano, M. Fujihira, W. Paulus and H. Ringsdorf, *Phys. Rev. Lett.* 72, 3546 (1994).

[11] R. M. Overney, E. Meyer, J. Frommer, D. Brodbeck, R. Luethi, L. Howald, H. J. Guentherodt, M. Fujihira, H. Takano and Y. Gotoh, *Nature (London)* 359, 133 (1992).

[12] C. K. Buenviaje, S. R. Ge, M. H. Rafailovich and R. M. Overney, *Mat. Res. Soc. Symp. Proc.* 522, 187 (1998).

[13] R. M. Overney, E. Meyer, J. Frommer, H. J. Guentherodt, M. Fujihara, H. Takano and Y. Gotoh, *Langmuir* 10, 1281 (1994).

[14] R. M. Overney, C. Buenviaje, R. Luginbuhl and F. Dinelli, *J. Therm. Anal. Cal.* 59, 205 (2000).

[15] F. Dinelli, C. Buenviaje and R. M. Overney, *Journal of Chemical Physics* 113, 2043 (2000).

[16] P.-G. de Gennes, *C.R. Acad. Sci.* IV, 1 (2000).

[17] S. Ge, Y. Pu, W. Zhang, M. Rafailovich, J. Sokolov, C. Buenviaje, R. Buckmaster and R. M. Overney, *Physical Review Letters* 85, 2340 (2000).

[18] C. Buenviaje, F. Dinelli and R. M. Overney, in *ACS Symposium Series "Interfacital Properties on the Submicron Scale"*, edited by J. Frommer and R. M. Overney (Oxford University Press, Oxford, 2000).

[19] A. Schallamach, *Wear* 17, 301 (1971).

[20] P. Vettiger, G. Cross, M. Despont, U. Drechsler, U. Duerig, W. Heberle, M. I. Lantz, H. E. Rothuizen, R. Stutz and G. K. Binnig, *IEEE Transactions on Nanotechnology* 1, 39 (2002).

150

[21]   W. C. Oliver and G. M. Pharr, *J. Mater. Res.* 7, 1564 (1992).

[22]   S. Shimizu, T. Yanagimoto and M. Sakai, *J. Mat. Res.* 14, 4075 (1999).

[23]   J. D. Ferry, *Viscoelastic Properties of Polymers, 3rd ed.* (John Wiley & Sons, New York, 1980).

[24]   U. W. Gedde, *Polymer Physics* (Chapman & Hall, New York, 1995).

[25]   A. K. Doolittle, *J. Appl. Phys.* 23, 236 (1952).

[26]   P. R. Higgenbotham-Bertolucci, H. Gao and J. P. Harmon, *Poly. Eng. Sci.* 41, 873 (2001).

[27]   U. Eisele, *Introduction to Polymer Physics* (Springer-Verlag, Berlin, 1990).

10. Closing Remarks and Future Outlook

Rheological material properties that were predominantly determined by macroscopic experiments in the past, e.g. viscosity and modulus, represent underlying microscopic transport properties of momentum and energy. These transport mechanisms are governed by couplings between atoms or molecules, intra- and intermolecular degrees of freedom, and external forces. Simply, phenomenological rheological properties are dictated by molecular mobility.

Fundamental insight to mesoscopic molecular motion is provided with the nanoscale probing techniques presented here. Lateral force microscopy studies of the dynamics and kinetics in polymer films reveal activation energies related to particular molecular relaxations, and provide insight to finite size limited structural relaxations near the glass transition. Direct access to the temperature resolved length scale for cooperative motion during the glass transition reveals a crossover from intra- to inter- molecular relaxation in the transition regime, and confirms the dynamical heterogeneity of the glass transition.

Nanotechnological thin film applications, such as terabit thermomechanical data storage, rely on very specific relaxation and transition properties in the sub-one-hundred nanometer regime. Ultimately, achieving the desired performance goals will require engineered polymeric materials of *tailored* molecular structure, in order to achieve the narrow range of physiochemical properties in demand. In polymer films, when film thicknesses are reduced to the nanometer scale, the structural, material, and transport properties become increasingly dominated by interfacial and dimensional constraints. Rheological boundary layers are formed at interfaces, due to shear induced structuring and anisotropic diffusion during film preparation. Within the boundary region, rheological gradients lead to bulk-deviating behaviors. These gradients are quantified with interfacial glass transition (T_g) profiles, which provide a molecular structural model of the boundary layer and allow characterization of the interfacial constraints. The development and optimization efforts of thin film technologies will be challenged to work within these interfacial constraints, or yet, to utilize the constraints as engineering design opportunities.

Very specific material engineering is possible with an understanding of polymer dynamics at interfaces. Modified relaxational properties and enhanced conformational stability may be achieved through control of the interfacial conditions, molecular weight, crosslinking density, and film thickness. Hence, the characterization and control of interfacial boundary layers becomes increasingly important to nanotechnological applications. In contact mechanical operations on thin polymer films, the rheological gradient within the boundary dictates the mean

contact pressure, while the substrate itself can lead to stress and strain shielding at the interface and compromise film stability. *Modulus-matching* techniques, i.e. generating a quasi-continuous modulus gradient between the two opposing faces, offer enhanced interfacial stress transmission and improved stability and durability of the interface. Countless applications stand to benefit from modulus-matching; for example, improving the stress distribution across the implant-bone interface via modulus-matching offers promise of increased longevity for artificial hip implants. To this end, a resurgence of design methodologies is foreseen, moving from traditional scaling approaches, to a mesoscopic approach where internal rheological gradients are catered to achieve the desired performance characteristics.

Bibliography

E. A. Abbott, *Flatland - A Romance of Many Dimensions* (Dover Publ., New York, 1992).

M. J. Adams, A. Allan, B. J. Briscoe, P. J. Doyle, D. M. Gorman and S. A. Johnson, Wear **251**, 1579 (2001).

G. Adam and J. H. Gibbs, J. Chem. Phys. **43**, 139 (1965).

D. Allara, F. Fowkes, J. Noolandi, G. Rubloff and M. Tirrell, Mater Sci Eng **83**, 213 (1986).

R. G. C. Arridge, Mechanics of Polymers (Clarendon Press, Oxford, 1975).

S. A. S. Asif, K. J. Wahl and R. J. Colton, Rev. Sci. Instrum. **70**, 2408 (1999).

D. Askeland, *The Science and Engineering of Materials* (PWS_KENT Publishing Company, Boston, 1989).

V. Barron, Materials World **5**, 656 (1997).

J. Benkoski, J. Bates and E. Kramer, ACS National Meeting; Orlando, FL , 7 (2002).

C. Bennemann, C. Donati, J. Baschnagel and S. Glotzer, Nature **399**, 246 (1999).

G. Binnig, C. F. Quate and C. Gerber, Phys. Rev. Lett. **56**, 930 (1986).

G. K. Binnig, G. Cherubini, M. Despont, U. T. Duerig, E. Eleftheriou and P. Vettiger, in *Springer Handbook of Nanotechnology*, ed B. Bhushan (Springer-Verlag, Heidelberg, 2004).

T. Bonner and A. Baratoff, Surf. Sci. **377-379**, 1082 (1997).

A. Borkar, J. Tsamopoulos, S. Gupta and R. Gupta, Physics of Fluids **6**, 3539 (1994).

J. Bouchet, A. Roche and E. Jaquelin, J Adhesion Sci Technol **15**, 345 (2001).

F. P. Bowden and D. Tabor, *The friction and lubrication of solids* (Clarendon Press, Oxford, 1951).

R. F. Boyer and S. G. Turley, in *Molecular basis of transitions and relaxations*, edited by D.J.Meier (Gordon and Breach Science Publishers, New York, 1978), pp. 333.

B. J. Briscoe and D. C. B. Evans, Proc. R. Lond. A **380**, 389 (1982).

B. J. Briscoe, P. D. Evans, S. K. Biswas and S. K. Sinha, Trib. Int. **29**, 93 (1996).

M. Brogly, S. Bistac and J. Schultz, Macromol. Theory Simul. **7**, 65 (1998).

H. Brown, Annu Rev Mater Sci **21**, 463 (1991).

H. Brown, IBM J Res Develop **38**, 379 (1994).

H. Brown, Macromolecules **2001**, 3720 (2001).

H. Brown, Mat Res Soc Symp Proc **264**, 183 (1992).

154

F. Bueche, J. Chem. Phys. **30**, 448 (1959).

C. Buenviaje, F. Dinelli and R. M. Overney, in ACS Symposium Series *Interfacital Properties on the Submicron Scale*, Vol. **781**, edited by J. Frommer and R. M. Overney (Oxford U. P., New Orleans, 2000), pp. 76.

C. Buenviaje, S. Ge, M. Rafailovich, J. Sokolov, J. Drake and R. Overney, Langmuir **15**, 6446 (1999).

C. K. Buenviaje, S. R. Ge, M. H. Rafailovich and R. M. Overney, Mat. Res. Soc. Symp. Proc. **552**, 187 (1998).

D. Buser, T. Nydegger, T. Oxland, D. Cochran, R. Schenk, H. Hirt, D. Snetivy and L. Nolte, J Biomed Mater Res **45**, 75 (1999).

B. Bushan, *Principles and Applications of Tribology* (John Wiley & Sons, New York, 1999).

M. Cabrini, A. Cigada, G. Rondelli and B. Vicentini, Biomaterials **18**, 783 (1997).

W. Chau, V. Lee, J. Frommer, S. Sills and R.Overney, in CPIMA Forum 2001 (Center for Polymer Interfaces and Macromolecule Assemblies, Stanford, CA, 2001).

H. P. Chen, D. Katsis, J. C. Mastrangelo, S. H. Chem, S. D. Jacobs and P. J. Hood, Adv. Mater. **12**, 1283 (2000).

Q. Chen, N. Miyata, T. Kukubo and T. Nakamura, J Mat Sci: Materials in Medicine **12**, 515 (2001).

P. Claudy, J. M. Letoffe, Y. Camberlain and J. P. Pascault, Polym. Bull. **9**, 208 (1983).

C. Creton, J.-L. Halary and L. Monnerie, Polymer **40**, 199 (1998).

R. Crowninshield, Clinical Orthopaedics **235**, 166 (1988).

R. Crownshield, R. Brand, R. Johnston and J. Milroy, Clinical Orthopaedics **146**, 71 (1980).

K. Dalnoki-Veress, J. A. Forrest, P. G. d. Gennes and J. R. Dutcher, J. Phys. IV **10**, 221 (2000).

S. Das, H. Manohara and C. Malek, Proceeedings of the SPIE: The International Society for Optical Engineering. 3225, 85 (1997).

G. Dean and B. Read, Poly. Testing **20**, 677 (2001).

R. Defay and J. R. Hommelen, J. Colloid. Sci. **14**, 411 (1959).

P.G. de Gennes, C.R. Acad. Sci. **IV**, 1 (2000).

G. B. DeMaggio, W. E. Frieze, D. W. Gidley, M. Zhu, H. A. Hristov and A. F. Yee, Phys. Rev. Lett. **78**, 1524 (1997).

E. A. DiMarzio and A. J. M. Yang, J. Res. Natl. Inst. Stand. Technol. **102**, 135 (1997).

F. Dinelli, C. Buenviaje and R. M. Overney, J. Chem. Phys. **113**, 2043 (2000).

E. Donth, J. Non-Cryst. Solids **53**, 325 (1982).

A. K. Doolittle, J. Appl. Phys. **23**, 236 (1952).

A. Dorinson and K. C. Ludema, *Mechanics and Chemistry in Lubrication* (Elsevier, Amsterdam, 1985).

O. K. Dudko, A. E. Filippov, J. Klafter and M. Urbakh, Chemical Physics Letters **352**, 499 (2002).

U. Eisele, *Introduction to Polymer Physics* (Springer-Verlag, Berlin, 1990).

A. Eisenberg, in ACS Symposium Series *Physical Properties of Polymers*, 2nd ed., edited by J. E. Mark (ACS, Washington DC, 1993).

M. K. Endoh, S. Saito and T. Hashimoto, Macromolecules **35**, 7692 (2002).

J. Engelhardt and S. Saha, Med Bio Eng Computing **26**, 38 (1988).

S. Ertel and J. Kohn, J Biomed Mater Res **28**, 919 (1994).

H. Eyring, J. Chem. Phys. **4**, 283 (1936).

J. D. Ferry, *Viscoelastic Properties of Polymers*, 3rd ed. (John Wiley & Sons, New York, 1980).

J. A. Forrest and J. Mattsson, Phys. Rev. E **61**, R53 (2000).

J. A. Forrest, K. Dalnoki-Veress, J. R. Stevens and J. R. Dutcher, Phys. Rev. E **56**, 5705 (1997).

B. Frank, A. P. Gast, T. P. Russel, H. R. Brown and C. Hawker, Macromolecules **29**, 6531 (1996).

J. R. Fried, *Polymer Science and Technology* (Scott, Foresman, and Co., Glenview, IL, 1995).

Y. Fujinami, H. Hayashi, A. Ebe, O. Imai and K. Ogata, Mat. Chem. Phys. **54**, 102 (1998).

H. Gao, C.-H. Chiu and J. Lee, Int. J. Solids Structures **29**, 2471 (1992).

S. Ge, Y. Pu, W. Zhang, M. Rafailovich, J. Sokolov, C. Buenviaje, R. Buckmaster and R. M. Overney, Phys. Rev. Lett. **85**, 2340 (2000).

U. W. Gedde, Polymer Physics (Chapman & Hall, New York, 1995).

A. E. Giannakopoulos, Thin Solid Films **332**, 172 (1998).

E. Gnecco, R. Bennewitz, T. Gyalog, C. Loppacher, M. Bammerlin, E. Meyer and H.-J. Güntherodt, Phys. Rev. Lett. **84**, 1172 (2000).

T. Gray, C. Buenviaje, R. M. Overney, S. A. Jenekhe, L. Zheng and A. K. Y. Jen, App. Phys. Lett. **83**, 2563 (2003).

P. F. Green, T. M. Christensen, T. P. Russel and J. J. Jérôme, J. Chem. Phys. **92**, 1478 (1990).

S. Gross and E. Abel, J. Biomech. **34**, 995 (2001).

J. A. Hammerschmidt, W. L. Gladfelter and G. Haugstad, Macromolecules **32**, 3360 (1999).

156

R. S. Hansen and T. C. Wallace, J. Phys. Chem. **63**, 1085 (1959).

W. B. Hardy and I. Doubleday, Proc. Roy. Soc. A **100**, 550 (1922).

T. Hanawa, in *The Bone-Biomaterial interface*, edited by J. Davies (University of Toronto Press, Toronto, 1991), pp. 49.

G. Haugstad, J. A. Hammerschmidt and W. L. Gladfelter, ACS Symposium: Interfacial Properties on the Submicrometer Scale **781**, 230 (2001).

M. He, *dissertation*, University of Washington, 2002.

M. He, A. Szuchmacher Blum, G. Overney and R. M. Overney, Phys. Rev. Lett. **88**, 154302/1 (2002).

K. Healy and P. Ducheyne, Biomaterails **13**, 553 (1992).

F. Heslot, T. Baumberger, B. Perrin, B. Caroli and C. Caroli, Phys. Rev. E **49**, 4973 (1994).

P. R. Higgenbotham-Bertolucci, H. Gao and J. P. Harmon, Poly. Eng. Sci. **41**, 873 (2001).

R. Hill, *The mathematical theory of plasticity* (Oxford University Press, London, 1950).

J. Israelachvili, M. P., M. Gee, A. Homola, M. Robbins and P. Thompson, J. Phys.: Condens. Matter **2**, 89 (1990).

J. N. Israelachvili and D. Tabor, Proc. R. Soc. London, Ser. A **331**, 19 (1972).

T. Ito, Y. Okayama and S. Shiratori, Thin Solid Films **393**, 138 (2001).

K. James, H. Levene, J. Parsons and J. Kohn, Biomaterials **20**, 2203 (1999).

V. D. Jardret and W. C. Oliver, Mat. Res. Soc. Symp. Proc. **594**, 251 (2000).

K. L. Johnson, *Contact Mechanics* (Cambridge University Press, Cambridge, UK, 1985).

K. L. Johnson, J. Mech. Phys. Solids **18**, 115 (1970).

M. Joshi, S. Advani, F. Miller and M. Santare, J. Biomech. **33**, 1655 (2000).

C. Kaddick, S. Stur and E. Hipp, Med Eng Phys **19**, 431 (1997).

T. Kajiyama, K. Tanaka and A. Takahara, Macromolecules **28**, 3482 (1995).

T. Kanaya, A. Patkowski, E. W. Fischer, J. Seils, H. Glaser and K. Kaji, Macromolecules **28**, 7831 (1995).

I. Kangasniemi, V. CC, E. van der Velde and K. de Groot, J Biomed Mater Res **28**, 563 (1994).

I. Karapanagiotis, D. F. Evans and W. W. Gerbrich, Polymer **43**, 1343 (2002).

J. L. Keddie, R. A. L. Jones and R. A. Cory, Europhys. Lett. **27**, 59 (1994).

D. Keller, D. Swigon and C. Bustamante, Biophys. J. **84**, 733 (2003).

H. Kim, F. Miyaji, T. Kokubo, S. Nishiguchi and T. Nakamura, J Biomed Mater Res **45**, 100 (1999).

J. H. Kim, J. Jang and W. C. Zin, Langmuir **17**, 2703 (2001).

E. Kondoh, Thin Solid Films **359**, 255 (2000).

R. Kopelman, Science **241**, 1620 (1988).

D.E. Kramer, et al., J. Mater. Res. **16**, 3150 (2001).

J. Kuiper and R. Huskies, J Biomech Eng **14** (1997).

T. Kukubo, F. Miyaji and H. Kim, J Am Ceram Soc **79**, 1127 (1996).

M. A. Lantz, S. J. O'Shea, A. C. F. Hoole and M. E. Welland, Appl. Phys. Lett. **70**, 970 (1997).

C. Larsson, P. Thompsen, B. Aronson, M. Rodahl, J. Lausmaa, B. kasemo and L. Ericson, Biomaterials **17**, 605 (1996).

J. Lausmaa, in *Titanium in Medicine*, edited by D. Brunette (Springer-Verlag, Berlin, 2001), pp. 231.

T. Lee, E. Chang and C. Yang, J Mater Sci **9**, 439 (1998).

J. Lewis, M. Askew, R. Wixson, G. Kramer and R. Tarr, J Bone Joint Surgery **66-A**, 280 (1984).

L. Y. T. Li, H. C. Kim and C. J. Hawker, (Center for Polymer Interfaces and Macromolecule Assemblies, Stanford, CA, 2001).

Y. Liu, T. P. Russell, M. G. Samant, J. Stohr, H. R. Brown, A. Cossy-Favre and J. Diaz, Macromolecules **30**, 7768 (1997).

K. C. Ludema and D. Tabor, Wear **9**, 329 (1966).

W. D. Luedtke and U. Landman, Phys. Rev. Lett. **82**, 3835 (1999).

R. Luginbuhl, R. M. Overney and B. D. Ratner, ACS Symposium: Interfacial Properties on the Submicrometer Scale **781**, 178 (2001).

T. R. Malow, C. C. Koch, P. Q. Miraglia and K. L. Murty, Mat. Sci. Eng. **A252**, 36 (1998).

H. J. Mamin and D. Rugar, Appl. Phys. Lett. **61**, 1003 (1992).

C. Mattheck, U. Vorburg and C. Kranz, Biomedizinische Technik **35**, 316 (1990).

J. R. Matthews, Acta Met. **28**, 311 (1980).

A. A. McBeath and R. N. Foltz, Clinical Orthopaedics **141**, 66 (1979).

R. Metzler and J. Klafter, Phys. Reports **339**, 1 (2000).

R. Metzler and J. Klafter, Physica A **302**, 290 (2001).

G. F. Meyers, B. M. DeKoven and J. T. Seitz, Langmuir **8**, 2330 (1992).

158

S. Middleman, J. Appl. Phys. **62**, 2530 (1989).

P. T. Mikulski and J. A. Harrison, J. Am. Chem. Soc. **123**, 6873 (2001).

I. Morfin, P. Linder and F. Boue, Macromolecules **32**, 7208 (1999).

W. Murphy, M. Peters, D. Kohn and D. Mooney, Biomaterials **21**, 2521 (2000).

A. Nayebi, R. E. Abdi, O. Bartier and G. Mauvoisin, Mat. Sci. Eng. **A333**, 160 (2002).

S. Nishiguchi, H. Kato, H. Fujita, M. Oka, H. Kim, T. Kokubo and T. Nakamura, Biomaterials **22**, 2525 (2001).

S. Nishiguchi, T. Nakamura, M. Kobayashi, H. Kim, F. Miyaji and T. Kokubo, Biomaterials **20**, 491 (1999).

C. Ohtsuki, H. Iida, S. Hayakawa and A. Osaka, J Biomed Mater Res **35**, 39 (1997).

W. C. Oliver and G. M. Pharr, J. Mater. Res. **7**, 1564 (1992).

W. J. Orts, J. H. Van Zanten, W. L. Wu and S. K. Satija, Phys. Rev. Lett. **71**, 867 (1993).

R. M. Overney, C. Buenviaje, R. Luginbuhl and F. Dinelli, Journal of Thermal Analysis and Calorimetry **59**, 205 (2000).

R. M. Overney, C. Buenviaje, R. Luginbuehl and F. Dinelli, J. Therm. Anal. Cal. **59**, 205 (2000).

R.M. Overney and S. Sills, in *Interfacial Properties on the Submicron Scale*, ACS Symposium Ser. **781**. Ed. J. Frommer and R.M. Overney. (New Orleans, LA: Oxford University Press, 2000) 2-21.

R. M. Overney, L. Guo, H. Totsuka, M. Rafailovich, J. Sokolov and S. A. Schwarz, in *Dynamics in Small Confining Systems IV*, Vol. **464**, edited by J. M. Drake, J. Klafter, and R. Kopelman (Material Research Society, Pittsburgh, PA, 1997), pp. 133.

R. M. Overney, E. Meyer, J. Frommer, D. Brodbeck, R. Luethi, L. Howald, H. J. Guentherodt, M. Fujihira, H. Takano and Y. Gotoh, Nature (London) **359**, 133 (1992).

R. M. Overney, E. Meyer, J. Frommer, H. J. Guentherodt, M. Fujihara, H. Takano and Y. Gotoh, Langmuir **10**, 1281 (1994).

R. M. Overney and E. Meyer, MRS Bulletin XVIII, **26** (1993).

R. M. Overney, D. P. Leta, L. J. Fetters, Y. Liu, M. H. Rafailovich and J. Sokolov, J. Vac. Sci. Technol. B **14**, 1276 (1996).

R. M. Overney, H. Takano, M. Fujihira, W. Paulus and H. Ringsdorf, Phys. Rev. Lett. **72**, 3546 (1994).

J. Pan, D. Thierry and C. Leygraf, J. Biomed. Mater. Res. **30**, 393 (1996).

J. Pan, H. Liao, C. Leygraf, D. Thierry and J. Li, J Biomed Mater Res **40**, 244 (1998).

A. Patkowski, H. Glaser, T. Kanaya and E. W. Fischer, Physical Review E (Statistical, Nonlinear, and Soft Matter Physics) **64**, 031503 (2001).

J. B. Pethica, R. Hutchings and W. C. Oliver, Philos. Mag. A **48**, 593 (1983).

N. P. Petrov, *Friction in Machines and the Effect of the Lubricant* (St. Petersburg, 1883).

V. N. Pokrovskii, *The Mesoscopic Theory of Polymer Dynamics* (Kluwer Academic Publishers, Dordrecht, 2000).

R. Poss, P. Walker, M. Spector, D. T. Reilly, D. D. Robertson and C. B. Sledge, Clinical Orthopaedics **235**, 181 (1988).

P. Prendergast and D. Taylor, J Biomed Eng **12**, 379 (1990).

M. Rabeony, D. G. Pfeiffer, S. K. Behal, M. Disko, W. D. Dozier, P. Thiyagarajan and M. Y. Lin, J. Chem. Soc., Faraday Trans. **91**, 2855 (1995).

C. Ramond-Angélélis, *dissertation*, Ecole Nationale Supérieure des Mines de Paris, 1998.

N.X. Randall, C. Julia-Schmutz and J.M. Soro, Surf. and Coat. Tech. **108-109**, 489 (1998).

J. Rault, Journal of Physics: Condensed Matter **15**, 1193 (2003).

S. Reich and A. Eisenberg, J. Poly. Sci. A-2 **10**, 1397 (1972).

M. Reiner, Phys. Today January, **62** (1964).

T. Richardson, M. Peters, A. Ennett and D. Mooney, Nat Biotech **19**, 1029 (2001).

E. Riedo, E. Gnecco, R. Bennewitz, E. Meyer and H. Brune, Physical Review Letters **91**, 084502 (2003).

C. M. Roland and R. Casalini, J. Chem. Phys. **119**, 1838 (2003).

A. Rotem, J Med Eng & Tech **18**, 208 (1994).

M. G. Rozman, M. Urbakh and J. Klafter, Physica A **249**, 184 (1998).

T. P. Russel, A. Menelle, S. H. Anastasiadis, S. K. Satija and C. F. Majkrzak, Macromolecules **24**, 6263 (1991).

S. Saito and T. Hashimoto, J. Chem. Phys. **114**, 10531 (2001).

Y. Sang, M. Dube and M. Grant, Phys. Rev. Lett. **87**, 174301/1 (2001).

D. Schaefer, H. W. Spiess, U. W. Suter and W. W. Fleming, Macromolecules **23**, 3431 (1990).

A. Schallamach, Wear **17**, 301 (1971).

J. Schmidt and M. Hackenbroch, Archives of Orthopaedic Trauma Surgery **113**, 117 (1994).

D. Schrader, in *Mechanical Properties of Polymers*, edited by L. E. Nielsen (Reinhold Publishing Corp., Ney York, 1962), pp. V/91.

S. Shimizu, T. Yanagimoto and M. Sakai, J. Mat. Res. **14**, 4075 (1999).

J. I. Siepmann and I. R. McDonald, Phys. Rev. Lett. **70**, 453 (1993).

160

H. Sillescu, J. Non-Crystalline Solids 243, **81** (1999).

S. Sills and R.M. Overney, Phys. Rev. Lett., **91** (2003) 095501/1-4.

S. Sills, T. Gray, J. Frommer and R.M. Overney, in *Applications of Scanned Probe Microscopy to Polymers*, ed. J.D. Batteas, G.C. Walker, and C. Michaels (Americal Chemical Society, Washington D.C., 2004), (in press).

S. Sills, R. M. Overney, W. Chau, V. Y. Lee, R. D. Miller and J. Frommer, J. Chem. Phys. **120** (2004) 5334-8.

S. Sills, R.M. Overney, B. Gotsman, and J. Frommer, Tribo. Lett. (2004) (submitted).

M. J. Silva, K. L. Reed, D. D. Robertson, C. Bragdon, W. H. Harris and W. J. Maloney, J. Ortho. Res. **17**, 525 (1999).

C. Sitting, M. Textor, N. Spencer, M. Wieland and P. Vallotton, J Mater Sci: Mater Med **10**, 35 (1999).

I. M. Sokolov, Phys. Rev. E **63**, 011104/1 (2000).

S. Srinivasan, J. d. Andrade, S. B. Jr and R. L. Jr, Biomaterials **21**, 1929 (2000).

R. N. Stauffer, J. Bone Joint Surgery **64-A**, 983 (1982).

A. Stoch, W. Jastrzebski, A. Brozek, J. Stoch, J. Szaraniec, B. Trybalska and G. Kmita, J Molecular Structure **555**, 375 (2000).

N. P. Suh, *Tribophysics* (Prentice-Hall, Inc., Englewood Cliffs, NJ, 1986).

D. R. Summer, T. M. Turner, R. Igloria, R. M. Urban and J. O. Galante, J. Biomechanics 31, 909 (1998).S. Suresh, A. E. Giannakopoulos and J. Alcala, Acta mater. **45**, 1307 (1997).

C. J. Sutherland, A. H. Wilde, L. S. Borden and K. E. Marks, J. Bone Joint Surgery **64-A**, 970 (1982).

D. Tabor and R. H. S. Winterton, Proc. R. Soc. Lond. **A312**, 435 (1969).

D. Tabor, *The hardness of Metals* (Oxford University Press, London, 1951).

D. Taylor, C. Martin, B. Cornelis and M. Jones, Proc Instn Mech Engrs **207**, 121 (1993).

M. Textor, C. Sittig, V. Frauchiger, S. Tosatti and D. Brunette, in *Titanium in Medicine*, edited by D. M. Brunette (Springer-Verlag, Berlin, 2001), pp. 171.

G. A. Tomlinson, Philos. Mag. Ser. **7**, 905 (1929).

B. Tower, Proc. Inst. Mech. Engrs Nov., 632 (1883).

U. Tracht, M. Wilhelm, A. Heuer, H. Feng, K. Schmidt-Rohr and H. W. Spiess, Phys. Rev. Lett. **81**, 2727 (1998).

K. C. Tseng, N. J. Turro and C. J. Durning, Phys. Rev. E **61**, 1800 (2000).

T. Y. Tsui and G. M. Pharr, J. Mater. Res. **14**, 292 (1999).

T. Y. Tsui, J. Vlassak and W. D. Nix, J. Mater. Res. **14**, 2204 (1999).

A. Ulman, *An Introduction to Ultrathin Organic Films* (Academic Press, New York, 1991).

R. Vaisyanathan, M. Dao, G. Ranichandran and S. Suresh, Acta Mater. **49**, 3781 (2001).

F. Varnik, J. Baschnagel and K. Binder, European Physical Journal E **8**, 175 (2002).

P. Vettiger, G. Cross, M. Despont, U. Drechsler, U. Duerig, W. Heberle, M. I. Lantz, H. E. Rothuizen, R. Stutz and G. K. Binnig, IEEE Trans. Nanotechnol. **1**, 39 (2002).

P. S. Walker and D. D. Robertson, Clinical Orthopaedics **235**, 25 (1988).

Z. Wan, L. D. Dorr, T. Woodsome and A. Ranawat, J. Arthroplasty **14**, 149 (1999).

C. L. Wang and S. J. Wang, Phys. Rev. B **51**, 8810 (1995).

J. Washiyama, E. Kramer and C. Hui, Macromolecules **26**, 2928 (1993).

H. Weinans, R. Huskies and H. J. Grootenboer, J. Biomechanical Eng. **116**, 393 (1994).

H. Weinans, R. Huskies, B. V. Rietbergen, D. R. Summer, T. M. Turner and J. O. Galante, J. Ortho. Res. **11**, 500 (1993).

M. Wong, J. Eulenberger, R. Schenk and E. Hunziker, J Biomed Mater Res **29**, 1567 (1995).

X. Wu and K. D. Squires, J. Fluid Mech. **418**, 231 (2000).

S. Xiao, G. Kenausis and M. Textor, in *Titanium in Medicine*, edited by D. Brunette (Springer-Verlag, Berlin, 2001), pp. 417.

O. Yano and Y. Wada, J. Poly. Sci. **A-2 9**, 669 (1971).

H. Zhao, Polymer **39**, 1103 (1997).

X. Zheng, M. H. Rafailovich, J. Sokolov, Y. Strzhemechny, S. A. Schwarz, B. B. Sauer and M. Rubinstein, Phys. Rev. Lett. **79**, 241 (1997).

J. A. Zukas, T. Nicholas, H. F. Swift, L. B. Greszczuk and D. R. Curran, *Impact Dynamics* (John Wiley & Sons, New York, 1982).

Vita

Scott Sills was born in the New England fishing town of Gloucester, Massachusetts, and spent most of his childhood in suburban Pennsylvania. After earning a Bachelor of Chemical Engineering from the University of Delaware in 1995, he moved to rural Wyoming, for a process engineering stint in the chemical manufacturing industry. Four long, cold winters at 7000 ft. drove him westward again, to Seattle, and to the ever-fluid rivers of the Pacific Northwest. During his graduate studies at the University of Washington, he was distinguished as an IBM Pre-Doctoral Fellow for his work on interfacial nanorheology and the thermomechanical aspects of mesoscopic polymer dynamics. In 2004, he completed his Doctor of Philosophy in Chemical Engineering, becoming the 3rd generation Ph.D. in the Sills Family. His predecessors, father and paternal grandfather, both specialized in health science and physiology, while Scott likely inherited his engineering astuteness from his maternal grandfather, a life-long self-employed innovator.